Magnetotelluric Time-Series Denoising and Three-Dimensional Inversion for Geothermal Exploration in Indonesia

マリヤディ

Magnetotelluric Time-Series Denoising and Three-Dimensional Inversion for Geothermal Exploration in Indonesia

A Doctoral Dissertation

MARYADI

Department of Earth Resources Engineering,
Graduate School of Engineering,
Kyushu University

2024

Magnetotelluric Time-Series Denoising and Three-Dimensional Inversion for Geothermal Exploration in Indonesia

A Doctoral Dissertation
Submitted as a partial fulfillment of
the requirement for the degree of

Doctor of Engineering
(Exploration Geophysics)

Submitted by
MARYADI
(Student Number: 3TE21792P)

B.Sc. in Physics, University of Indonesia, Indonesia, 2013
M.Eng. in Exploration Geophysics, Kyushu University, Japan, 2018

Supervised by
Associate Professor Hideki MIZUNAGA

Department of Earth Resources Engineering,
Graduate School of Engineering,
Kyushu University
2024

ABSTRACT

Indonesia has a significant amount of geothermal energy resources that need to be explored. In geothermal exploration, the magnetotelluric (MT) method is the most commonly used geophysical technique for delineating the subsurface resistivity structure that depicts the geothermal system. However, the natural signal recorded in MT sensors is highly prone to noise interference and could disrupt the reliability of the data. Therefore, it is important to develop an MT time-series noise removal system that can significantly enhance the quality of MT data to support a successful geothermal exploration.

Another crucial issue regarding geothermal exploration using the MT method is the reliability of subsurface modeling, especially for areas located in geologically complex regions commonly found in Indonesia. The magnetotelluric method is not immune to the effects of geologic distortions caused by this complexity, making it difficult to model the subsurface resistivity structure due to the high dimensionality. Considering the subsurface model's reliability, appropriate modeling techniques are necessary to avoid misleading results due to insufficient and unsuitable modeling efforts. Therefore, it is essential to employ suitable modeling strategies to obtain a reliable resistivity model of the subsurface and accelerate the optimization of Indonesia's geothermal energy resources.

This study aims to enhance the accuracy and precision of MT exploration by utilizing improved techniques in signal processing and 3-D inversion. An MT time series denoising method that uses a neural network architecture is proposed. In building the denoising system, input and output data sets are synthesized using a 3-D forward modeling scheme. This research showcases the application of 1-D convolutional neural networks and long short-term memory algorithms to eliminate the typical noises affecting MT time series data, which results in a modular denoising system. The most appropriate and suitable neural network learning strategies are tested and evaluated using some criteria. The performance tests against synthetic and real field data show that the trained denoising modules can automatically identify noise patterns in unseen noisy data, improving the quality of MT time series data.

Regarding geothermal exploration in Indonesia, the Danau Ranau geothermal prospect area has a high geothermal potential. However, this area is located in

geologically complex regions, making it difficult to model the subsurface resistivity structure due to the high dimensionality. The inversion modeling practices that utilize the magnetotelluric impedance tensor and the tipper vector from the vertical magnetic transfer function are used to deal with complex geological conditions. Prior dimensionality analysis using phase tensor revealed that the MT data contains a high dimensionality distortion and shows significant horizontal geoelectrical variations. The 3-D MT inversion result effectively recovers the spread of highly conductive impermeable cap rock in the shallow depth with a maximum thickness of about 1,000 m. The inverted model was also able to localize the more resistive zone seated at about 1.5 km depth below the summit of Mt. Seminung, which serves as the reservoir for the geothermal fluids. The total area of the reservoir zone is approximately 16 km2. All the findings agree with the existing geological and geochemical survey data and can explain the hydrothermal activities in the Danau Ranau geothermal prospect area.

Another potential geothermal prospect in Indonesia is located in Mount Lawu, on the border of Central and East Java. The three-dimensional inversion of MT and gravity data in the Mount Lawu geothermal prospect is discussed. The idea is to jointly interpret 3-D subsurface resistivity and gravity models to image the existing geothermal system, including the structure of the reservoir, impermeable clay cap, hydrothermal fluid flow pathways, and the depth of the magmatic heat source. The results show that the geothermal system's primary location is about 2 km south of the fumarolic manifestation. That is evidenced by a highly conductive, low-density zone near the GL-08 MT station. The geothermal reservoir is located subsequently, characterized by intermediate conductivity and low density resulting from highly fractured rocks saturated by hydrothermal fluids. Despite the models' inability to definitively image the heat source, the models offer insights into the presence of a conducting zone where the heat is transferred to the reservoir system. Integrating MT and gravity subsurface models in this study has yielded a valuable understanding of the geothermal system in the Mount Lawu geothermal field.

As a conclusion of all the works done in this study, it is apparent that the modular time series denoiser works well as an alternative to filter out unwanted noises from the MT signal. The method was able to recover the clean signal without missing important information. In the later stages of data processing, the 3-D inversion of MT and the supporting data were able to delineate the subsurface conditions with regard to the

existing geothermal system in the Danau Ranau and Mount Lawu geothermal prospect area. Considering all the results, it is hoped that this research could contribute to a more effective geothermal exploration, in identifying potential energy sources to address Indonesia's rising demand for sustainable energy solutions.

Keywords: *magnetotelluric, geothermal, time series, resistivity, Indonesia.*

CONTENTS

LIST OF FIGURES

LIST OF TABLES

CHAPTER I
INTRODUCTION

1.1 Indonesia's Geothermal Potential and Challenges

Indonesia is located in a region where three tectonic plates coincide, making it a highly strategic location for geothermal energy production. The country has a significant amount of geothermal energy resources, which is why it is considered one of the richest sources of this renewable energy source. Geothermal energy is classified as renewable because it produces no harmful emissions during production. That makes it an environmentally friendly energy source that does not contribute to climate change. It is derived from the Earth's internal thermal energy that flows to the surface. This thermal energy includes the heat generated by the planet's initial formation and the radioactive decay of elements in the mantle and crust.

From a geological perspective, Indonesia has 76 historically active volcanoes, the highest number globally. That makes Indonesia an ideal location to explore the science of geothermal energy. Indonesia has vast geothermal resources, almost 40% of the world's total (Wilcox, 2012). The abundance of geothermal resources in Indonesia is due to the country's location on the Pacific Ring of Fire, which is characterized by active volcanoes, earthquakes, and tectonic activity (Suharmanto et al., 2015). According to the Indonesian Ministry of Energy and Mineral Resources, approximately 80% of geothermal sites in Indonesia are located in isolated active volcanic systems in the main islands. That means that geothermal energy has the potential to be a significant source of energy for the country. As per a report by ESDM (2020), the total composition of the geothermal potential is 23,765 MW, which includes 9,344 MW of resources and 14,421 MW of reserves distributed at 357 locations in Indonesia, as shown in Table 1.1.

Indonesia needs to build production wells to access subsurface heat and harness this abundant energy. Steam-gathering facilities and fracture systems must be integrated to transfer heat to the surface for clean and efficient geothermal energy production. When all these components are combined, they produce clean and efficient geothermal energy. However, it can be inferred from Table 1.1 that the number of unused geothermal potential is very high compared to the installed capacities. That is why geothermal exploration is still essential for the country's energy challenge.

Table 1.1. Indonesia's geothermal energy potential (ESDM, 2020)

Region	**Number of Location**	**Resource**		**Reserve**			**Total Potential**
		Speculative	*Hypothetical*	*Possible*	*Probable*	*Proven*	
Sumatra	101	2276	1551	3594	976	1120	9517
Java	75	1259	1191	3403	377	1820	8050
Sulawesi	91	1365	343	1063	180	120	3071
Bali - Nusa Tenggara	40	295	169	996	231	42.5	1733.5
Maluku - Papua	36	635	91	485	6	2	1219
Kalimantan	14	151	18	6	0	0	175

Geothermal exploration is critical in developing and utilizing geothermal energy in Indonesia. It involves a comprehensive study of geothermal resource areas to determine the reservoir depth, dimension, and boundary and to choose the most suitable and economically viable site for drilling. It is also necessary to estimate the temperature, volume, and permeability at depth and predict the intrinsic properties of the geothermal fluid. The exploration stage typically includes geological, hydrological, geochemical, and geophysical studies followed by exploratory drilling. Among all the studies mentioned above, geophysical study is the only technique to delineate the subsurface features related to geothermal systems. The rules of geophysical prospecting in geothermal exploration other than to locate the highly permeable zone are to image the controlling structural features, reservoir system, impermeable clay cap, up-flow zones, and the source of the geothermal heat (Gupta and Roy, 2007).

Geothermal prospects are commonly accompanied by geophysical anomalies that arise from variations in the physical properties of rocks and fluids within or close to the reservoir. Resistivity, density, porosity, magnetic susceptibility, seismic velocity, and temperature are geophysical exploration's most commonly used physical properties. The resistivity contrast is especially useful for exploration since a low resistivity anomaly typically indicates the zone above the reservoir, the main target for geothermal exploration. The reservoir has a higher resistivity value due to the formation of alteration products in a high-temperature system. Therefore, resistivity structure mapping up to a depth greater than 1,000 m is crucial for geothermal exploration, and the magnetotelluric method plays an important role in achieving that goal. This geophysical method is used to delineate the deep subsurface resistivity structure and has the potential to greatly improve reservoir imaging and the success rates of geothermal exploration. In Indonesia, successful magnetotelluric surveys could help the country develop and maximize its geothermal potential to meet its energy needs.

1.2 Magnetotelluric Method in Geothermal Exploration

Geothermal resources consist of a heat source and fluid phase in altered or structurally deformed rocks. Following this, geophysical resistivity methods become crucial for geothermal exploration. Subsurface resistivity is highly related to the properties of geothermal rocks, such as temperature and pressure, lithology, and porosity. It also highly depends on the types of geothermal fluids, such as the phase and salinity. The magnetotelluric (MT) technique is a primary tool among resistivity methods as it allows for coverage of a large area encompassing the geothermal system, great depth of investigation (compared to other resistivity methods that usually only reach a few hundred meters), and the necessary resolution to understand often complex geological settings in a geothermal system (Rodriguez et al., 2021). There are three main purposes of geothermal exploration using the MT method: (1) to image prospective geothermal features, (2) to define the geothermal reservoir boundaries, and (3) to locate the drilling targets (Spichak and Manzella, 2009). The MT method could achieve the abovementioned goals by mapping and modeling the resistivity structure beneath the geothermal field.

Figure 1.1 shows the typical model of a high-temperature magmatic geothermal system commonly found in Indonesia. In this system, the shallow magmatic intrusion heats the meteoric water that seeps into permeable zones through volcanic structures. The volcanic gases that mix with the infiltrating water in the permeable reservoir cause a significant increase in temperature, buoyancy, and mineral content. The reservoir system is typically located between 1 and 3 kilometers below the surface and has a temperature range of 215 to 315 °C (Rodriguez, 2021). As the geothermal fluids rise, they interact with the surrounding rocks, forming an impermeable clay cap that contains smectite and illite-rich layers. This cap prevents the geothermal fluid from reaching the surface, forcing it to flow upward and outward through existing fractures and faults until it reaches the surface as geothermal manifestations.

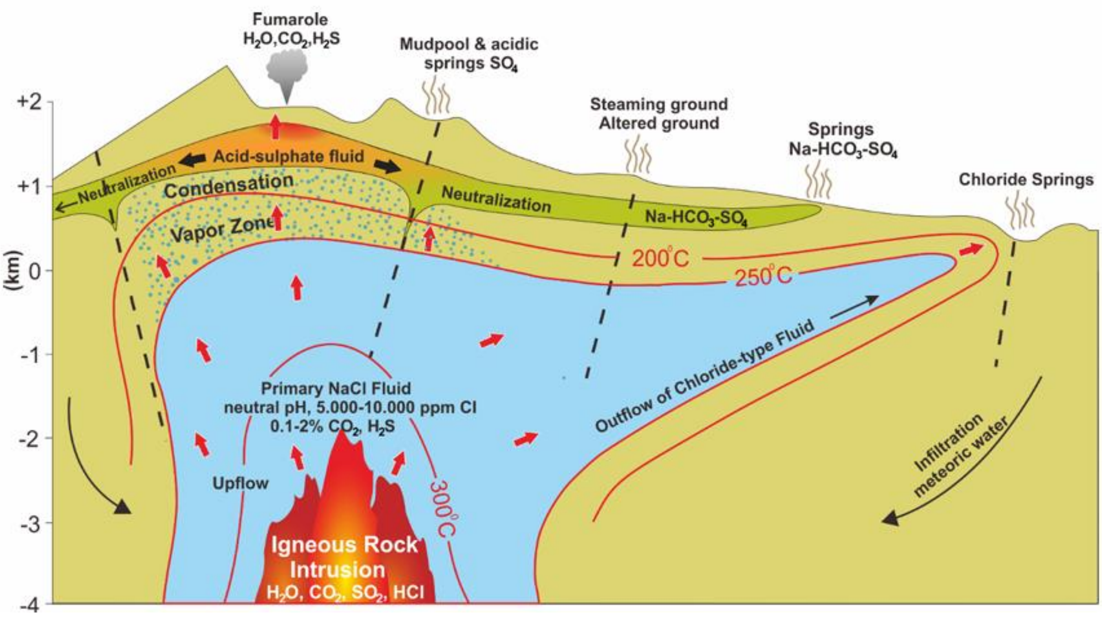

Figure 1.1. Schematic concept of a high-enthalpy geothermal system (from Utami, 2018).

As explained previously, geothermal systems have distinct components, each possessing a unique resistivity characteristic. The unaltered rock located near the surface typically comprises native volcanic rocks such as basalt and andesite, which exhibit high resistivity values and innate electrical current resistance. A geophysical signature frequently associated with a high-temperature geothermal system is a significantly low resistivity layer (< 10 Ωm) that overlays a moderately low resistivity layer (10 to 50 Ωm). These resistivity reactions are linked to the smectite-rich clay cap and the underlying reservoir that contains high chlorite and epidote content (Anderson et al., 2000; Lévy et al., 2018). At the deepest part, the relation between resistivity and temperature enables MT to detect the magmatic heat sources, especially when low resistivity magmatic intrusion (partially melting body) exists. These distinct electrical properties of the main components of geothermal systems become why the MT method is preferable for deep geothermal exploration.

The efficacy of the magnetotelluric (MT) technique in geothermal exploration within volcanic terrains is demonstrated by many scholarly investigations that have successfully imaged low-resistivity features associated with an impermeable cap, reservoir rocks, fluid pathways, and instances of geothermal heat source (Matsushima et al., 2020; Başokur et al., 2022; Marwan et al., 2021; Zhou et al., 2022; Di Paolo et al., 2020). MT surveys offer a significant benefit in their ability to generate images of resistivity structures at significant depths. That is especially important because most geothermal sources are several kilometers below the Earth's surface. By utilizing MT surveys, geologists and geothermal exploration companies can obtain detailed and accurate information about the electrical conductivity of rocks and fluids at great depths, which is a critical factor in identifying potential geothermal energy sources.

1.3 Research Background

The potential of geothermal energy to become the primary source of green energy in Indonesia and beyond has led to a significant focus on developing this energy source and attracting investments. In this regard, the success rate of surface or geothermal surveys is crucial in making informed decisions and ensuring optimal resource utilization. Table 1.1 shows that the areas with the highest geothermal potential, such as Sumatra and Java, are densely populated islands. That poses a challenge for magnetotelluric exploration, as it relies on natural electromagnetic fields and is highly susceptible to cultural electromagnetic interference. Conducting an MT survey in or near an urban area is likely to result in highly noisy data sets, rendering the collected data unusable and reducing the effectiveness of the MT exploration. On the other hand, utilizing such noisy data for further processing could be a malicious practice. To address this issue, finding a way to eliminate or reduce the effect of noisy and unusable data sets would benefit future exploration efforts.

As previously discussed, the subsurface geology in Indonesia is quite complex due to tectonic and volcanic activities within the country. Unfortunately, the magnetotelluric method is not immune to the effects of geologic distortions caused by this complexity. Considering the subsurface model's accuracy, another critical factor for successful geothermal exploration, adequate modeling techniques are necessary. That is to avoid any misleading results due to insufficient and inappropriate modeling efforts, which, in turn, can hinder the effectiveness of magnetotelluric exploration and delay the development or utilization of geothermal resources. Therefore, it is essential to employ suitable modeling strategies to obtain a reliable resistivity model of the subsurface and accelerate the optimization of Indonesia's geothermal energy resources.

1.4 Purpose of the Study

The general purpose of this study is to improve the reliability of the MT exploration by improving the time series signal processing and the three-dimensional inverse modeling. Signal processing has always been a challenging task, particularly when it comes to removing noise from data. However, utilizing neural networks to remove noise has several advantages over traditional methods. Firstly, it eliminates the need for a professional in signal processing as the machine can learn the noise pattern by itself. Secondly, using the trained networks ensures efficient separation between signal and noise of MT data in a short time. Finally, removing noise from the MT data prevents noise propagation, avoiding any disturbance to subsequent processes such as response function estimation and inversion modeling. In conjunction with the subsurface modeling, inverting the MT data alone could be insufficient due to its limitations (e.g., being prone to geological and electromagnetic distortions). Therefore, joining or combining other data sets is necessary to support and integrate with the resulting MT model.

Therefore, the specific aim of this study is threefold: first, to develop a cutting-edge MT time-series denoising method that effectively eliminates or reduces noise interference in recorded time series data. The second purpose is to create a subsurface resistivity model in complex geological settings by simultaneously inverting magnetotelluric impedance and the vertical magnetic transfer function. Finally, the last purpose is constructing a dependable geothermal conceptual model in a highly topographic area by integrating magnetotelluric and gravity data. These previous two objectives were applied to Indonesia's largest geothermal prospects, Danau Ranau and Mount Lawu.

1.5 Structure of the Thesis

The study and research that have been conducted are carefully written in this thesis and are presented systematically in six chapters as follows:

1. Chapter one provides the background story and introduces the research idea. It sheds light on the current situation of geothermal development in Indonesia, which inspired the topic. Additionally, I outline some problems encountered in geothermal exploration and present a proposed solution that will be further investigated in this research.

2. Chapter two presents a concise overview of the magnetotelluric method, covering key topics such as the electromagnetic field source, background principles, and potential noise sources. Additionally, I learn the data acquisition and processing procedures, including time series inspection and inversion modeling. By familiarizing ourselves with the fundamentals of the MT method in this chapter, I can better comprehend the subsequent content of this study, as MT is the primary technique employed throughout.

3. Chapter three explains the development of the MT noise removal modules, representing my research's first objective. This section offers a comprehensive breakdown of the process of building the denoising system, from synthesizing input and output data sets to the neural network training strategies. Additionally, I will demonstrate the effectiveness of the trained networks against both synthetic and real field data, both of which present significant challenges in terms of noise interference.

4. In chapter four of this thesis, I discuss the inversion modeling practices that utilize the magnetotelluric impedance tensor and the tipper vector from the vertical magnetic transfer function. I applied an inversion modeling strategy to explore the geothermal prospect in the Danau Ranau geothermal field. My discussion includes detailed data analysis, dimensionality and directionality, and the inversion modeling process. In the final portion of this chapter, I present the resulting subsurface resistivity model from the joint inversion and provide a detailed geological interpretation.

5. Chapter five presents the three-dimensional inversion of MT and gravity data in the Mount Lawu geothermal prospect. I commence my discussion by briefly outlining the geological and geochemical surroundings of the region,

followed by a comprehensive examination of my MT and gravity data analysis. In the final section, I deliberate on the inversion outcomes of each method and the advantages of integrating all models for effective geothermal exploration in this area.

6. In the last chapter, I present the conclusions of my research along with recommendations for improving the results.

1.6 Concluding Remarks

Thanks to its strategic location on the Pacific Ring of Fire, Indonesia boasts vast geothermal energy resources. Geothermal energy is an environmentally friendly energy source as it produces no harmful emissions. In order to explore the geothermal potential of a particular area, the magnetotelluric (MT) technique is an effective tool, especially in volcanic terrains. This technique generates images of resistivity structures to help identify potential geothermal energy sources at significant depths. However, the reliability of MT exploration can be improved through advanced time-series signal processing and 3-D inverse modeling. Therefore, this study aims to enhance the accuracy and precision of MT exploration by utilizing improved techniques in signal processing and 3-D inversion. That will allow for more effective geothermal exploration and identifying potential energy sources that can help meet the growing demand for sustainable energy solutions.

CHAPTER 2
THE BASICS OF MAGNETOTELLURIC METHOD

2.1 Introduction

The magnetotelluric (MT) method is a non-invasive and cost-effective geophysical exploration technique that involves measuring natural electromagnetic fields over a wide range of frequencies to reveal the subsurface electrical conductivity structure. This method primarily investigates geological features such as mineral deposits and maps the Earth's crust and upper mantle structure. By analyzing the signals recorded at the surface, geophysicists can obtain valuable information about the subsurface resistivity structure, which can help make important decisions related to resource exploration, engineering design, and environmental monitoring.

Tikhonov (1950) and Cagniard (1953) first introduced the MT method as a valuable tool for geophysical prospecting. Their research established a connection between the measured electric (E) and magnetic (H) fields and various materials' electrical resistivity. This breakthrough discovery enabled geoscientists to map the electrical resistivity beneath the Earth's surface based on measurements taken at its surface. The MT method has been extensively developed since its inception and applied in various geophysical exploration projects worldwide. Its non-invasive nature, great investigation depth, and the fact that it provides adequate resolution images of the subsurface make it a preferred method for shallow to deep earth explorations, especially for those related to electrical resistivity distribution.

. Electrical resistivity measures how much a material opposes the flow of electrical current. It is the inverse of electrical conductivity, measuring a material's ability to conduct electricity. In geothermal exploration, electrical resistivity is an important parameter since it helps determine the subsurface properties of the Earth's crust. By measuring the electrical resistivity of rocks and fluids, geophysicists can obtain valuable information about the presence and distribution of geothermal reservoirs, which are crucial for developing geothermal energy resources.

2.2 Theoretical Background of MT Method

To determine the electrical conductivity of the subsurface material, the fluctuation in the natural electric (E) and magnetic (H) fields in the orthogonal directions is measured. These electromagnetic waves have a wide range of wave periods, from 10^{-3} to 10^{5} seconds, and are exploitable for MT studies (Chave and Jones, 2012). The range of wave periods allows for investigating different depths and structures within the Earth's subsurface. For instance, shorter periods are useful for investigating shallow structures, while longer periods can penetrate deeper into the Earth's crust. The difference in depth penetration between signals with certain periods is related to the exponential decay of electromagnetic fields as they diffuse into a medium, described by the electromagnetic skin depth relation. In MT studies, the penetration depth of electromagnetic fields into the Earth is generally equivalent to one electromagnetic skin depth (δ), which can be approximated as

$$\delta(T) \approx 500\sqrt{\rho_a T}\,, \tag{2.1}$$

where ρ_a is the average resistivity of a homogeneous half-space, and T is the signal period. Thus, in order to obtain deeper information, one should extend the magnetotelluric sounding period. Compared to active EM or other resistivity methods, where the energy source and receiver configurations determine the probing depth, the MT technique boasts a greater capacity for imaging a wider spectrum of depths. The following subsections present a more detailed explanation of the source of the MT signal and how these signals are related to the subsurface electrical characteristics.

2.2.1 Source of Magnetotelluric Fields

Under the common assumption, MT source fields rely on two natural phenomena: lightning or thunderstorm activities and solar wind. These field sources produce short-period and long-period electromagnetic waves, respectively (Figure 2.1). Lightning activities produce a so-called Schumann resonance in the ionosphere, filled with ionized atmospheric gases (Kaufman and Keller, 1981). This event creates the energy, known as *sferics*, that travels in the Earth-ionosphere waveguide with a frequency greater than one cycle per second (> 1 Hz).

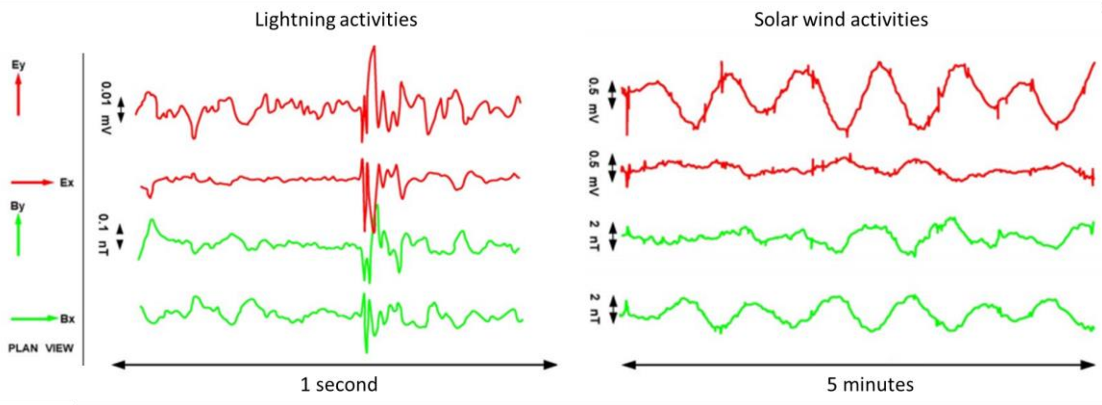

Figure 2.1. Samples of (left) high-frequency and (right) low-frequency signal recordings from two signal sources (from Unsworth, 2007).

The counterpart low-frequency (< 1 Hz) signal originates from the interaction between the earth's magnetic field and solar wind activity. Ionic streams emitted from the solar wind moving towards the Earth at a speed of more than 500 km/s interfere with the Earth's natural magnetic field. At that time, protons and electrons inside the plasma deflected in opposite directions and, thus, create the electric current. As these plasma groups move following the continuous solar wind activity and encounter the Earth's magnetosphere, they give rise to the time-varying EM waves (Kaufman and Keller, 1981). When these external energies reach the surface of the Earth, a portion of them is reflected back while the rest penetrates into the Earth. Since the Earth is a good conductor, this leads to the induction of electric currents, known as telluric currents, generating a secondary magnetic field, which is considerably small but measurable.

Figure 2.2 shows the power spectrum of the natural magnetic field variation produced by the two signal sources. The inductive source mechanism of low-frequency and high-frequency signals leaves very low-energy signals around 1 Hz or the *dead band* frequency (see the inset in Figure 2.1). The effect of this situation is usually observable in the MT curve, where the data quality around the dead band is relativity poor. Several assumptions about the MT signal sources are made to simplify and accommodate the electromagnetic induction on the Earth's material. Conservative and analytic properties are assigned to all MT electromagnetic fields away from their sources. Electromagnetic fields created by ionospheric current systems far from the Earth's surface can be considered uniform and plane-polarized electromagnetic waves that hit the Earth almost vertically. The MT technique relies heavily on the plane wave assumption, which assumes that the exciting source remains time-invariant. This assumption leads to calculating the impedance tensor using the electric and magnetic fields that are orthogonal to each other, which is unchanged over time (Cagniard, 1953).

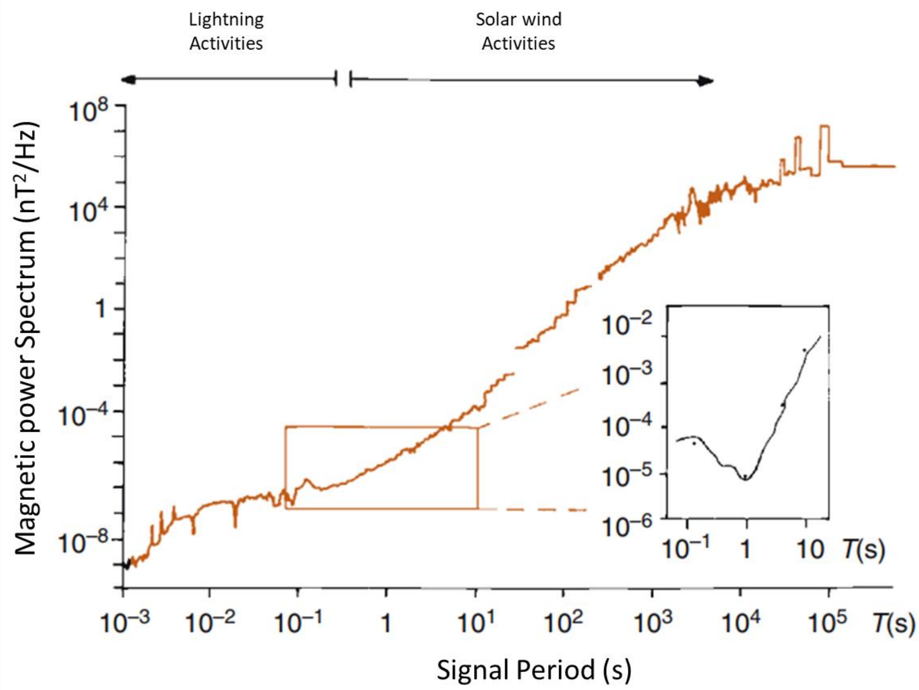

Figure 2.2. Typical power spectrum of the varying natural magnetic signal for short and long periods (from Simpson and Bahr, 2005).

2.2.2 EM Fields and Subsurface Resistivity

The natural electromagnetic signals are assumed to travel downward through the earth's surface as plane waves. While most of these signals are reflected, a small portion diffuses into the earth, inducing an electromagnetic field to materials based on their conductivity. That means that the conductivity of the earth's material can be determined by solving Maxwell's equations, where the propagation of EM fields is described as follows,

$$\nabla \cdot \boldsymbol{E} = \frac{q}{\varepsilon}\,, \tag{2.2}$$

$$\nabla \cdot \boldsymbol{H} = 0\,, \tag{2.3}$$

$$\nabla \times \boldsymbol{E} = -\mu \frac{\partial \boldsymbol{H}}{\partial t}, \tag{2.4}$$

$$\nabla \times \boldsymbol{H} = \sigma \boldsymbol{E} + \varepsilon \frac{\partial \boldsymbol{E}}{\partial t}, \tag{2.5}$$

where $\boldsymbol{E}$ and $\boldsymbol{H}$ are the electric and magnetic fields, respectively. The symbols μ, ε, and σ represent magnetic permeability, dielectric permittivity, and conductivity, respectively. The first equation is Gauss's Law, which explains the electric field in a closed boundary. The second equation states that the total magnetic field in a closed boundary equals zero, implying no magnetic monopole. Eq. (2.4) is Faraday's Law, which describes the relation between the time-varying magnetic and induced electric fields (Figure 2.3a). The last part of the modified Maxwell's equations states that a magnetic field could be produced from a conducting current and displacement current (Figure 2.3b). The wave equations for electric and magnetic fields are solved using their vector identities. Therefore,

$$\nabla^2 \boldsymbol{E} = \mu\sigma \frac{\partial \boldsymbol{E}}{\partial t} + \mu\varepsilon \frac{\partial^2 \boldsymbol{E}}{\partial t^2}\,, \tag{2.6}$$

$$\nabla^2 \boldsymbol{H} = \mu\sigma \frac{\partial \boldsymbol{H}}{\partial t} + \mu\varepsilon \frac{\partial^2 \boldsymbol{H}}{\partial t^2}\,. \tag{2.7}$$

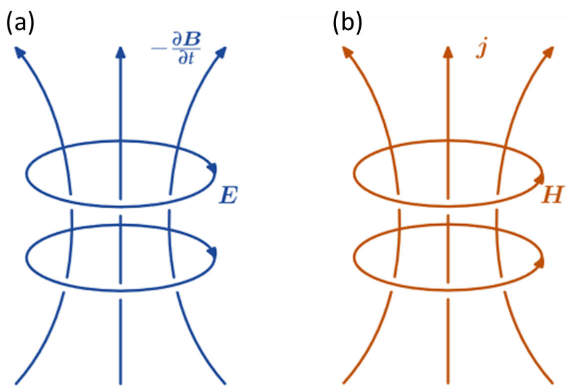

Figure 2.3. (a) Induced electric field due to a change in magnetic field and (b) induced magnetic field due to electric current (from Vozoff, 1991)

The partial differential equations above inferred that the EM fields exponentially vary with time. Assuming a sinusoidal form of time variation, the equations above can be rewritten using the formula of harmonic wave oscillation as follows,

$$\nabla^2 \boldsymbol{E} = (i\omega\mu\sigma - \omega^2\mu\varepsilon)\boldsymbol{E} \ , \tag{2.8}$$

$$\nabla^2 \boldsymbol{H} = (i\omega\mu\sigma - \omega^2\mu\varepsilon)\boldsymbol{H} \, , \tag{2.9}$$

where ω is the angular frequency. The assumption is made in a quasi-static approximation that the change in displacement current is so insignificant that it can be disregarded when compared to the conductivity value. Therefore, the second element in Eq. (2.6) and (2.7) of the right-hand side could be neglected. This approximation allows for simplification of the equations as follows,

$$\nabla^2 \boldsymbol{E} = i\omega\mu\sigma\boldsymbol{E} \ , \tag{2.10}$$

$$\nabla^2 \boldsymbol{H} = i\omega\mu\sigma\boldsymbol{H} \, . \tag{2.11}$$

The electromagnetic field is assumed to be a plane wave, and its intensity remains constant in the horizontal (x and y) direction. However, this electromagnetic field is attenuated in the vertical direction (z), and the amplitude should be zero at the infinite depth (Naidu, 2012). Thus, the elemental solutions for Eq. (2.10) and (2.11) are as follows,

$$E_x = Ae^{-i\omega\mu\sigma z} = Ae^{-kz} \ , \tag{2.12}$$

$$H_y = -\frac{1}{i\omega\mu}\frac{\partial E}{\partial z} = \frac{k}{i\omega\mu}(Ae^{-kz}) \ , \tag{2.13}$$

where A is the amplitude constant and k denotes the wave number. Eq. (2.12) is the diffusion equation, which implies that the EM field is not propagating inside the earth but rather diffuses into the earth. Note that the depth and the material's conductivity affect the EM field attenuation.

The primary response function in MT observation is an impedance tensor (***Z***), the ratio between electric and magnetic fields that oscillate perpendicularly. In other words, this function describes a linear relationship between the measured electric and magnetic fields. For instance, the impedance tensor component that is calculated from the electric field in the x direction and its orthogonal magnetic field in the y direction is as follows,

$$Z_{xy} = \frac{E_x}{H_y} = \frac{i\omega\mu}{k} \, , \tag{2.14}$$

where E_x denotes the electric field intensity in the x direction (measured in mV/km), and Hy is the magnetic field intensity in the y direction (measured in nT). From the characteristic impedance, the frequency-dependent apparent resistivities (ρ_a) related to the x and y-axis could be deduced as follows,

$$\rho_{axy} = \frac{|Z_{xy}|^2}{\omega\mu}, \tag{2.15}$$

and its phase (φ) is described as

$$\varphi_{xy} = arg\left(Z_{xy}\right). \tag{2.16}$$

Equation 2.13 describes the resistivities of the earth's non-uniform layer, which exhibit apparent values dependent on frequency and the chosen approach, whether 1-D, 2-D, or 3-D. An inversion process and several pre-inversion data processing steps are necessary to obtain an accurate subsurface resistivity value. These steps aim to eliminate noise, distortions, and uncertainties that may arise.

2.3 Magnetotelluric Noises

In any electromagnetic measurement, it is crucial to distinguish between signal and noise sources, as there are usually more noise sources than signal sources. Cultural noise arises from various sources, with electrical power being a major contributor. That refers to the present-day seepage from power cables, electric pumps, and electric trains, which create a magnetic field that goes around in a circle through the earth, acting as a source of electromagnetic waves. In longer-period magnetotelluric data, spikes and step-like bursts can result from power sources, and electric channels are more prone to this type of noise. Moving ferrous metals or other magnetic material near the magnetic field sensor can introduce noise into the magnetic channels. Loosely connected cables can result in spikes and/or dead traces, while wind or sea-generated vibrations of the magnetic field sensor will cause random variations in the magnetic channels.

Any or all of the above noise sources may be present with the MT signal, resulting in compounded responses in the recorded time series. To obtain accurate measurements, electromagnetic cultural noise must be characterized and corrected. Figure 2 .4 presents some of the most common MT noise patterns, and Chapter 3 further explains these noise types.

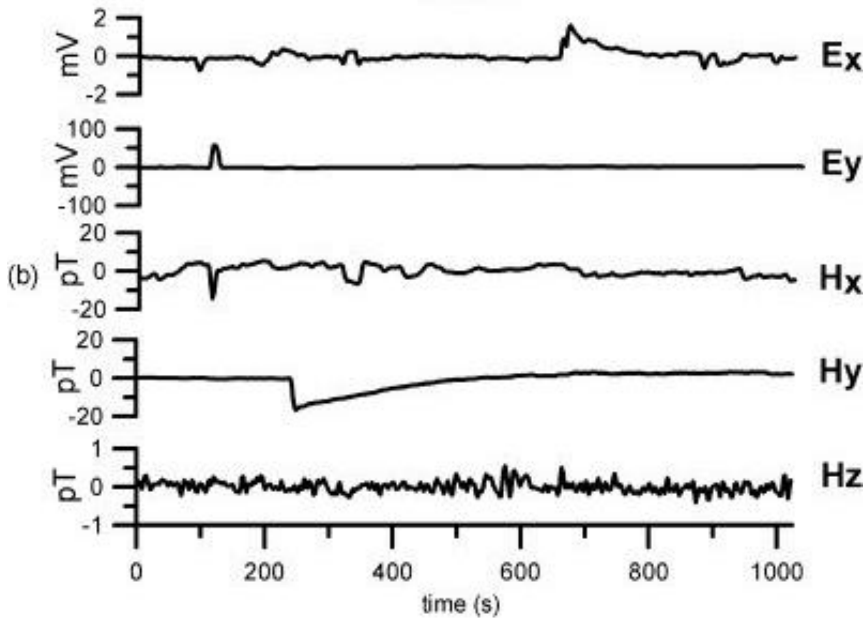

Figure 2.4. Common noise types and patterns in a time window of MT recording; Ex and Hy show the signal step and its decay. Different types of spikes or impulses are shown in Ey and Hx. Hz contains random noises (from Manoj and Nagarajan, 2003).

2.3.1 Cultural Noise Sources

When dealing with geophysical datasets, power line signals can often cause interference, which is the most common type of noise. Electromagnetic fields around the power line's base frequency (50 Hz in Indonesia) and its higher harmonic frequencies are created when electricity flows through power lines in populated areas. The sinusoidal signal caused by the noise from the power grid system oscillates at the base frequency. This signal tends to fluctuate around the base frequency due to changes in energy supply and demand (Figure 2.5). There must be a balance between the electricity generated by power plants and the energy consumed by consumers in the grid at all times. In the event of an increase in power demand beyond what the generators supply, the generators' rotational energy is tapped into to make up for the deficit. That causes a decrease in grid frequency as the generators slow down. Additionally, the signal's amplitudes and phases constantly change for similar reasons. Power-line noise is highly polarized and can affect one orthogonal measurement direction more than the other.

Figure 2.5. Fluctuation in utility frequency in the European grid within 5 minutes from 1:00 to 1:05 UTC on April 28th, 2024 (downloaded from mainsfrequency.com at that time).

Another source of cultural noise is near-field magnetic interference from automobiles. Cars emit magnetic fields, which can create disturbances in nearby MT recording stations. This interference can be particularly problematic for sensitive sensors, such as those used in the MT survey. Additionally, vibrations generated by traffic can create seismic disturbances, leading to inaccuracies and signal distortion. That can be especially challenging for the MT sensors that depend on stable and accurate readings. In addition to these noise sources, errors caused by sensors and instruments can also contribute to cultural noise. For instance, sensor noise and noise from electronic circuits are unpredictable and unrelated to signal power. That makes it difficult to distinguish and evaluate signals accurately.

2.3.2 Natural Noise Sources

Meteorological noise is a common phenomenon caused by different factors, one of which is wind. When the wind blows, it can move trees and bushes, causing their roots to generate seismic noise that can interfere with the sensors and adversely impact the measured fields. This effect is particularly noticeable in high-frequency magnetic field measurements, where wind-induced disturbances can cause significant fluctuations in the readings. Therefore, it is essential to consider the potential impact of wind on the measurements and apply appropriate correction techniques to ensure accurate and reliable data.

Another source of meteorological noise is lightning. Distant lightning activities can act as high-frequency signal sources, but local lightning can be more problematic. The intensity of the local lightning is much stronger than the distant ones, which can saturate telluric amplifiers. Telluric amplifiers are used to amplify the signals received from the ground but are sensitive to nearby sources of electromagnetic interference. That can cause an increase in the noise level, affecting the accuracy and reliability of the data obtained from the magnetic field.

2.3.3 MT Signal Coherence

Noise in MT data can be classified into incoherent and coherent noise. Incoherent noise is noise in the electric field, the magnetic field, or both and cannot be attributed to the transfer function. The local seismic noise, for example, may not be recorded in all measurement channels and, therefore, is incoherent. Meanwhile, coherent noise affects the input (magnetic field) and output (electric field) coherently, as if the noise in both measured fields is correlated and shows linearity (Manoj and Nagarajan, 2003). Lightning activities close to the MT recording stations and signals from nearby power distribution lines may interfere with electric and magnetic signals simultaneously and directly affect both channels. Therefore, the resulting noise will be coherent and linear.

Quantifying the level of random noise in data can be done by analyzing the linear correlation between electric and magnetic field components, known as coherence. Coherence is a dimensionless variable whose values range between 0 and 1, where the upper limit represents completely coherent signals. The coherence is a spectral ratio comprising the cross-correlated electric and magnetic field spectra (Simpson and Bahr, 2005). Coherence (ψ) between the electric field (E) measured in the i direction and magnetic field (H) in the j direction can be calculated as follows,

$$\psi_{ij} = \frac{\langle E_{ij}^{*} H_{ij} \rangle}{\sqrt{\left(\langle E_{ij}^{*} E_{ij} \rangle \langle B_{ij}^{*} B_{ij} \rangle\right)}}, \tag{2.17}$$

where the symbol * denotes the complex conjugate.

The coherence value in magnetotelluric (MT) surveys helps to identify local noise sources that are not uniform across the source field, resulting in a low coherence value. This noise source is known as the "cultural effect" and can affect the quality of the data collected in MT surveys. Therefore, coherence threshold values are often used as a criterion to filter out noise from the data. However, it is important to note that relying solely on coherence values may not always be sufficient to identify noise sources in complex environments, where the noise may be correlated across different electromagnetic components. Therefore, it is essential to have a comprehensive understanding of the geological and geophysical context of the survey area to properly interpret the coherence values and identify any potential noise sources.

2.4 Data Acquisition and Processing

2.4.1 Data Acquisition

The magnetotelluric time series consists of five simultaneously measured components of the Earth's electromagnetic field: two orthogonal components of horizontal electric fields (E_x, E_y) and three orthogonal components of the magnetic field (H_x, H_y, H_z). Two non-polarizable electrodes are placed at right angles to measure potential differences in both directions. Three induction coil magnetometers measure the magnetic field in the x, y, and z directions. These sensors' behavior and data collection are set in the main acquisition unit (see Figure 2.6).

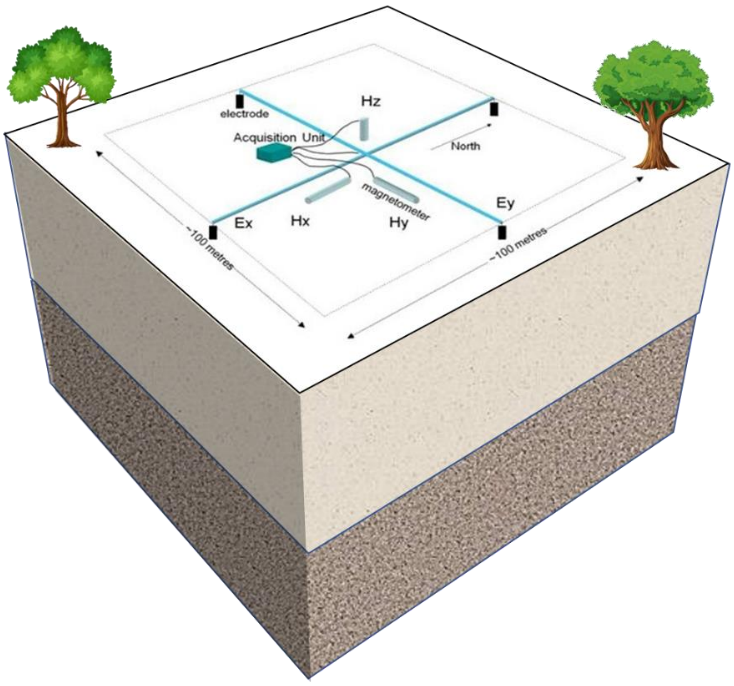

Figure 2.6. Configuration of MT instruments for data acquisition.

When conducting MT measurements, taking readings with overlapping broad ranges of frequencies is common practice. These readings are usually taken at several different intervals (sampling rate) to ensure a comprehensive dataset is obtained while maintaining effective data storage. Figure 2.7 shows an example of a 2 s time series recorded in different sampling intervals. The data points in Figure 2.7 from top to bottom are 4800, 300, and 30, respectively. The measurement process continues until an adequate number of stacks are obtained. The number of sample data points in each stack is chosen according to the maximum signal period of interest. When surveying in a noisy area, more stacks are needed. The stacking and averaging process helps to cancel out noise included in individual time stacks.

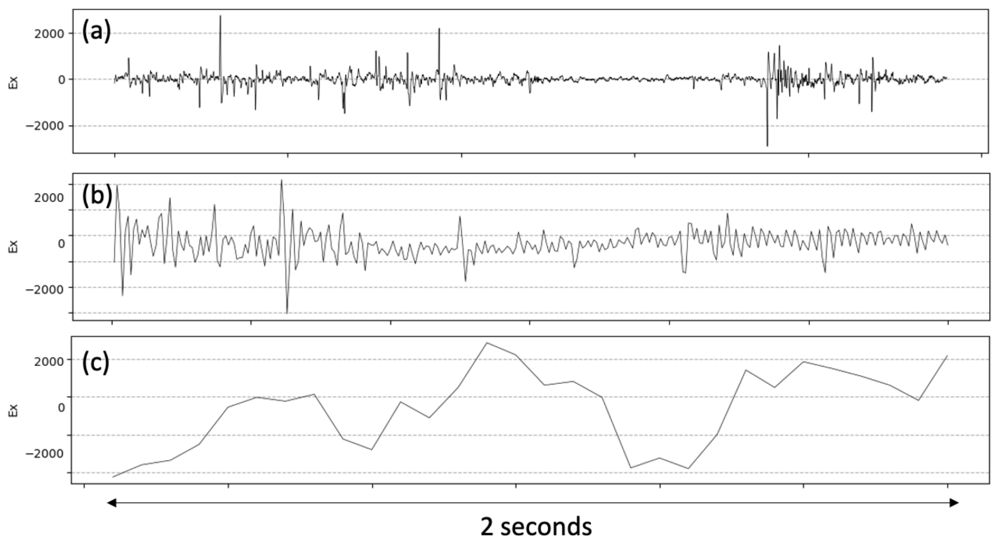

Figure 2.7. Example of 2-second-long electric field time series data with (a) 2,400 Hz, (b) 150 Hz, and (c) 15 Hz of sampling frequencies.

2.4.2 Spectra Estimation

The first step of MT data processing is transforming the time series data (e.g., $E_x(t)$ and $H_y(t)$) into the frequency domain and calculating the Fourier coefficient. The Fourier coefficient is a complex-valued quantity representing signal amplitude for different frequencies. Suppose a digital time series (X) is divided into N data point intervals (Figure 2.7a; N = 4,800), where each point is represented as x_j where j = 1, N. The Fourier coefficient ($\bar{X}$) at one frequency in this time series is described by

$$\bar{X}_m = a_m + ib_m\,, \tag{2.18}$$

where m = 1, 2, …., N/2, and a and b are real and imaginary parts of the coefficient. First, it is assumed that the discrete function x_j is a superposition of signals of different finite frequencies as follows,

$$x_j = \sum_{m=0}^{M} \left(a_m \cos\left(m \frac{2\pi j}{N} \right) + b_m \sin\left(m \frac{2\pi j}{N} \right) \right) + \delta x_j\,, \tag{2.19}$$

where M is the number of coefficients. Using the orthogonality of the trigonometric function theorem, the coefficients a and b can be calculated using the discrete Fourier transform (DFT) as follows,

$$a_m = \frac{2}{N} \sum_{j=0}^{N-1} x_j cos\left(\frac{2\pi j}{N} \right), \tag{2.20}$$

$$b_m = \frac{2}{N} \sum_{j=0}^{N-1} x_j sin\left(\frac{2\pi j}{N} \right). \tag{2.21}$$

Note that to perform the DFT on discrete time series data, it is necessary to have the x_j = 0 at the margin of the time segment. That can be obtained by performing trend removal followed by a windowing method. (Simpson and Bahr, 2005).

The next step is to calculate power spectra and cross spectra from the individual field spectrum ($\bar{X}$) at each evaluation frequency. The power spectrum of the X field component is as follows,

$$\langle \bar{X}\bar{X}^* \rangle = \frac{1}{I} \sum_{i=1}^{I} \bar{X}_i \bar{X}_i^*\,, \tag{2.22}$$

where I is the total number of individual field spectra for one evaluation frequency in a time window.

In Eq. (2.22), $\bar{X}$ can be either electric or magnetic spectrum components ($\bar{E}_x, \bar{E}_y, \bar{H}_x, \bar{H}_y,$ or $\bar{H}_z$). Therefore, it can be used to calculate either each pair's power spectra or cross spectra. A stacking procedure is then applied to evaluate the spectra from all the time windows. Additionally, a weighting scheme that could improve the response function estimation can be attributed to this process, either by hand editing or a robust technique (Egbert and Booker, 1986).

2.4.3 Response Function Estimation

The next crucial step of magnetotelluric data processing is estimating the response function (e.g., the impedance tensor (***Z***)). The electrical impedance is the measured ratio between the electric and magnetic field components. According to Eq. (2.14), the impedance tensor can be estimated by evaluating the following relation:

$$\begin{bmatrix} E_x \\ E_y \end{bmatrix} = \begin{bmatrix} Z_{xx} & Z_{xy} \\ Z_{yx} & Z_{yy} \end{bmatrix} \begin{bmatrix} H_x \\ H_y \end{bmatrix}, \tag{2.23}$$

where Z_{xx}, Z_{xy}, Z_{yx}, and Z_{yy} are the components of the impedance tensor. Impedance is a complex quantity and can be separated as follows,

$$\begin{bmatrix} Z_{xx} & Z_{xy} \\ Z_{yx} & Z_{yy} \end{bmatrix} = \begin{bmatrix} X_{xx} & X_{xy} \\ X_{yx} & X_{yy} \end{bmatrix} + i \begin{bmatrix} Y_{xx} & Y_{xy} \\ Y_{yx} & Y_{yy} \end{bmatrix}, \tag{2.24}$$

where ***X*** and ***Y*** are the real and imaginary parts of the complex impedance tensor (Thiel, 2008). Linear expansion of Eq. (2.23) and the presence of measurement noise yields,

$$E_x = Z_{xx} H_x + Z_{xy} H_y + \delta Z \ , \tag{2.25}$$

$$E_y = Z_{yx} H_x + Z_{yy} H_y + \delta Z \ , \tag{2.26}$$

where δZ is the electric field noise, which is assumed to follow the Gaussian (normal) distribution.

The least-square technique is the basic statistical processing method used to minimize noise's effect in impedance tensor estimation. The least square method finds the optimum solution when the sum of squared residuals is minimum. For example, the residual between the observed electric field spectra ($\bar{E}_x$) and predicted ($\bar{E}_{xp}$) is as follows,

$$\sigma = \sum_{k=1}^{K} \left| \bar{E}_{x,k} - \bar{E}_{xp,k} \right|^2 = \sum_{k=1}^{K} \left(\bar{E}_{x,k} - \bar{E}_{xp,k} \right) \left(\bar{E}_{x,k} - \bar{E}_{xp,k} \right)^* , \tag{2.27}$$

where K is the number of available spectra. Substituting Eq. (2.25) into Eq. (2.27) yields,

$$\sigma = \sum_{k=1}^{K} \left(\bar{E}_{x,k} - \bar{Z}_{xx}\bar{H}_{x,k} + \bar{Z}_{xy}\bar{H}_{y,k}\right)\left(\bar{E}_{x,k} - \bar{Z}_{xx}\bar{H}_{x,k} + \bar{Z}_{xy}\bar{H}_{y,k}\right)^{*}. \tag{2.28}$$

Then, to get the optimum solution by minimizing the residual function, one must satisfy the following conditions:

$$\frac{\partial\sigma}{\partial Z_{xx}} = 0 \ and \ \frac{\partial\sigma}{\partial Z_{xy}} = 0. \tag{2.29}$$

By setting the derivative of σ for each complex component of Z_{xx} to 0, and solving the partial differential equation yields,

$$\sum_{k=1}^{K} \bar{E}_{x,k}\bar{H}_{x,k}{}^{*} = \bar{Z}_{xx}\sum_{k=1}^{K} \bar{H}_{x,k}\bar{H}_{x,k}{}^{*} + \bar{Z}_{xy}\sum_{k=1}^{K} \bar{H}_{y,k}\bar{H}_{x,k}{}^{*} . \tag{2.30}$$

Then, by performing a similar procedure to another component (Z_{xy}) and minimizing the residuals between E_y and E_{yp} for Z_{yx} and Z_{yy} components, the following equation is obtained:

$$\sum_{k=1}^{K} \bar{E}_{x,k}\bar{H}_{y,k}{}^{*} = \bar{Z}_{xx}\sum_{k=1}^{K} \bar{H}_{x,k}\bar{H}_{y,k}{}^{*} + \bar{Z}_{xy}\sum_{k=1}^{K} \bar{H}_{y,k}\bar{H}_{y,k}{}^{*} , \tag{2.31}$$

$$\sum_{k=1}^{K} \bar{E}_{y,k}\bar{H}_{x,k}{}^{*} = \bar{Z}_{yx}\sum_{k=1}^{K} \bar{H}_{x,k}\bar{H}_{x,k}{}^{*} + \bar{Z}_{yy}\sum_{k=1}^{K} \bar{H}_{y,k}\bar{H}_{x,k}{}^{*} , \tag{2.32}$$

$$\sum_{k=1}^{K} \bar{E}_{y,k}\bar{H}_{y,k}{}^{*} = \bar{Z}_{yx}\sum_{k=1}^{K} \bar{H}_{x,k}\bar{H}_{y,k}{}^{*} + \bar{Z}_{yy}\sum_{k=1}^{K} \bar{H}_{y,k}\bar{H}_{y,k}{}^{*} . \tag{2.33}$$

The solutions for the impedance tensor could be estimated by combining the equations from Eq. (2.30) to Eq. (2.33), followed by averaging the power and cross spectra as follows,

$$Z_{xx} = \frac{\langle \bar{E}_x\bar{H}_y^*\rangle\langle \bar{H}_y\bar{H}_x^*\rangle - \langle \bar{E}_x\bar{H}_x^*\rangle\langle \bar{H}_y\bar{H}_y^*\rangle}{\langle \bar{H}_x\bar{H}_y^*\rangle\langle \bar{H}_y\bar{H}_x^*\rangle - \langle \bar{H}_x\bar{H}_x^*\rangle\langle \bar{H}_y\bar{H}_y^*\rangle}\,, \tag{2.34}$$

$$Z_{xy} = \frac{\langle \bar{E}_x\bar{H}_y^*\rangle\langle \bar{H}_x\bar{H}_x^*\rangle - \langle \bar{E}_x\bar{H}_x^*\rangle\langle \bar{H}_x\bar{H}_y^*\rangle}{\langle \bar{H}_y\bar{H}_y^*\rangle\langle \bar{H}_x\bar{H}_x^*\rangle - \langle \bar{H}_y\bar{H}_x^*\rangle\langle \bar{H}_x\bar{H}_y^*\rangle}\,, \tag{2.35}$$

$$Z_{yx} = \frac{\langle \bar{E}_y \bar{H}_y^* \rangle \langle \bar{H}_y \bar{H}_x^* \rangle - \langle \bar{E}_y \bar{H}_x^* \rangle \langle \bar{H}_y \bar{H}_y^* \rangle}{\langle \bar{H}_x \bar{H}_y^* \rangle \langle \bar{H}_y \bar{H}_x^* \rangle - \langle \bar{H}_x \bar{H}_x^* \rangle \langle \bar{H}_y \bar{H}_y^* \rangle}, \tag{2.36}$$

$$Z_{yy} = \frac{\langle \bar{E}_y \bar{H}_y^* \rangle \langle \bar{H}_x \bar{H}_x^* \rangle - \langle \bar{E}_y \bar{H}_x^* \rangle \langle \bar{H}_x \bar{H}_y^* \rangle}{\langle \bar{H}_y \bar{H}_y^* \rangle \langle \bar{H}_x \bar{H}_x^* \rangle - \langle \bar{H}_y \bar{H}_x^* \rangle \langle \bar{H}_x \bar{H}_y^* \rangle}. \tag{2.37}$$

The formula above can provide reliable results only if two specific conditions are met: (1) the residuals follow a normal distribution, and (2) the magnetic field is unaffected by noise. If these conditions are not met, other methods, such as remote reference or robust processing, can be used to estimate the response function. However, these methods still have limitations when dealing with coherent noises or high signal-to-noise ratios. Therefore, a more effective solution is to remove the noise from the time series data before processing, especially when dealing with noisy data.

2.4.4 Inversion Modeling

Geophysical inversion is a technique that helps us to obtain information about the subsurface distribution of physical property from data collected in the field. After estimating the response functions, the next step is to find a subsurface model that fits these functions and is also geologically plausible. In MT exploration, inverse modeling aims to generate an image of the resistivity distribution beneath the measurement site related to physical properties such as rock or fluid properties. However, it's important to note that geophysical inversion only provides an approximate model rather than an exact physical property distribution. The technique works best when there is sufficient contrast between the target structure and the surrounding geology and when the data are sensitive to the target structure, meaning that the geophysical response from that structure is evident in the data. Finally, the parameters used in the inversion process need to be set appropriately to achieve the desired results.

The majority of geophysical inversion algorithms function by minimizing an objective function (ϕ) concerning the physical parameter model ($\boldsymbol{m}$):

$$\phi(\boldsymbol{m}) = \phi_d(\boldsymbol{m}) + \lambda \phi_m(\boldsymbol{m}), \tag{2.38}$$

where ϕ_d is the data misfit, ϕ_m is the model misfit, and λ is the regularization (trade-off parameter). The data misfit term is a crucial component in geophysical inverse problems.

It plays an important role in ensuring that the predicted data from the model fits the observed data. The data misfit is commonly represented as the L2-norm, which is given by:

$$\phi_d(\boldsymbol{m}) = \|\boldsymbol{W_d}[\boldsymbol{F}(\boldsymbol{m}) - \boldsymbol{d}]\|^2, \tag{2.39}$$

where $\boldsymbol{F(m)}$ is the predicted data, $\boldsymbol{d}$ is the observed data, and $\boldsymbol{W_d}$ denotes the data weighting matrix influenced by the data uncertainty (standard deviation or variance). To avoid over-fitting and stabilize the inversion process, the weighting matrix is designed to not focus solely on fitting the large values at the expense of the small values.

The second term of the right-hand side of Eq. (2.38) is the model misfit, which ensures that the recovered model contains a reasonable geological image. It usually consists of two factors: smallness misfit (ϕ_{small}) and smoothness misfit (ϕ_{smooth}), so that:

$$\phi_m(\boldsymbol{m}) = \phi_{small}(\boldsymbol{m}) + \phi_{smooth}(\boldsymbol{m}), \tag{2.40}$$

with:

$$\phi_{small}(\boldsymbol{m}) = \beta_s\|\boldsymbol{W_s S_s}[\boldsymbol{m} - \boldsymbol{m_0}]\|_2^2, \tag{2.41}$$

and

$$\begin{aligned}\phi_{smooth}(\boldsymbol{m}) = \beta_x\|\boldsymbol{W_x G_x}[\boldsymbol{m} - \boldsymbol{m_0}]\|_2^2 &+ \\ \beta_y\left\|\boldsymbol{W_y G_y}[\boldsymbol{m} - \boldsymbol{m_0}]\right\|_2^2 &+ \\ \beta_z\|\boldsymbol{W_z G_z}[\boldsymbol{m} - \boldsymbol{m_0}]\|_2^2 &,\end{aligned} \tag{2.42}$$

where $\boldsymbol{W_s}$ represents the model cell weighting matrix and $\boldsymbol{W_x}$, $\boldsymbol{W_y}$, and $\boldsymbol{W_z}$ are smoothness weighting matrices. These weighting matrices could be defined independently or adjusted based on depth and distance. The smoothness matrices **G** defines the behavior of model gradients in the x, y, and z directions. The parameter β controls the importance of each direction.

The last parameter in the objective function (Eq. 2.38) is the regularization parameter, λ, which determines the contribution of data and the model to the objective function. This parameter ensures that the data and the model are equally important in the final estimate of the physical property model. It is usually scaled to the total number of input data and automatically recovered through an optimization routine to ensure that the desired level of accuracy is achieved.

In this study, I mostly used a three-dimensional inversion scheme to analyze the MT data, which required a high level of detail. I conducted the inversion process using the ModEM software (Kelbert et al., 2014), a flexible Fortran-based inversion program. This program can be used for various data types, and its basic inversion components can be reused and extended to various cases. Additionally, ModEM can be applied to parallel computation.

The objective function implemented in ModEM software gives a reasonable resistivity model parameter ($\boldsymbol{m}$) that fits the given data matrix ($\boldsymbol{d}$) by minimizing the penalty function (Φ) as follows,

$$\Phi(\boldsymbol{m},\boldsymbol{d}) = \left(\boldsymbol{d}-\boldsymbol{F}(\boldsymbol{m})\right)^T \boldsymbol{C_d}^{-1}\left(\boldsymbol{d}-\boldsymbol{F}(\boldsymbol{m})\right) + \lambda(\boldsymbol{m}-\boldsymbol{m_0})^T \boldsymbol{C_m}^{-1}(\boldsymbol{m}-\boldsymbol{m_0}). \quad (2.43)$$

$\boldsymbol{C}_d$ and $\boldsymbol{C}_m$ are the covariance of the data errors and the model, respectively.

2.5 Concluding Remarks

The MT method is a non-invasive geophysical exploration technique that measures natural electromagnetic fields over a wide range of frequencies to reveal the subsurface conductivity structure. It is commonly used to investigate geological features, such as mineral deposits, and map the Earth's crust and upper mantle structure. By analyzing the surface signals, geophysicists can obtain valuable information about the subsurface resistivity structure, which can help make important decisions related to resource exploration, engineering design, and environmental monitoring. The electrical resistivity of a material is its opposition to the flow of electrical current, and it plays a critical role in determining the subsurface properties of the Earth's crust in geothermal exploration. By measuring the electrical resistivity of rocks and fluids, geophysicists can obtain valuable information about the presence and distribution of geothermal reservoirs, which are essential for developing geothermal energy resources.

The MT signal travels downward as plane waves through the earth's surface, and its conductivity can be determined by solving Maxwell's equations. However, noise from different sources can influence the MT signal, making it challenging to obtain accurate measurements. Therefore, electromagnetic cultural noise must be characterized and corrected to obtain reliable results. Careful data acquisition, time series inspection, spectra and transfer function estimation, and inversion modeling are necessary for a successful MT survey.

CHAPTER 3
MAGNETOTELLURIC TIME SERIES MODULAR DENOISER BASED ON ARTIFICIAL NEURAL NETWORK

3.1 Introduction

The magnetotelluric (MT) method, a geophysical technique that uses natural electromagnetic field variations, is crucial for producing images of the resistivity structure beneath the Earth's surface. Its applications span a wide range, from tectonic studies to geothermal exploration, which is the primary focus of this study. The MT method's ability to probe the subsurface at significant depths is highly esteemed. As detailed in Chapter 2, the MT method's source can be attributed to two main factors - solar wind activity and distant lightning activities. These sources generate low and high-frequency signals, respectively. The MT signal, characterized by a wide band frequency, non-stationarity, and very low amplitude, poses unique challenges for researchers to ensure its quality and reliability.

The MT responses are subject to natural and artificial electromagnetic noises, strongly influencing magnetotelluric time series recordings. These noises often contaminate the observed electric and magnetic fields coherently, making them difficult to separate and remove (Ritter et al., 1998). Due to this problem, the reliability of the magnetotelluric method to accurately image the subsurface resistivity becomes questionable. Many attempts have been made to address this issue. Remote reference processing uses noise-free reference data synchronously recorded at a remote station to discriminate local noise in the observation station (Gamble et al., 1979). However, current industrialization makes finding a suitable remote station difficult (Pedersen, 1982). Using an inappropriate remote station may result in correlated noise between local and remote sites, which makes it ineffective (Ritter et al., 1998).

In the frequency domain, robust processing is a method used to filter out noises by analyzing the coherence of data (Egbert and Booker, 1986). This method is effective when the signal and noise are not correlated. However, it becomes counterproductive when dealing with cultural EM noises since they are usually correlated and affect most parts of the recording (Weckmann et al., 2005). Some advancements in MT noise removal are directly influenced by time series form (Larnier et al., 2016; Neukirch and Garcia, 2014). One of the attempts is the signal-noise separating method using wavelet-transform (Trad and Travassos, 2000). In this approach, wavelet coefficient thresholding filters out the unusual observations related to noisy portions of the data. However, the method risks eliminating the useful signal component (Li et al., 2021).

In recent years, researchers have explored the use of machine and deep learning algorithms to tackle electromagnetic data processing beyond the traditional statistical approach. For instance, Manoj and Nagarajan (2003) utilized feed-forward neural networks to automate the denoising process on single and inter-channel reading. Larsen et al. (2022) applied a neural network to remove electromagnetic noise originating from the power line grid system. The result was significantly better than using a notch filter. Carbonari et al. (2018) proposed a method that uses a Self-Organizing Map (SOM) neural network to eliminate cultural noise from a distorted MT signal. Li et al. (2022) used sparse coding and dictionary learning to enhance the quality of MT data by eliminating strong ambient noise. Zuo et al. (2022) and Zhang et al. (2022) adopted the residual network to filter out the noise caused by anthropological activities. These studies effectively removed specific types of electromagnetic noise up to a certain threshold. However, the overall noise is typically the combination of several cultural and natural noise sources, which is more difficult to eliminate.

This study proposes a denoising method that utilizes artificial neural network (ANN) technology. This method will enable the computer to learn the unique pattern of noises and use it to differentiate similar noises when it encounters noisy data autonomously. Since each noise source has its distinct pattern, I propose a modular system that can be customized according to the type of noise contaminating the data (Figure 3.1). This modular system will allow us to train the network separately based on the different types, patterns, and noise characteristics using various methods, architectures, and training schemes. By doing so, I hope to develop a denoising method that is highly effective in cleaning noisy data and can be easily adapted to different types of noise sources. This chapter will follow step-by-step, from synthesizing the time series and noises, data pre-processing, training, and performance test to applying the proposed method to the synthetic and real MT data.

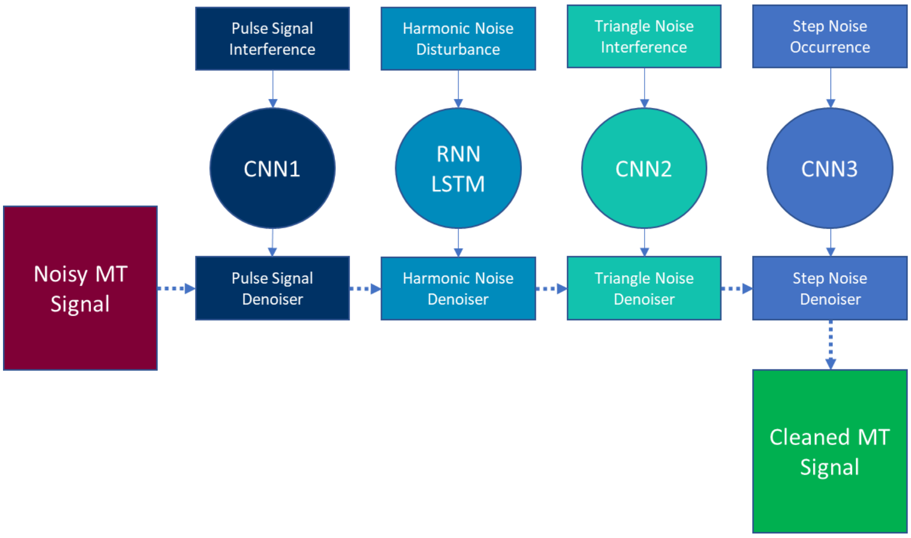

Figure 3.1. Schematic diagram of modular NN denoiser.

3.2 Data and Methods

3.2.1 Synthetic Time Series Data Sets

Synthesizing MT time-series data provides a noise-free signal that is favorable for the training phase. It is also needed for comparison and performance evaluation. The time-domain form of a single-frequency (ω) EM field at a time (t) is as follows,

$$\boldsymbol{x}(\omega, t) = \boldsymbol{A}_x \cos(\omega t + \Phi_x) \ , \quad (3.1)$$

where $\boldsymbol{x}$ represents the electric or magnetic field signal in the frequency domain. $\boldsymbol{A}_x$ denotes the signal amplitude while Φ_x is the signal phase. Therefore, a time series containing N frequency can be reconstructed as follows,

$$\boldsymbol{X}(t) = \sum_{k=1}^{N} \boldsymbol{x}(\omega_k, t) \ , \quad (3.2)$$

where $\boldsymbol{X}(t)$ is the time series after superposition.

To generate a synthetic signal comparable to the actual MT time-series data, a Delphi code given by Wang et al. (2023b) is used. The synthesizing process involved simulating a time series of small segments for a single frequency and polarization source at a particular location. Following several distinct simulations, the composite of each single-frequency time series was combined to produce the final data for the MT time series. I used the same 3-D earth model from the COMMEMI Project (Zhdanov et al., 1997), a three-layered earth with two anomalous bodies at the top layer (Figure 3.2). Eight MT stations were placed in different places so that the MT data for each station is unique. The MT time series were forward modeled using the modified ModEM software (Kelbert, 2014; Wang et al., 2023b). This process resulted in the frequency-dependent electric and magnetic fields from 2 orthogonal polarization sources for three sampling frequencies: 2400, 150, and 15 Hz. For this current study, I only used high-frequency data as I limited the scope to consider noises affecting the high-frequency part.

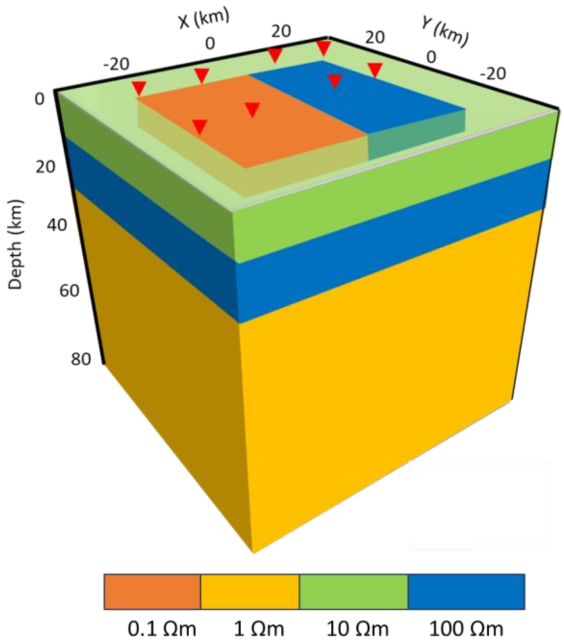

Figure 3.2. Synthetic model for forward modeling the MT time series.

3.2.2 Simulation Noise

Suppose a recorded MT data with the sampling frequency of f_s. The signal is observed for N/f_s second long, where N is the total number of data points. The n^{th} data point $S(n)$ can be expressed as

$$S(n) = X(n) + \varepsilon(n) \ , \tag{3.3}$$

where $X(n)$ and $\varepsilon(n)$ are clean signal and noise data points, respectively. The noise described here could come from different sources. According to Manoj and Nagarajan (2003), the typical MT noise sources and patterns, other than uncorrelated random noise, are spikes (pulse signals), step bursts, triangle signals, and harmonic sinusoidal noises (see Figure 2.4). I simulate those noise patterns along the length of the synthetic time series and combine them to obtain the noisy signal (Figure 3.3).

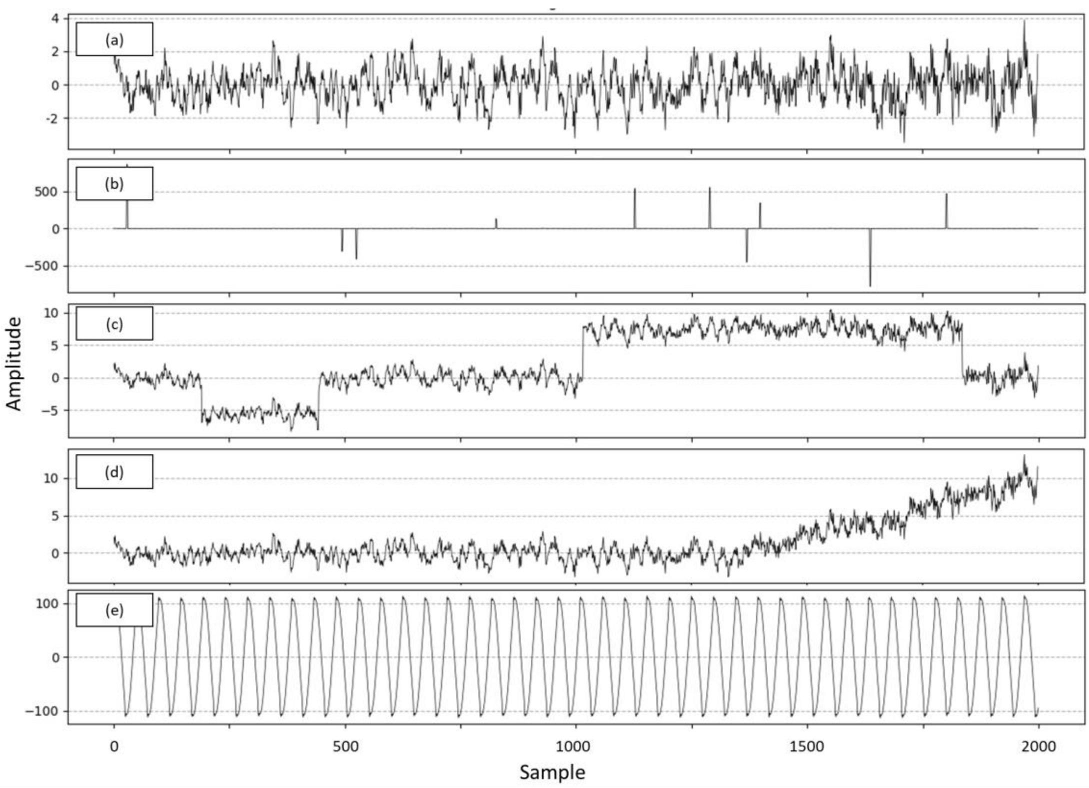

Figure 3.3. Synthetic time series data consists of (a) clean samples and those contaminated by (b) impulse signal, (c) step noise, (d) triangle noise, and (e) harmonic noise.

Impulse noise is interference that exhibits a spiky pattern and endures only for a few data samples. The sources of this type of noise include local lightning, thunderstorms, or power sources. A distinctive feature of this interference is that its amplitude is much higher than the amplitude of the original signal. In order to simulate this noise, I observe its behavior on real field data. To create synthetic impulse noise, I randomize its occurrence and establish the extreme values of its properties. For instance, the maximum amplitude is 1,000 units, the maximum duration is 1/1000 s, and the maximum occurrence is 25% in one time segment. An example of the impulse noise that can be added to the clean signal is illustrated in Figure 3.3b.

The issue with the power source can also lead to a different type of noise, referred to as step noise or noise bursts. This type of noise can persist for longer periods, often spanning hundreds of data samples, and cause the signal amplitude to appear as a plateau or depression. In certain instances, it may also manifest as a square wave. To simulate this type of noise, I introduce randomness in the occurrence, with each noise event lasting between 0.5 and 1 second. The noise amplitude is determined randomly, ranging between -100 and 100 units for each event. Figure 3.3c depicts an example of the step noise present during a 2-second recording interval.

In MT time series recordings, it is not uncommon to observe triangular noise patterns caused by the charge and discharge of power. This type of noise is prevalent in both urban and rural areas. To replicate this phenomenon, I generated a charge-discharge-like noise lasting up to hundreds of time samples (up to 0.8 seconds) with a maximum amplitude of 100 data units. A maximum of 3 triangle peaks are permitted for each time window segment. An illustration of the resulting noise pattern is displayed in Figure 3.3d.

The last type of noise incorporated in this research is harmonic noise emanating mainly from power lines. This type of noise typically arises from imbalances in the power transmission and distribution system. When the power line signal interferes, it takes on a sinusoidal form that matches its base frequency (usually 50 or 60 Hz) and higher harmonics (10 or more). Traditional notch filtering methods can be ineffective since the utility frequency fluctuates around the base frequency. To properly determine the base frequency and the number of higher harmonic interferences, I analyzed sample data collected from a contaminated farm (as depicted in Figure 3.4). I also adjusted the amplitude of the harmonic signal accordingly. The magnitude spectrum of the synthetic harmonic noise is presented in Figure 3.3e.

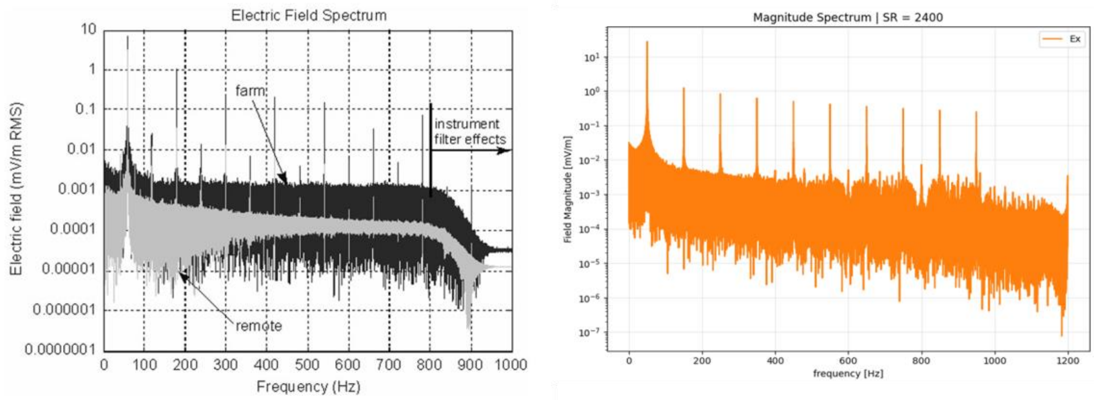

Figure 3.4. A comparison of the (left) electric field spectrum from a farm and a remote site (from Pellerin et al., 2004) and the field spectrum from harmonic noise simulation was made for this study.

3.2.3 Deep Learning Algorithms

I train several deep neural networks for each of the noise types. Each network model will specifically learn each noise pattern and remove it from the signal. I made it modular so that each denoiser model can be used separately based on the type of noises that interfere with the MT signal. Not all noises are usually present in a time segment. If needed, the noisy MT signal will undergo some of the denoiser models. Two neural network algorithms used in this research are 1-D convolutional neural network (1-D CNN) and recurrent neural network with long short-term memory (RNN-LSTM).

3.2.3.1 One Dimensional CNN

Convolutional Neural Networks (CNNs) generally refer to the 2-D version of this deep learning algorithm. The advantage of using CNN is that it can extract the spatial features from the data using its kernel or filter. For example, CNN can detect edges and the distribution of colors in the image, which makes these networks very robust in processing, such as classification or recognition and other similar data that contain spatial properties. In 2-D CNN, the kernel or filter slides in two dimensions during the convolutional process through all the image pixels. The input data is usually 3-D because each pixel in an image can contain colors (e.g., RGB) that give depth to an image (Figure 3.5).

The 1-D CNN follows a different approach, where the kernel slides along a single direction and extracts the features through the convolution process. That makes it suitable for processing 1-D array data, such as geophysical time series data. For instance, if an accelerometer measures seismic acceleration in all three axes (x, y, and z), with seven data points in each axis, the 1-D CNN can detect anomalies individually or all at once. In the latter case, the accelerometer data becomes two-dimensional (7×3), with the first dimension being time-steps and the second being the acceleration values in the three axes. As depicted in the upper part of Figure 3.5, the kernel (convolutional filter) moves along the data in only one dimension: the time axis.

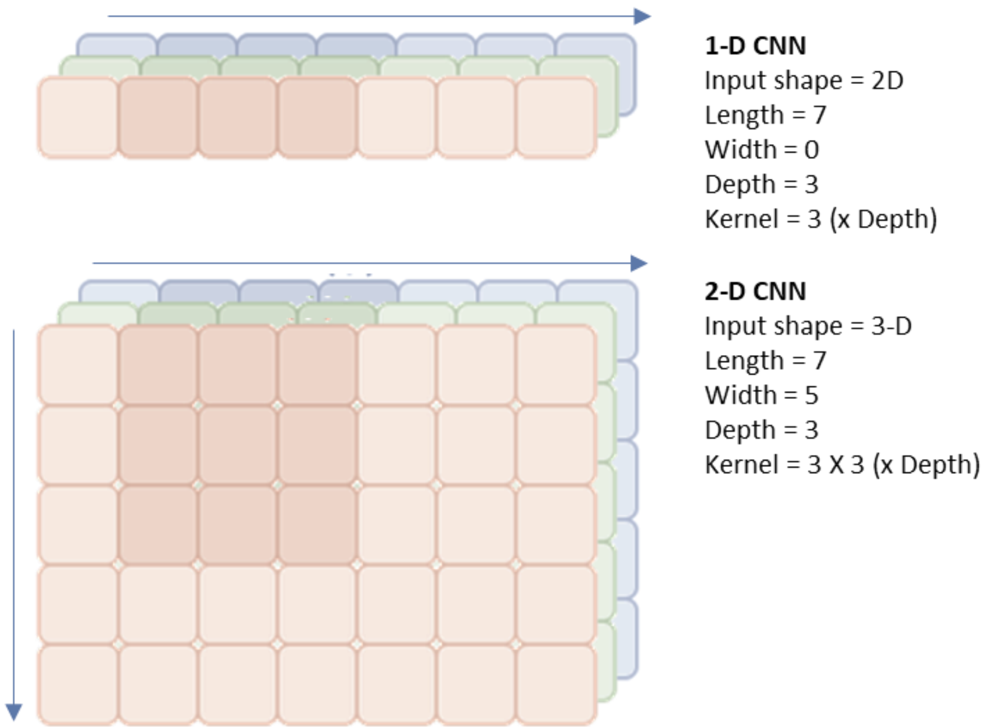

Figure 3.5. Differences between inputs of 1-D and 2-D CNN. Arrows indicate the kernel movement direction.

3.2.3.2 Recurrent Neural Network – LSTM

Recurrent neural networks, or RNNs for short, are an essential type of neural network that is particularly effective for processing time series data. Their structure typically consists of a repeating chain of neural network modules, making them capable of efficiently handling sequential information. In sequential input data, each time step is dependent on the ones that came before it, in which the current output (Y_t) is copied to be used to join the next input (X_{t+1}) for the subsequent process (see Figure 3.6).

Long Short-Term Memory Networks (LSTM) are a specialized form of RNNs capable of learning and remembering long-term dependencies. LSTM networks possess the unique ability to control the flow of information, permitting the network to learn and retain specific information while disregarding others. In Figure 3.6, each line represents a complete vector that transmits data from one node to another. The yellow boxes indicate the learning activation function. The yellow parts signify pointwise operators, such as addition and multiplication. Note that outputs are copied and re-joined in the network for the next data input (X_{t+1}).

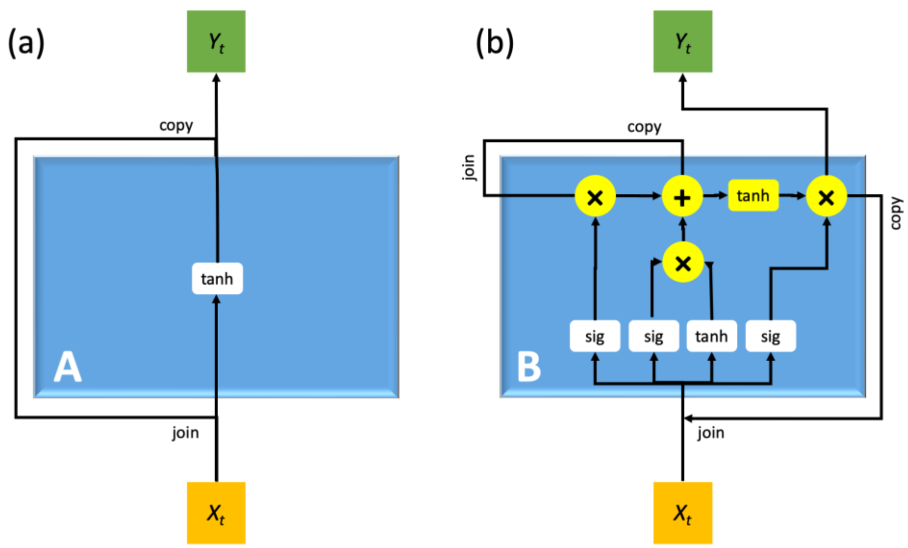

Figure 3.6. Repeating module in (a) standard RNN and (b) RNN-LSTM.

3.3 Neural Network Training and Test

3.3.1 Training Scheme

The objective of training the neural network is to establish a correlation between the noiseless and noisy data. I expect the neural network to distinguish between the two datasets and learn the noise pattern that sets them apart. Before training, the data must be prepared to ensure it is suitable for neural network inputs and outputs. That involves subjecting the noiseless and noisy data to a time windowing process, whereby the time series data is segmented into recordings of seconds. It is worth noting that although the neural network can extract features from multiple time signals recorded simultaneously, I have refrained from doing so in this case. That is because each channel, especially the electric and magnetic channels, has a different unit; they may contain various types of noise, and the impact of noise on different channels is still not understandable.

Prior to processing data in the network, it is crucial to normalize it to guarantee accuracy and efficiency. My approach involved implementing two distinct normalization methods based on signal-noise amplitudes. For the majority of cases, I relied on the maximum absolute scaler from the SciPy library. Nonetheless, I discovered that Z-score normalization was more effective when the noise amplitude greatly surpassed the actual signal, a conclusion supported by the training and validation loss observed during the training process. Furthermore, determining the appropriate hyperparameters is critical to neural network training. I engage in trial and error because there are no guidelines for selecting the optimal hyperparameters. I optimize the hyperparameters at each iteration of the training while simultaneously evaluating the training and test results. I employ distinct hyperparameters for each denoiser category, which will be elaborated on in subsequent subsections.

The denoising method's predictive performance is evaluated by comparing the correlation and misfit of the noisy and denoised signals to the noise-free signal. The correlation (*CC*) is evaluated as follows,

$$CC = \frac{\sum_{i=1}^{N} x_c(i) x_d(i)}{\sqrt{\sum_{i=1}^{N} x_c(i)^2 \sum_{i=1}^{N} x_d(i)^2}}, \tag{3.4}$$

where x_c is the clean sample, and x_d is the noisy or denoised sample. N denotes the total number of samples in a time window. I utilize the signal-to-noise ratio as an additional means of assessing the performance of the modular denoiser. This quantitative measurement is employed to determine the level of noise present within a signal. The SNR represents the ratio between the power of the useful signal and the desired signal or noise present within time series data. Decibels are used to express the SNR, with positive values greater than 1 indicating a stronger signal-to-noise ratio, while negative values less suggest a heavy interference of noise within the signal. The SNR between the noisy or denoised sample and the clean sample is calculated as follows,

$$SNR = 20log_{10}\left(\frac{\|x_c(n)\|_2}{\|x_c(n) - x_d(n)\|_2}\right). \tag{3.5}$$

3.3.2 Spike Reduction

Impulse noise usually appears as peaks or spikes with amplitudes significantly higher than the norm. I leverage this anomaly to train the neural network to recognize and remove these spikes from the noisy signal automatically. To ensure the normalization of the dataset, I employ Z score normalizations, which involve calculating the mean and standard deviations for both the input and output. I split my datasets into training and testing sets, with a ratio of 4:1.

My approach to removing impulse noise involves using a five-layered architecture with one input layer, one output layer, and three hidden layers of a 1-D CNN with a sigmoid activation function between them. I have included a batch normalization layer between the layers to maintain stability during training. The final layer is a fully connected layer with a tanh function that links the convolutional layer with the output label. I have compiled the model using a dynamically adjusting learning rate with an initial value of 0.001 and a decay rate of 90% while using Adam optimizers and mini-batch training mode. The aim is to minimize the loss function, which is determined by calculating the predicted and labeled data's mean absolute error (MAE). The training and validation loss functions are shown in Figure 3.7.

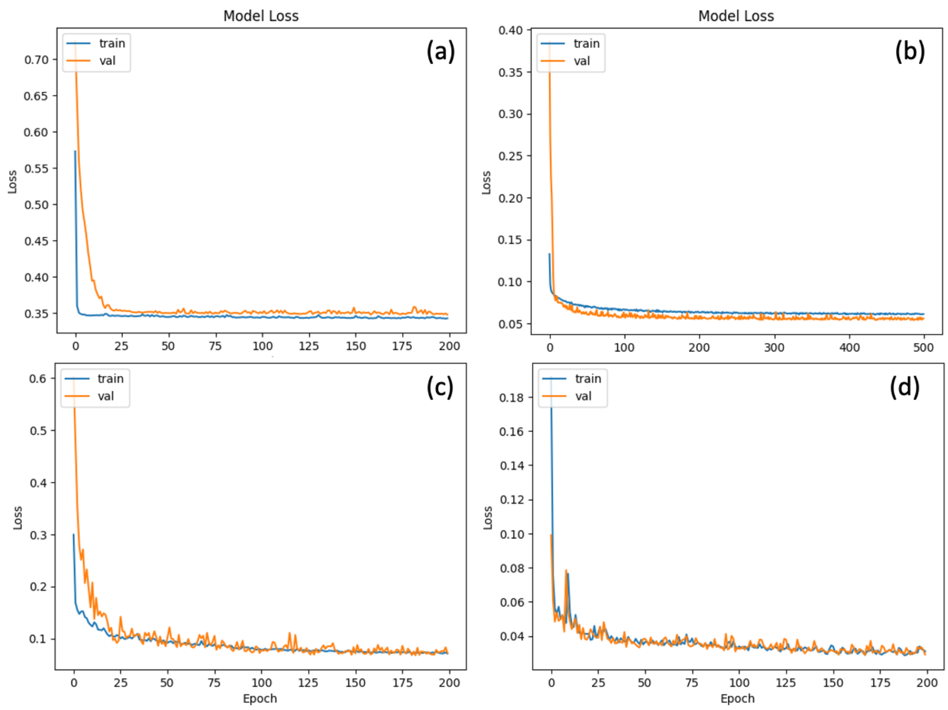

Figure 3.7. Training and validation losses for four denoising models: (a) impulse noise, (b) step noise, (c) triangle noise, and (d) harmonic noise.

The test results for the trained neural network to eliminate the impulse signal are displayed in Figure 3.8. Upon examining the time series on the left-hand side of Figure 3.8, it is apparent that the algorithm effectively removes spikes from the noisy signal. Comparing the predicted signal to the noise-free ground truth signal reveals similarities. The correlation coefficient and signal-to-noise ratio (right-hand side of Figure 3.8) indicate that the noise removal algorithm performs well on impulse noise, significantly increasing their respective values (from less than 0.1 to more than 0.9). The signal-to-noise ratio significantly improves from an average minus -34 dB to only -4 dB. That indicates that the algorithm designed for removing impulse noise was trained successfully. It is now ready to be applied to eliminate similar noises from new data.

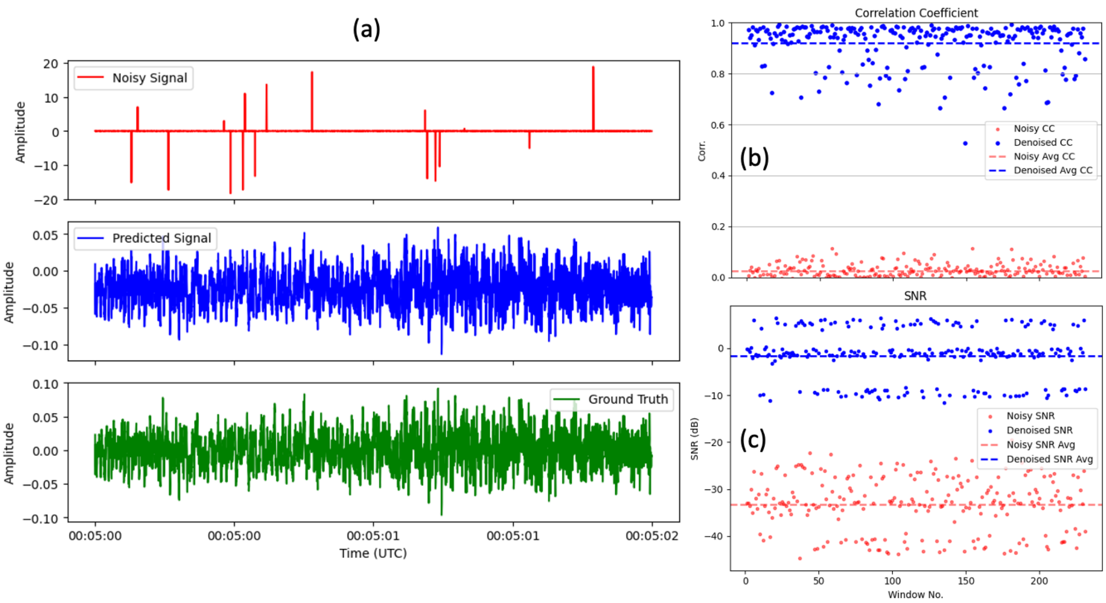

Figure 3.8. Prediction test results for impulse noise removal showing (a) the comparisons between noisy and predicted signals, (b) the correlation coefficient, and (c) the SNR between noisy and denoised signals.

3.3.3 Step Noise Removal

Step noise is usually characterized by a sudden jump or amplitude shifting over time. To easily distinguish this behavior, I take the first difference value of the signal in a time window. By taking the first difference value, the shifting in amplitude turns into an impulse-like signal, which can be easily observed using the same training strategies I used earlier to remove signal spikes. The first difference (ΔX) is calculated with a simple formula as follows,

$$\Delta X(t) = X(t+1) - X(t). \tag{3.6}$$

After performing the first difference calculation on the entire time windows, the preprocessed data is ready to be fed into the convolutional neural network model. This model has the same architecture and learning parameters as the previous case. However, in the output layer, the predicted data is represented by the first difference value rather than the actual time series value. To obtain the complete time series data, it's necessary to reverse the first difference process on the prediction result. Given that the MT time series data is nonstationary, the predicted time series data may contain a linear trend that needs to be removed from the result.

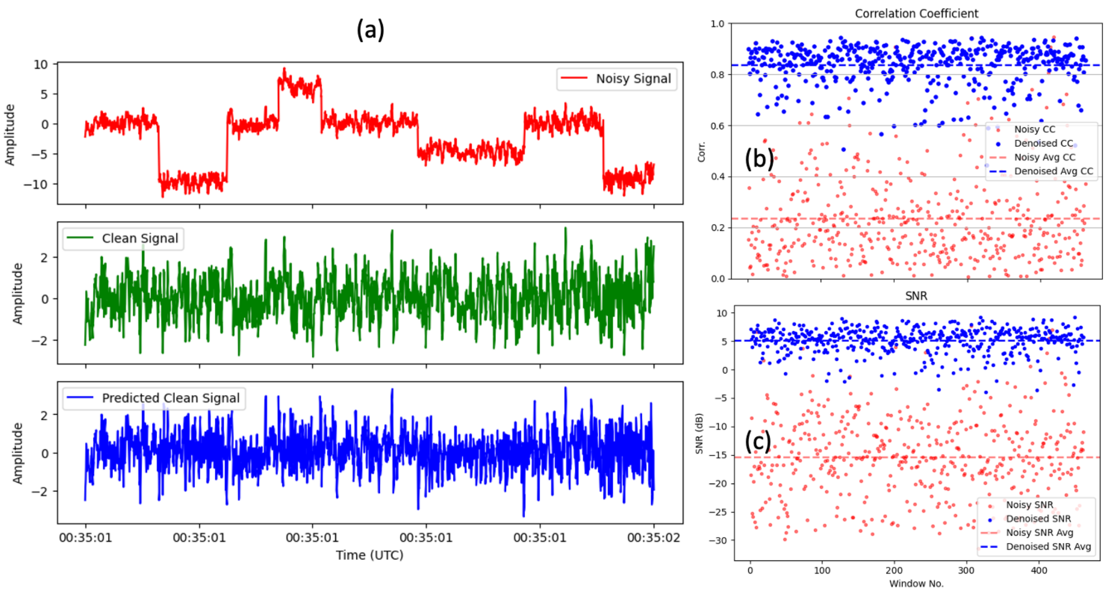

Figure 3.9. Prediction test results for step noise removal showing (a) the comparisons between noisy and predicted signals, (b) the correlation coefficient, and (c) the SNR between noisy and denoised signals.

Figure 3.9 showcases the prediction test results. The image's left-hand side compares the noisy signal, the projected clean signal, and the noiseless signal. The figure shows the correlation coefficient and signal-to-noise ratio on the right-hand side. Based on the test results, the step noise removal module's performance is exceptional, eliminating amplitude shifting caused by the steps. Additionally, the predicted clean signal closely resembles the noiseless signal. The correlation coefficient between the noisy and clean signals is about 0.2, which increases to approximately 0.9 on average after denoising. Similarly, the signal-to-noise ratio indicates that the step noise removal module improves the signal quality, increasing the average signal-to-noise ratio from -15 dB to 5 dB.

3.3.4 Triangle Noise Removal

A triangle noise can often be detected in a time series by observing the charged discharge behavior. This type of noise is characterized by a continuous increase or decrease in the signal amplitude, followed by a sudden drop or spike. To eliminate this type of noise from an MT time series, I have developed a convolutional neural network model consisting of three consecutive layers. The sizes of these layers are 128, 64, and 32, respectively, and the kernel filter sizes are 7×7, 5×5, and 3×3, respectively. A fully connected layer is attached to the output layer at the end of the model. Before implementing the neural network, it is necessary to preprocess the training data to obtain accurate results. Here, I normalized the data using Z score normalization, which involves calculating the mean and standard deviation of the data in a time window. This technique helps to normalize the data by subtracting the mean and dividing by the standard deviation, resulting in a distribution with a mean of zero and a standard deviation of one as follows,

$$X_n(t) = \frac{X(t) - \mu_x}{\sigma_x}, \tag{3.7}$$

where μ_x represents the mean value of the time series X and σ_x denotes the standard deviation of the data. Once the input data is normalized, it can be fed into the neural network, with the noisy signal in the input layer and the noise-free signal in the output layer. This process helps to train the network to recognize and distinguish between noisy and noise-free signals, resulting in improved accuracy and performance.

Figure 3.10 displays the outcome of the predicted signal with the removal of noise on the left-hand side. A time segment is exhibited within the figure where the charge-discharge behavior's effect is eliminated. By comparing the predicted signal's result to the noise-free signal in the same time segment, I can confidently conclude that the triangle signal removal process was successful. The correlation coefficient's value and the signal-to-noise ratio corroborate this assessment, as they agree. The correlation coefficient's average value has significantly increased from less than 0.05 to 0.9, while the signal-to-noise ratio has improved from -5 to 8 dB. This result must be further evaluated using new noisy datasets from synthetic models and real field surveys.

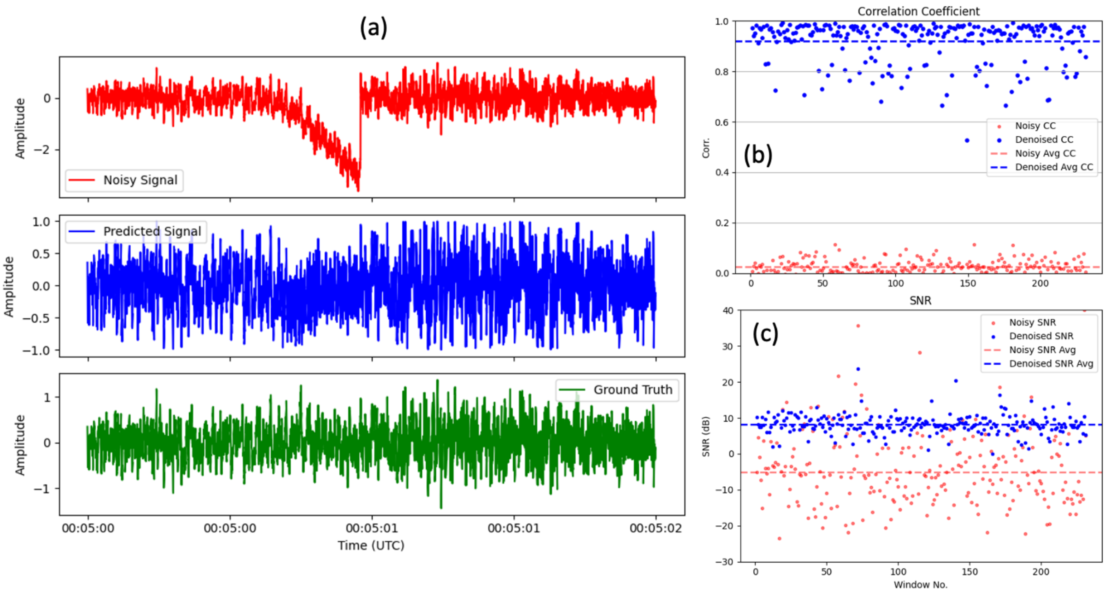

Figure 3.10. Prediction test results for triangle noise removal showing (a) the comparisons between noisy and predicted signals, (b) the correlation coefficient, and (c) the SNR between noisy and denoised signals.

3.3.5 Power Line Noise Reduction

The presence of power lines can disturb the MT signal, manifesting as a sinusoidal interference with a frequency that matches the base frequency of the power line, which is typically 50 Hz in Indonesia. This interference includes up to 10 higher harmonics, each with a smaller amplitude than the main frequency. Unlike other types of noise, harmonic noise is persistent throughout the recording. I need to build a network that can effectively separate this sinusoidal noise from the useful signal because removing the noise directly from the time series will be difficult. As a result, a different neural network model must be developed to remove this type of interference effectively.

In this instance, I employed the RNN-LSTM algorithm to differentiate the harmonic signal from the MT recordings. The network's input layer was fed noisy data, while the output label contained the harmonic noise. As a result, the network's objective was to predict or extract the harmonic noise from the given time series segment. The predicted harmonic noise was subtracted from the noisy signal to obtain denoised data. To achieve this, I first normalized the data using the maximum absolute scaler, which is included in the SciPy module in Python language. Next, the data passed through three LSTM layers, each comprising 64 units with sigmoid recurrent activation. Finally, I introduced a tanh-activated fully connected layer attached to the output layer. The model was trained by minimizing the mean absolute error with the Adam optimizer, where I set the learning rate to be exponentially decreased from the initial rate of 0.01. Training occurred over 100 epochs, with a training time of 7.5 seconds per step. The training and validation loss is shown in Figure 3.7d.

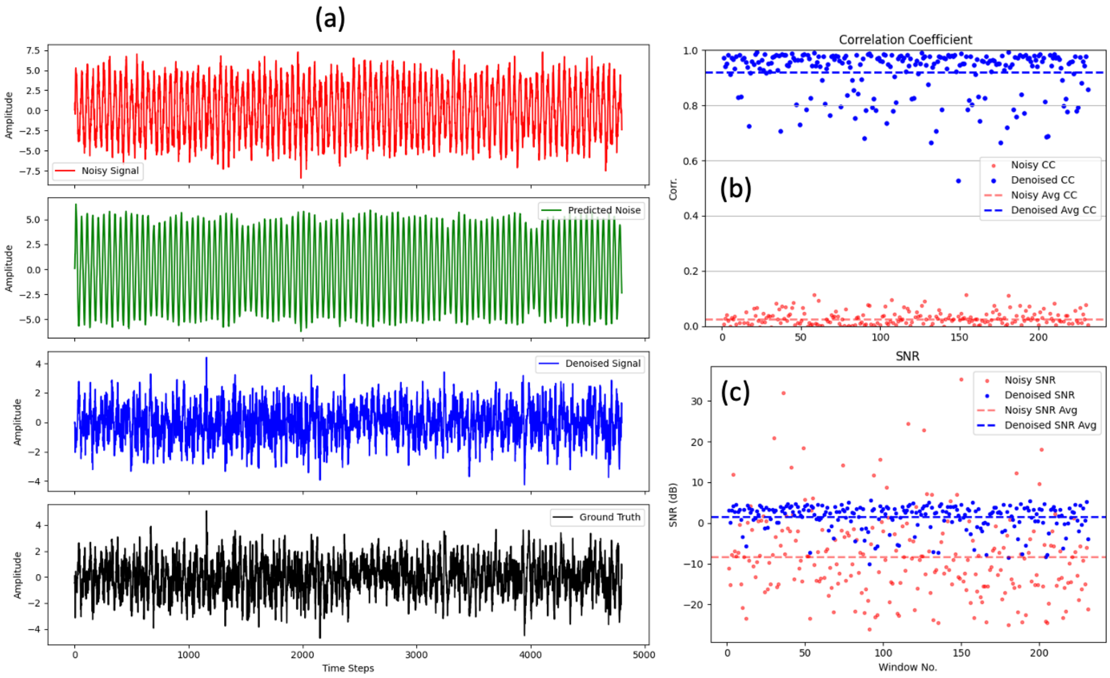

Figure 3.11. Prediction test results for harmonic noise removal showing (a) the comparisons between noisy and predicted signals, (b) the correlation coefficient, and (c) the SNR between noisy and denoised signals.

In Figure 3.11, I can see the prediction test results for the harmonic noise remover module. The left side of the figure shows the harmonic noise predicted by the LSTM network. The figure also demonstrates how the difference between the noisy and predicted noise produces the denoised signal. Comparing the resulting denoised signal with the ground truth from the noise-free signal, I can conclude that the harmonic noise removal was successful, as both signals show a high degree of similarity. This result is also supported by the improved correlation coefficient value, which changed from near 0 to about 0.9. Additionally, the average signal-to-noise ratio of the noise signal demonstrates that the training process effectively removed the noise from the noise. After completing these training and test processes, I must reevaluate the performance of the modular neural network denoiser by applying it to new synthetic data and real field data.

3.4 Application of Modular Denoiser

3.4.1 Synthetic Data

I applied the modular noise removal system to new, unseen, noisy data sets to evaluate its efficacy. Synthetic time series data was synthesized from the 3-D model detailed in subsection 1.2.1. The clean time series data was then artificially contaminated with impulse and charge-discharge noises in every channel, which resulted in a significant reduction in data coherences and a loss of trend in the MT curve. This initial condition is depicted in Figure 3.12a. I subsequently used the trained impulse noise and triangle noise removal modules to reconstruct the clean time series data and calculate the transfer function to see the MT curve after denoising.

Using the modular denoising model, starting the noise removal process with the most significant noise (i.e., the one with the highest amplitude or the most occurences) that could be observed is advisable. After several denoising attempts using various data and noise levels, I noticed that the order of the processes considerably impacts the denoising performance. In this case, the first step involves removing the spikes from the noisy data, as shown in Figure 3.12b. In the upper part of this figure, I can observe that the spikes were significantly removed, leaving a trace of a triangle signal in the early part of the time window. The coherence value of both *ExHy* and *EyHx* data pairs also increased significantly, indicating that the data became more related after the spikes were removed. From the apparent resistivity and phase curves, it is evident that the high-frequency signal was successfully reconstructed, while the low-frequency signal is still under the influence of low-frequency noise, which may be associated with triangle charge-discharge noises. In the next step, I attempted to remove the remaining noise.

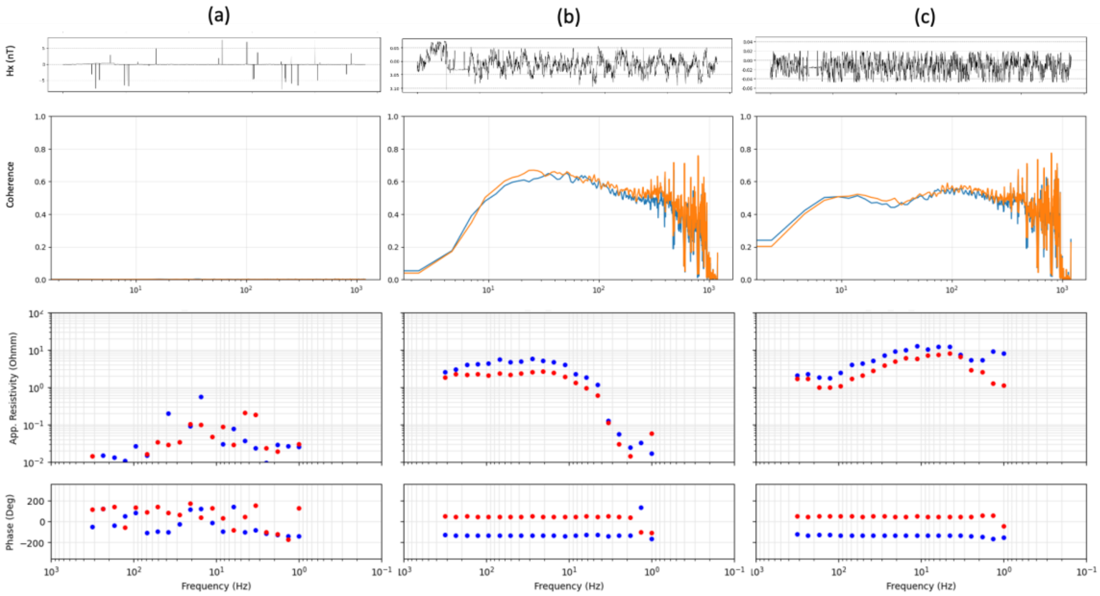

Figure 3.12. Comparison of time series, coherence, and MT curves from (a) initial noisy condition, (b) after spikes removal, and (c) after triangle noise removal.

Figure 3.12c shows the outcome of the noise removal process after eliminating the triangle signal from the noisy time series. The upper section of Figure 3.12c depicts removing the charge-discharge shape, which contaminated the data, resulting in relatively clean time series data. The middle section of the figure indicates that the coherence has not significantly improved following the previous denoising attempt. The coherence value remains lower than the original value, which may be attributed to the presence of residual noises that the denoising process could not remove. The bottom section of the figure reveals that the MT curves were successfully reconstructed, with a smooth trend evident in both the apparent resistivity curves and the phase curve. Some deviations in the results persist, which may also be due to the residuals of the noise. Nevertheless, the performance of the trained denoising modules was adequately reliable, and the time series data was reconstructed well, ultimately producing a good MT transfer function.

I further evaluated the effectiveness of this approach by testing it on a fresh dataset that had been artificially contaminated with various types of noise, including spikes, steps, triangles, and harmonic noises. I then applied all my trained noise removal models to the data, consecutively in that order, to smooth out the MT curve. As shown in Figure 3.13a, the raw, noisy data was significantly impacted by noise, causing the curve to lose its trend and making it difficult to correct manually or use for the inversion process. Before implementing my modular denoiser method, I attempted to address this issue using the robust processing method known as BIRRP (Chave and Thomson, 2004), which calculated the transfer function while disregarding the outlying noise.

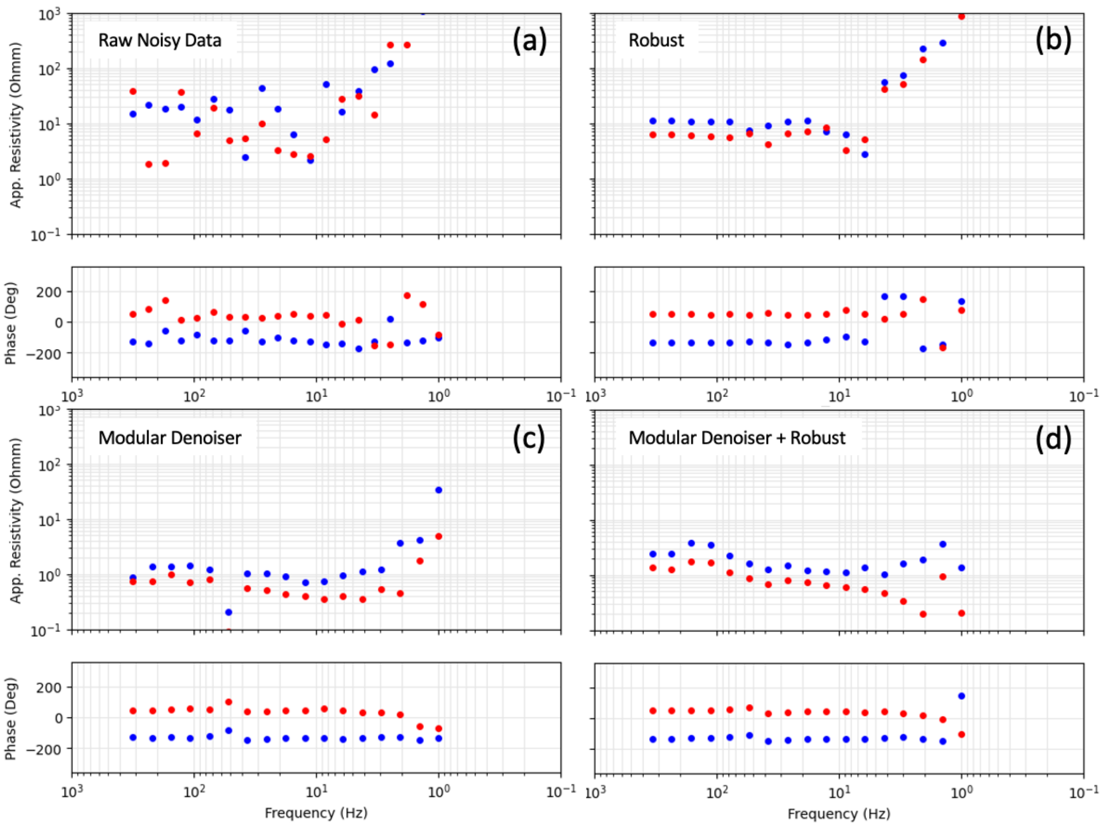

Figure 3.13. Comparison between MT response curves estimated from (a) raw noisy data, (b) BIRRP code, (c) the modular denoiser, and (d) a combination of both methods.

From robust processing, I observed that the transfer function estimation effectively eliminates noise in the higher frequency range but struggles in lower frequencies, as shown in Figure 3.13b. On the other hand, my developed modular denoiser produced a smooth response curve in most of the higher frequency range, although some discrepancies remained in the lower frequencies (see Figure 3.13c). To test the complementarity of these methods, I combined them, and the resulting Figure 3.13d showed a reconstructed response curve for both the apparent resistivity and phase. That suggests that utilizing my modular denoiser with the existing robust processing method can effectively process highly noisy data.

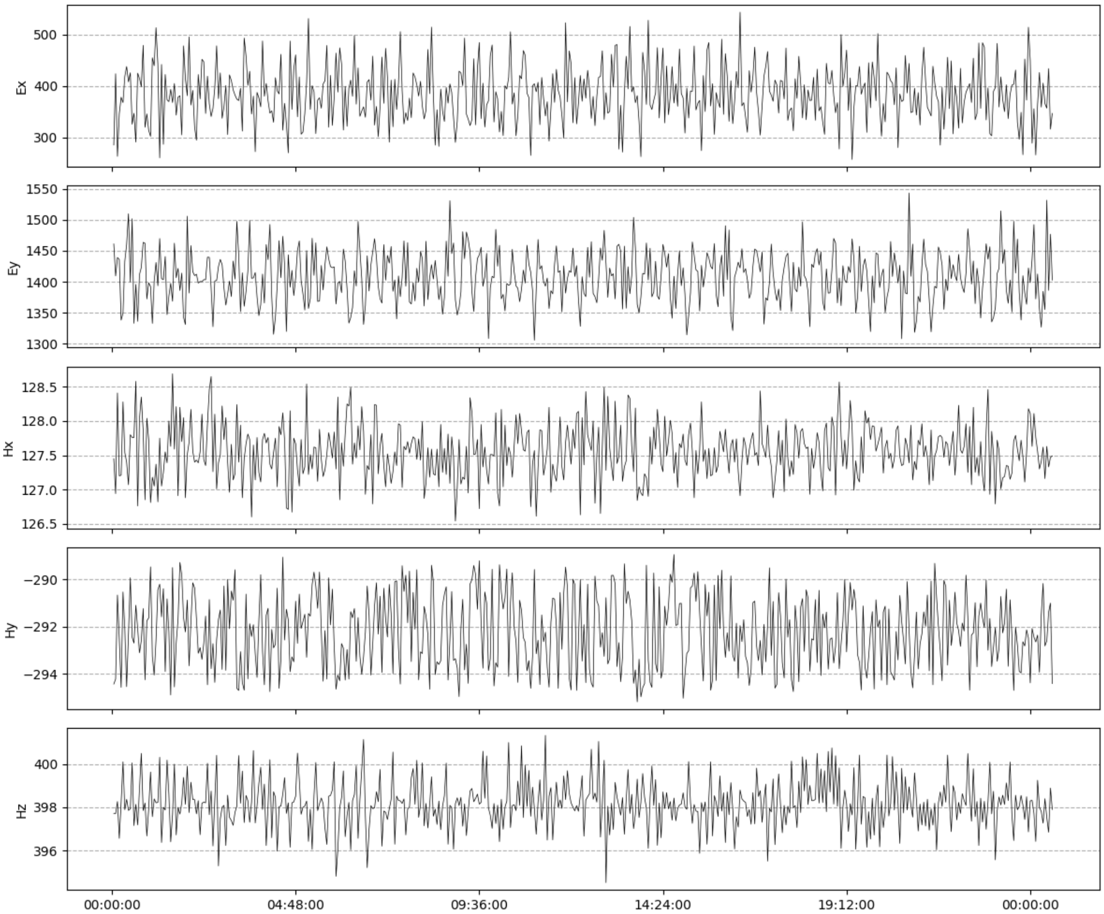

Figure 3.14 Noisy time series segment recorded in Ebino, Kyushu Island, Japan.

3.4.2 Real Data

I utilized my neural network noise removal scheme to eliminate high noise contamination levels during my field survey in Ebino, Kyushu region, Japan (Figure 3.14). This survey uses a newly developed lightweight MI sensor to record the magnetic field variation (Mizunaga et al., 2022; Tanaka et al., 2022). In order to determine the appropriate denoiser module to use, I first needed to identify the types of noises present within the time series data. Upon initial inspection, it was evident that harmonic noises and spikes in the data significantly distorted the data. I conducted a spectrum analysis to understand the frequency of the harmonic noises better. The power spectrum density revealed that the signal had the highest amplitude on several frequencies, which I identified as corresponding to a 60 Hz power lines signal (Figure 3.15a). Due to the high level of noise interference, the data coherence was quite low, indicating that the signals in each channel were not correlated, as illustrated in Figure 3.15c.

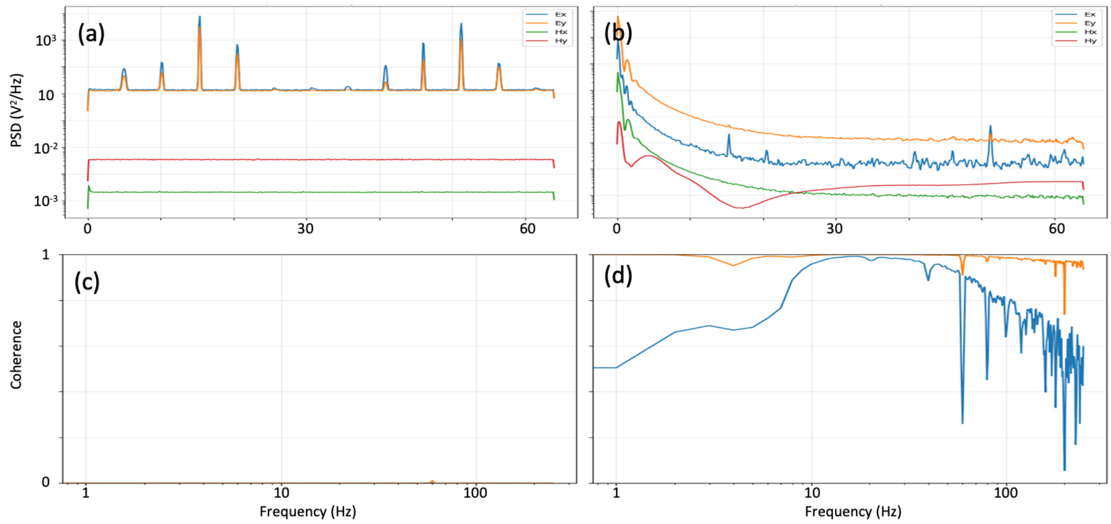

Figure 3.15 Power spectrum density of the MT signal (a) before and (b) after the denoising process, and the signal coherence (c) before and (d) after noise removal.

The impulse noise and harmonic noise removal modules were employed to process the time series data. The primary objective was to eliminate the corresponding noises, enhance the data quality, and minimize the subsequent impact of the noises on the resulting MT curves. The denoising process was carried out instantaneously, as the program merely needed to utilize the trained model to remove the learned noise patterns. After removing the noises from the time series, the power spectrum density was recalculated using the noise-free signal. The study results indicate a reduction in the signal at 60 Hertz and its lower and higher harmonics, as displayed in Figure 3.15b. Furthermore, the coherence of the signal was improved, as demonstrated in Figure 3.15d.

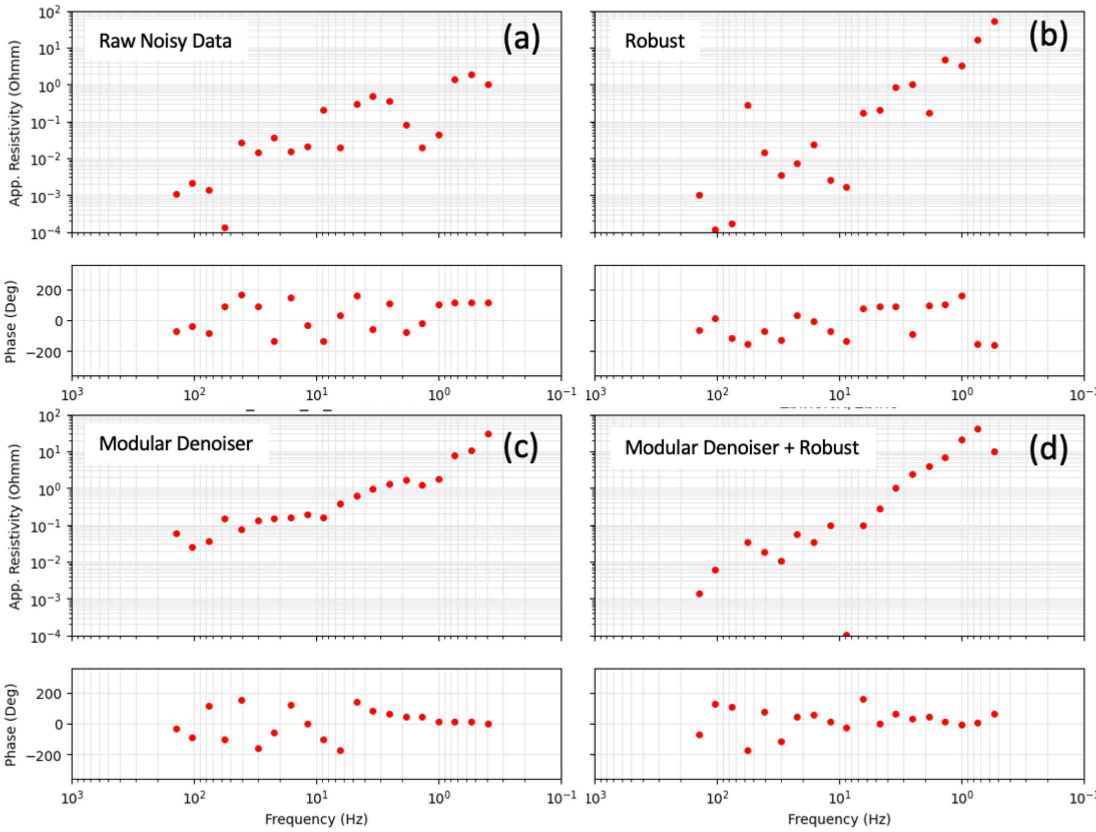

Figure 3.16. Comparison between real field MT response curves estimated from (a) raw noisy data, (b) BIRRP code, (c) the modular denoiser, and (d) a combination of both methods.

Figures 3.16a and 3.16b depict the MT response curves resulting from applying the least square method and BIRRP code, respectively, for processing noisy data. However, both methods failed to estimate the response function accurately, as evidenced by the unsatisfactory curve trend. To further evaluate the effectiveness of this denoising method in improving data quality, I estimated the MT response based on the denoised data. The results of the least square approximation for the MT response function for the denoised data are presented in Figure 3.16c. While the smoother curves obtained from this method appear promising, the trend in Figure 3.16c is not particularly reasonable. Additionally, combining my neural network, the denoising method, and the robust algorithm yielded less-than-ideal results (see Figure 3.16d). The apparent resistivity and phase curves indicate that the frequency distributions were successfully reconstructed and smoothed out, but the validity of these results remains questionable due to the lack of comparative data.

3.5 Concluding Remarks

Removing the noise signals from MT time series data can significantly enhance accurate exploration. It can improve data quality and minimize the risk of incorrect processing or misinterpretation. This research showcases the application of 1-D convolutional neural networks and long short-term memory algorithms to eliminate the typical noises affecting MT time series data. The deep learning algorithm's well-established pattern recognition capabilities were utilized to accomplish this feat. I expected that the trained neural network models would be proficient in distinguishing the noise patterns from the contaminated time series data and effectively reduce them.

Based on the neural network training and test results, it was found that utilizing synthetic time series data and simulated noises was highly effective for training the supervised learning algorithms. The resulting modular noise removal models improved the quality of unseen, noisy synthetic signals and real data with high levels of noise contamination. This conclusion was reached by evaluating time series coherences and estimated response functions. However, there is room for improvement in the current method. It was discovered that not all time segments have the same noise level, so it would be helpful to develop a system that can automatically identify which segments need fixing. Another idea to enhance the benefit of this method is to build a noise removal system that can learn patterns from all measurement channels simultaneously rather than fixing each component one by one. In conclusion, deep learning algorithms show great promise for removing or reducing noise in magnetotelluric time series data. Further research in this field would be invaluable for the future of MT exploration.

CHAPTER 4
THREE-DIMENSIONAL IMPEDANCE AND TIPPER INVERSION IN DANAU RANAU, SOUTH SUMATERA

4.1 Introduction

Subsurface resistivity information is essential in geothermal exploration as it is highly related to hydrothermal activities such as alteration, permeability, and heat distribution (Muñoz, 2014). The resistivity distribution map can further be used to image the geothermal system by locating the position of the cap rock, reservoir, and heat source. The cap rock in a geothermal system contributes to a low resistivity anomaly due to hydrothermally altered minerals (Moeck, 2014). A higher resistivity characterizes the reservoir system in the deeper zone, as low-conductivity alteration minerals are abundant in this zone following extensive high-temperature alteration processes (Ussher et al., 2000). The resistivity map could finally suggest the position for production and injection wells, which is decisive in geothermal energy utilization.

The magnetotelluric (MT) method is commonly employed to characterize the electrical resistivity distribution in a geothermal area up to several kilometers under the ground surface. The technique has an excellent response to covering shallow conductive features and deep resistive zones (Abdelzaher et al., 2012; Ardid et al., 2021; Carrier et al., 2019; Kanda et al., 2013; Yadav et al., 2020). It can also infer the subsurface fault and fracture systems that lead to the hydrothermal processes (Becken and Ritter, 2012; Martí et al., 2020; Triahadini et al., 2019; Yamaguchi et al., 2010). Moreover, the MT method has been successfully applied to image several types of geothermal systems in different regions worldwide (Cherkose and Saibi, 2021; Matsushima et al., 2020; Nimalsiri et al., 2015; Saibi et al., 2021; Uwiduhaye et al., 2021) including low to high-enthalpy geothermal fields (Muñoz, 2014).

This research uses the abovementioned method to reveal subsurface resistivity distribution in the Danau Ranau geothermal prospect. The subject area preserves an intermediate enthalpy geothermal energy (Kusuma et al., 2005), which has not been explored further and does not have a piece of borehole information. Only a limited number of studies about geothermal exploration in this area are publicly available. The most recent publication addressing the issue is a numerical simulation conducted by Afiat et al. (2021). They modeled the geothermal system beneath Mount Seminung using parameters derived from the early geoscience survey, including the subsurface resistivity resulting from a 2-D magnetotelluric inversion modeling (Sugianto et al., 2009). However, the 2-D model is unreliable when imaging complex geological conditions (Ledo, 2005). To overcome such an issue, three-dimensional MT inversion modeling is now becoming a viable option thanks to the advancement in computer performance and the rapid development of 3-D MT inversion algorithms. Instead of using only the principal impedance, as performed in the earlier 2-D model, the diagonal component of the impedance tensor is also used to compensate for the effect of any off-strike geological features.

Being exposed to extensive tectonic and volcanic activities (Natawidjaja, 2018), this area is also expected to have lateral inhomogeneities or spatial variations of rocks' geological and physical properties in the horizontal direction (Båth, 1965). To resolve this matter, the 3-D inversion scheme will also incorporate the magnetovariational data with a higher sensitivity to horizontal resistivity contrasts (Berdichevsky et al., 2009; Zhdanov, 2018). Regarding this matter, there are some studies about both the advantages and drawbacks of including the magnetovariational data or vertical magnetic transfer function as the basis for the inversion process (Berdichevsky et al., 2010; Borzotta, 2012; Dehkordi and Montahaei, 2016; Xu et al., 2013; Zhdanov et al., 2010). Robertson et al. (2020) compared the results of different inverted components (off-diagonal impedance, full-impedance, tipper, and combining all the details). They found that inverting only the data subsets resulted in the inability of the model to explain the other elements that were not included in the inversion. Their study suggests using full-impedance and tipper components for better coverage of subsurface features. The specific objective of this study was to delineate the resistivity map under the Danau Ranau geothermal field using a model-space 3-D inversion scheme based on all components of magnetotelluric transfer functions. Integrated impedance tensor and VTF data inversion could benefit geothermal exploration in geologically complex locations. Hopefully, this study could provide helpful insight into further geothermal exploration work in this prospective area.

The chapter begins with an overview of the geological condition of the study area, including the surface manifestations found inside, and lists results from the preliminary survey. The second part explains the principles of the MT and MV methods, data processing and analysis, and their usage in the inversion process. The result is presented in the subsequent section, with the interpretation and a brief discussion. The overall conclusion of this research is summarized in the last section.

4.2 Danau Ranau Geothermal Field

The presence of geothermal prospects in the Danau Ranau area could be related to the main subduction zone in the west, at the boundary between the Eurasian and Australian plates. Periodic subduction activity in this region stimulates magmatic activity, forming volcanic mountain ranges along the Sumatera Fault Zone that leads to the formation of geothermal systems (Natawidjaja, 2018). The prospect area is situated in the southern part of Sumatera Island, between South Sumatera and Lampung Provinces. Lake Ranau is a Pleistocene caldera from the Mount Ranau eruption, forming the circular scarf and tectonic depressions (Kusuma et al., 2005). A stratovolcano, Mount Seminung, began afterward, standing in the middle of the current study area. The geothermal field covers a 127 km^2 area, as shown in Figure 4.1. No borehole data is available. Therefore, thorough subsurface modeling is highly needed for further exploration and accelerating energy utilization.

The morphology of the Danau Ranau geothermal prospect area consists of plains, hills, and mountains with different geological characteristics. They could be divided into three morphological units: (1) old volcanic unit, (2) young volcanic unit, and (3) alluvial plain. Geological structures controlling the permeability in the area are the dextral strike-slip faults in the NW-SE direction and several normal faults in the NW-SE and N-S directions. Volcanic products of Mount Seminung dominate the lithology in the area, as shown in Figure 4.2. The basement rock is a tertiary-aged Hulu Simpang Formation consisting of lava, volcanic breccia, tuff, shale, and sandstone. The oldest rock in the survey area is the old volcanic lava, which has a porphyritic texture and is made of hornblende, pyroxene, and plagioclase minerals formed in the early Miocene age. The youngest unit is found around the tip of Mount Seminung, which is the mountain's last andesitic lava flow product, formed in the quaternary period (Kusuma et al., 2005).

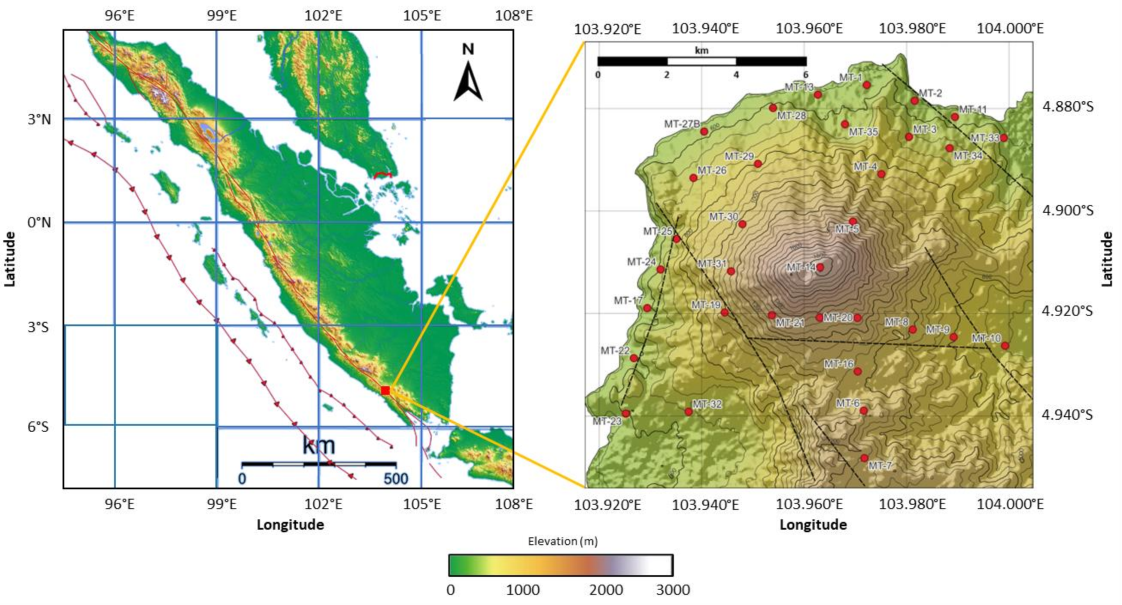

Figure 4.1. The location of the study area on the map of Sumatra Island. Red lines indicate the main tectonic systems (adapted from Natawidjaja, 2018)

Eight groups of warm and hot water springs are inside the Danau Ranau geothermal prospect area. Most appear on the surface in the northern and western vicinity of Mount Seminung, next to the lip of the lake, as plotted in Figure 4.2. The hot springs discharge follows the direction of the known fault systems. The hot springs have a neutral pH and varying temperatures ranging from 37°C to 63°C and are discharged at speeds up to 0.5 L/s (Kusuma et al., 2005). The initial geochemical survey by Kusuma et al. (2005) implies that the geothermal system belongs to the intermediate enthalpy as it shows that the reservoir temperature is about 158-199°C based on the SiO_2 geothermometer. Two alteration zones are found on the surface, next to the groups of hot springs mentioned earlier. These findings show the footprints of hydrothermal activities on the surface in the form of argillic alteration minerals. There are high Hg and CO_2 anomalies near those locations, indicating the existence of permeable zones in the study area. Travertine deposits were also discovered in the northeastern part, followed by a high value of HCO_3 resulting from a mixture of hydrothermal minerals with surface water (Afiat et al., 2021; Kusuma et al., 2005).

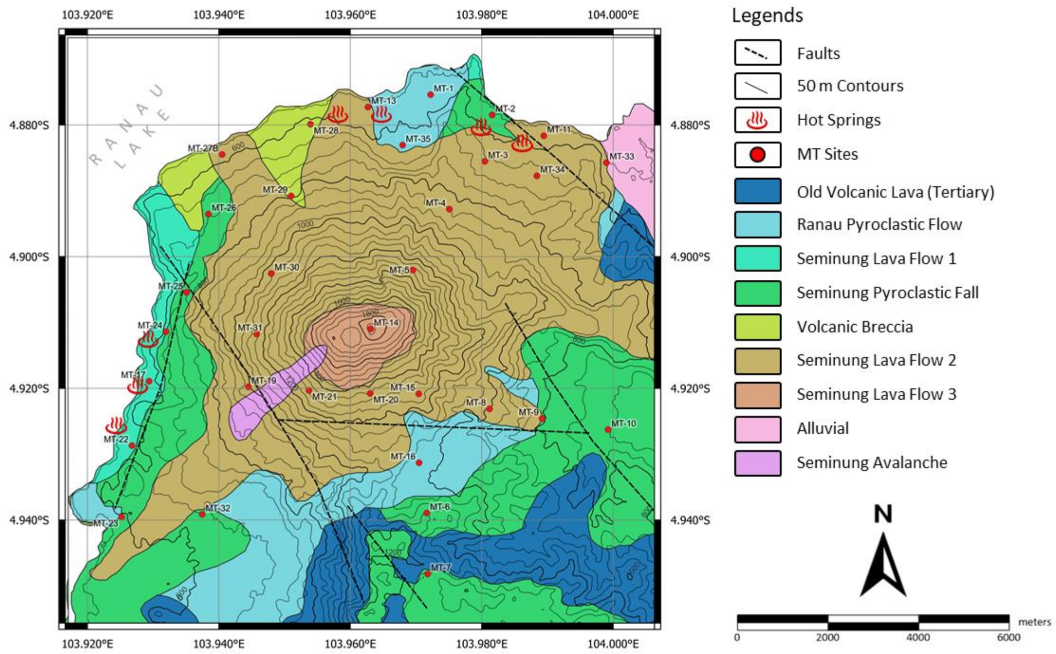

Figure 4.2. Locations of MT stations on the regional geology map of the Danau Ranau geothermal prospect area (modified from Kusuma et al., 2005).

4.3 Magnetotelluric Data and Methods

The data used in this study is the magnetotelluric data acquired in 34 stations for 13 hours on average. The distribution of MT stations covers almost all the areas of interest surrounding Mt. Seminung, including the location of surface manifestations, with a station interval of about 1 km. The acquisition resulted in the time-varying field amplitude of five electromagnetic components, which included two horizontal electric fields in the N-S and E-W directions, two horizontal magnetic fields in the same directions, and one vertical part of the magnetic field. The MT response functions (impedance tensor and vertical magnetic transfer function) were then estimated in the frequency domain ranging from 0.003 Hz to 320 Hz. (Sugianto et al., 2009).

4.3.1 Impedance Tensor

The magnetotelluric method utilizes naturally alternating electromagnetic fields to map the subsurface resistivity distribution up to several kilometers of depth. It measures temporal and spatial variations of electric and magnetic fields on the Earth's surface over a wide frequency range (Cagniard, 1953; Tikhonov, 1950). The observed horizontal electric and magnetic fields are correlated through the impedance tensor **Z**, which can be written as follows:

$$\boldsymbol{Z} = \frac{\boldsymbol{E}}{\boldsymbol{H}} \ , \tag{4.1}$$

where $\boldsymbol{E}$ and $\boldsymbol{H}$ denote electric field in V/m and magnetic field intensity in A/m, respectively. The surface impedance is a 2 × 2 sized complex-valued tensor quantity, where

$$\boldsymbol{Z} = \begin{bmatrix} Z_{xx} & Z_{xy} \\ Z_{yx} & Z_{yy} \end{bmatrix}. \tag{4.2}$$

Then, from each component (ij) of the impedance tensor, it is possible to calculate the apparent resistivity (ρ) and impedance phase (ϕ) as follows:

$$\rho_{ij} = \frac{1}{\omega\mu_0} \left|Z_{ijk}\right|^2 \ , \tag{4.3}$$

$$\phi_{ij} = \tan^{-1}\left(\frac{Im(Z_{ij})}{Re(Z_{ij})}\right) , \tag{4.4}$$

where ω is the angular frequency of the electromagnetic signal, and μ_0 represents a value for free-space magnetic permeability (Simpson and Bahr, 2005).

In the 3-D model, $\boldsymbol{Z}$ is non-symmetric as it could have a unique non-zero value for all the components in (4.2). The 2-D MT approach minimizes the diagonal impedance elements (Zxx, Zyy) by rotating the tensor. Then, the inversion is done using only the off-diagonal, also called principal impedance (Z_{xy}, Z_{yx}). By applying a rotation strike angle, the effects of any off-profile structure are neglected (Siripunvaraporn et al., 2005). In early 3-D modeling attempts, the diagonal components of impedance tensor are often ignored in resistivity modeling due to the limitation of the computer's ability or its effect on the resulting inverted curves. The magnitude of the diagonal components is relatively small compared to the off-diagonal ones, with a lower signal-to-noise ratio, which could degrade the inversion process and increase the overall RMS misfit (Newman et al., 2008). However, using the off-diagonal impedance tensor element alone may fail to sense oblique conducting bodies in three-dimensional earth (Kiyan et al., 2014). Moreover, including the diagonal components could provide a more detailed structure and subsurface features (Kiyan et al., 2014; Newman et al., 2015; Robertson et al., 2020; Slezak et al., 2019). This study provides the impedance tensor elements as one of the bases for three-dimensional inversion modeling of MT data in the Danau Ranau geothermal complex.

4.3.2 Tipper Vector

The vertical magnetic field component (Hz) is usually zero except when sensing lateral resistivity variations nearby. That happens after the differences in current density in a conductor-resistor boundary make the magnetic field fluctuate in a vertical direction, which obeys Faraday's law (Thiel, 2008; Vozoff, 1991). The tipper vector is computed from the vertical magnetic transfer function, which is another kind of magnetotelluric field response that expresses the relation between the horizontal and vertical magnetic field as follows:

$$H_z = \begin{bmatrix} T_{zx} & T_{zy} \end{bmatrix} \begin{bmatrix} H_x \\ H_y \end{bmatrix} \ , \tag{4.5}$$

where H_x, H_y, and H_z are magnetic field intensity in x, y, and vertical directions, respectively. T_{zx} and T_{zy} are the two complex-valued components of the tipper vector $\boldsymbol{T}$.

Therefore, VTF is only produced when there are lateral conductivity variations and, therefore, could help to detect the anomalous conducting zone (Berdichevsky et al., 2009).

The tipper quantity has been used to detect the conductivity source and resolve the ambiguity in the strike direction (Ermolin et al., 2014; Shalivahan et al., 2017; Xu et al., 2013). VTF alone could effectively recover the horizontal anomaly position and lateral conductivity contrast, but not the depth and amplitude (Siripunvaraporn and Egbert, 2009). Berdichevsky et al. (2003) concluded in their study that the tipper data is not susceptible to the statics shift effect and, therefore, is beneficial to improving the reliability of the inverted geological model. All the studies reviewed here suggest a pertinent role of the vertical magnetic transfer function in subsurface resistivity imaging in addition to the impedance tensor data. Considering the topography of the Danau Ranau geothermal prospect area, including tipper data in the analysis could also be helpful since the use of magnetic response over conducting terrains is preferable, as the electric data is often distorted (Chave and Jones, 2012).

4.3.3 Dimensionality Analysis

Using the full component of the MT response function in 3-D inversion is computationally expensive and time-consuming. Joint inversion of impedance tensor and tipper vector could provide valuable constraints to recover the subsurface resistivity structure with a high level of complexity (Siripunvaraporn and Egbert, 2009; Tietze and Ritter, 2013). On the other hand, when overused, the additional magnetic transfer function data and non-principal elements of the impedance tensor could lower the inversion model quality (Newman et al., 2008). Therefore, one should include these components before the inversion and interpretation processes. That could be done by analyzing the degree of three-dimensional distortion in the MT data.

Phase tensor is used to analyze the subsurface directionality and dimensionality (Bibby et al., 2005; Booker, 2014; Caldwell et al., 2004). It is commonly displayed as an ellipse with its semi-major axis and semi-minor axes representing the maximum (Φ_{max}) and minimum (Φ_{min}) phase, respectively. Generally, when the underlying structure is symmetric, the ellipse is symmetric, and vice versa. The elongation direction of the ellipses shows the geoelectrical strike. The asymmetrical measure is expressed by another invariant parameter, skew angle (β). For the 2-D situation, $|\beta|$ is zero and gets higher as the earth has a greater dimensionality. Therefore, 3-D inversion should be carried out to model the subsurface precisely (Hill et al., 2009). Phase tensor ellipses and skew angles from all stations in the survey area are shown in Figure 4.3.

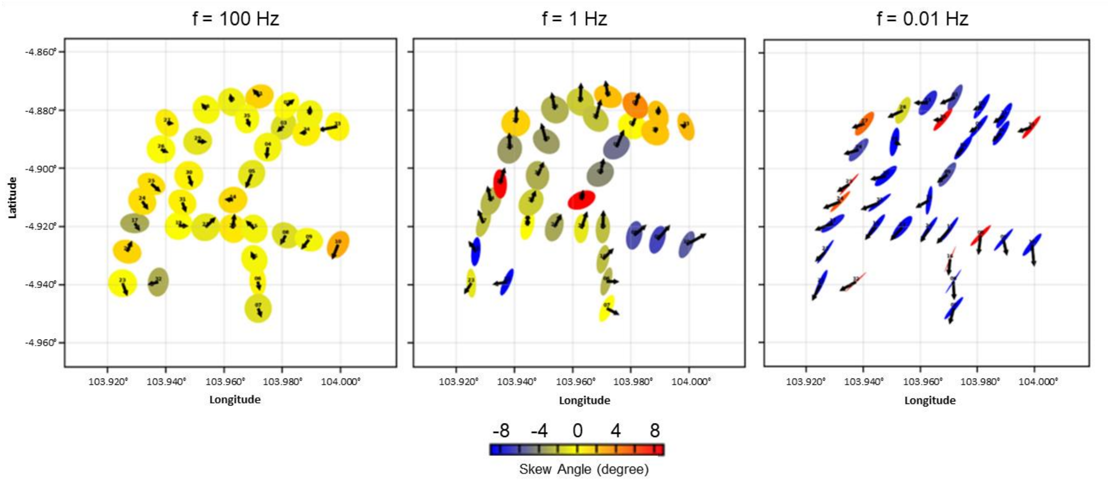

Figure 4.3. Phase tensor maps at each MT station at 100, 1, and 0.01 Hz

The phase tensor is calculated using a Python-based MT toolbox package (Kirkby et al., 2019; Krieger and Peacock, 2014) at three different frequencies (100, 1, and 0.01 Hz) to demonstrate the dimensionality and directionality variation with depth. At 100 Hz, the shape of phase tensor ellipses is mostly circular, with $|\beta|$ being not greater than 3 degrees. It shows a 1-D structure at a shallow depth in each station. At 1 Hz, the shape of the ellipses and skew values vary. The symmetrical shape of the ellipses, followed by a relatively small value of $|\beta|$ are exposed in the northern part of Mt. Seminung, while they are asymmetric in other locations. This lateral difference indicates a spatial complexity of the subsurface in the lateral direction. This condition makes using the vertical magnetic transfer function in the inversion process preferable as it can detect such geological situations. The phase tensor map at 0.01 Hz shows more evidence of the subsurface asymmetricity in a deeper depth. The value of the skew angle is very high, so the phase tensor analysis reveals the three-dimensionality in the deeper depth. Therefore, a 3-D inversion scheme incorporating the complete component of the MT transfer function is needed to get the whole image of the subsurface resistivity distribution under the Danau Ranau geothermal prospect area.

4.3.4 Three-dimensional Inversion

In the subsurface resistivity 3-D modeling, I use all components of complex MT response at 20 logarithmically spaced frequencies ranging from 0.03 to 320 Hz. The number and range of frequency used in the inversion process were chosen after considering the optimum computational time and the depth of interest, respectively. The error floor for the data was set to 5% for the off-diagonal impedance, 7% for the diagonal impedance, and 10% for the vertical magnetic transfer functions. After several trials, those final error floors were chosen to find the best trade-off between data misfit and model roughness. The code for the 3-D inversion was obtained from the ModEM software package (Egbert and Kelbert, 2012; Kelbert et al., 2014), which employs the nonlinear conjugate gradient algorithm to minimize the objective function (U) through data and model parameterization as follows:

$$U(\boldsymbol{m}, \boldsymbol{d}) = U_d + \lambda U_m \ , \tag{4.6}$$

where U_d and U_m are data misfits and model roughness regularization, respectively. A constant λ, represents the regularization or trade-off parameter. The first term on the right-hand side of Equation (4.6) is calculated using the observed data vector ($\boldsymbol{d}$) and forward model response ($F(\boldsymbol{m})$), which is given by:

$$U_d = \left(\boldsymbol{d} - F(\boldsymbol{m})\right)^T \boldsymbol{C_D}^{-1}\left(\boldsymbol{d} - F(\boldsymbol{m})\right) \ , \tag{4.7}$$

which also includes a data covariance ($\boldsymbol{C_D}$). The model roughness regularization in the second term is calculated as follows:

$$U_m = (\boldsymbol{m} - \boldsymbol{m_0})^T \boldsymbol{C_M}^{-1}(\boldsymbol{m} - \boldsymbol{m_0}) \ , \tag{4.8}$$

where $\boldsymbol{m}$ and $\boldsymbol{m_0}$ are the updated and the initial model vector, respectively. The model covariance ($\boldsymbol{C_M}$) is used as the smoothing and scaling control for the estimated model.

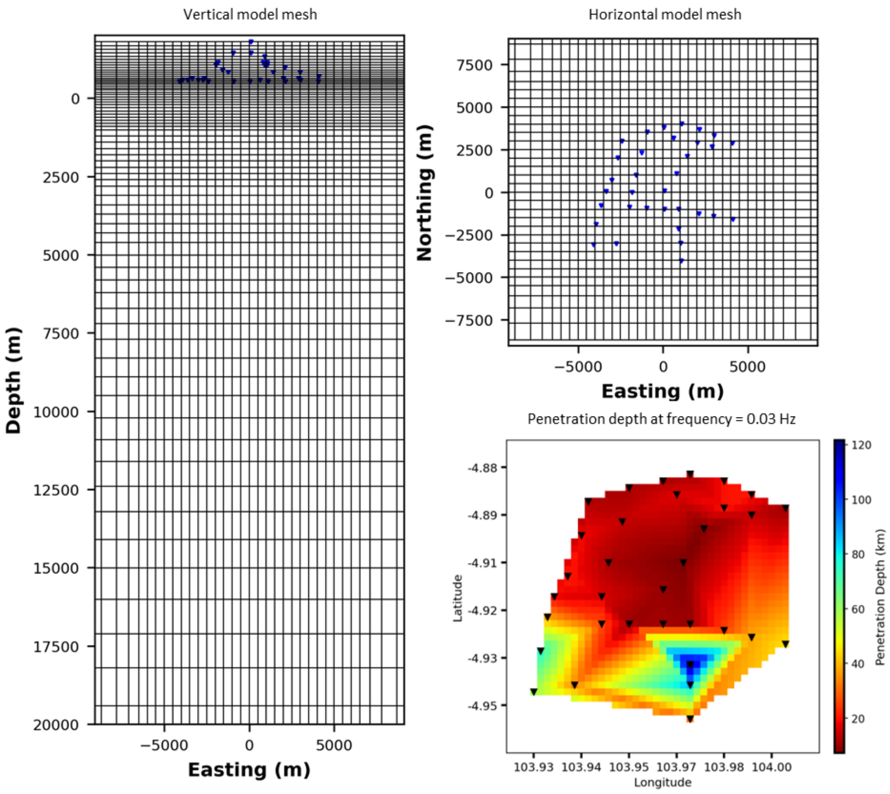

Figure 4.4. Vertical (left) and horizontal (upper right) view of the model grid for 3-D magnetotelluric inversion and signal penetration depth estimation at frequency = 0.03 Hz (lower right). Downward triangles represent MT station locations.

In the model space, a cell dimension of 500 × 500 m was used in both the x and y directions, which covers the main survey area of about 100 km^2. The total size of the mesh grid was 56 (Nx) × 58 (Ny) × 60 (Nz), including five padding cells on each edge to prevent the boundary effect during the inversion process, as shown in Figure 4.4. The model thickness on the first layer was 50 m and increased successively with depth by a factor of 1.12 until it reached 20 km depth. Several inversion tests showed that the calculated curves failed to follow the observed ones at a lower frequency when the model depth was inappropriate. Therefore, the maximum model depth was assigned by first calculating the signal penetration depth using the Niblett-Bostick formula (Bostick, 1997; Rodríguez et al., 2010), as shown on the right-hand side of Figure 4.4. A half-space resistivity of 100 Ωm was used for the starting model. The topography model from NASA (2013) was incorporated into the model mesh. The regularization parameter (λ) was initially set to 10 to stabilize the inversion process and automatically decreased with a ratio of 0.1. After several attempts, these parameters were carefully considered, and each parameter's influence rate was followed, as Robertson et al. (2020) studied. The model, data, and control parameter files were prepared using the MTpy module (Kirkby et al., 2019).

4.4 Resistivity Model and Interpretation

4.4.1 Inversion Result

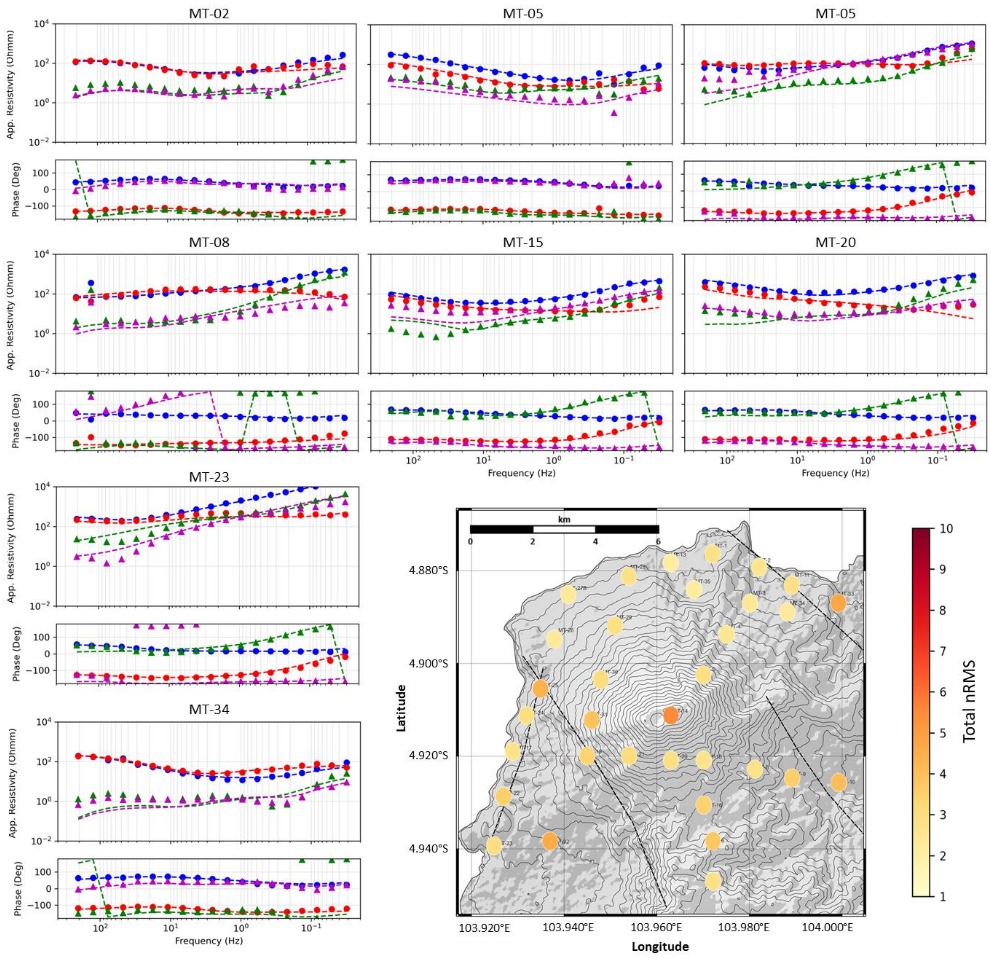

Figure 4.5. Curve fitness between observed (dotted) and calculated (dashed) apparent resistivity and phase in several sample locations for XY (blue circle), YX (red circle), XX (green triangle), and YY (purple triangle) components. The map in the bottom right shows the normalized RMS (nRMS) after the final iteration calculated from all station MT components.

The inversion process stopped after 80 iterations with the normalized root mean squared error of 2.2. The regularization parameter (λ) was updated twice during the inversion process to achieve sufficient gradient descent in the search for the global minimum, with the final value of 0.1. Overall, the inversion convergence process was exhaustive since incorporating the vertical magnetic transfer function makes the calculation heavier. Observed and calculated data for complete impedance components resulting from the inversion are a good fit in most MT stations (see Figure 4.5). As shown at the bottom right of Figure 4.5, the normalized RMS values in all the MT stations are primarily small. Both quantitative and qualitative assessments of the misfits show that the result of 3-D MT inversion is considered acceptable.

4.4.2 Lateral Resistivity Model

The resulting resistivity model is presented in several depth slices, as shown in Figure 4.6. At the shallow depth, resistivity values vary throughout the measurement area, depicting the surface's geological variations due to recent and earlier volcanism. A conductive body is first encountered below the summit of Mt. Seminung, as shallow as 250 m from the surface. This low resistivity anomaly is then spread out to the northern and western portion of the survey area, heading to the location of hot spring manifestations at the deeper depths (see 500 m depth slice in Figure 4.6). In the northern part of the area, low resistivity anomalies come across the location of the strike-slip fault system, which explains the finding of some alteration minerals, including travertine, on the surface in this area. The geothermal fluids alter the minerals, and some follow the outflow permeable path along the fault structure before reaching the surface. In the western part of Mt. Seminung, the normal fault in the NE-SW direction controls the appearance of the hot spring manifestations. From the resistivity distribution map (Figure 4.6) at 750 m and 1,000 m depths, this structure also marked out the conductive cap rock's boundary, indicating that the hot springs appear as outflow manifestations.

The conductive body is no longer detected at a depth of 1,500 m, where a medium resistivity anomaly appears in the subsequent layer. This resistive zone first appears in the center of the study area. This zone is most probably the reservoir zone where geothermal conduction occurs. The medium resistivity anomaly is detected due to the effects of the high rock porosity and permeability, geothermal fluids, and some less conductive mineral products following the alteration processes at high temperatures (Ussher et al., 2000). This zone spreads from the center to the northern and western portions of the geothermal field, following the overlying conductive clay cap. This reservoir zone extends to a depth of about 3,000 m.

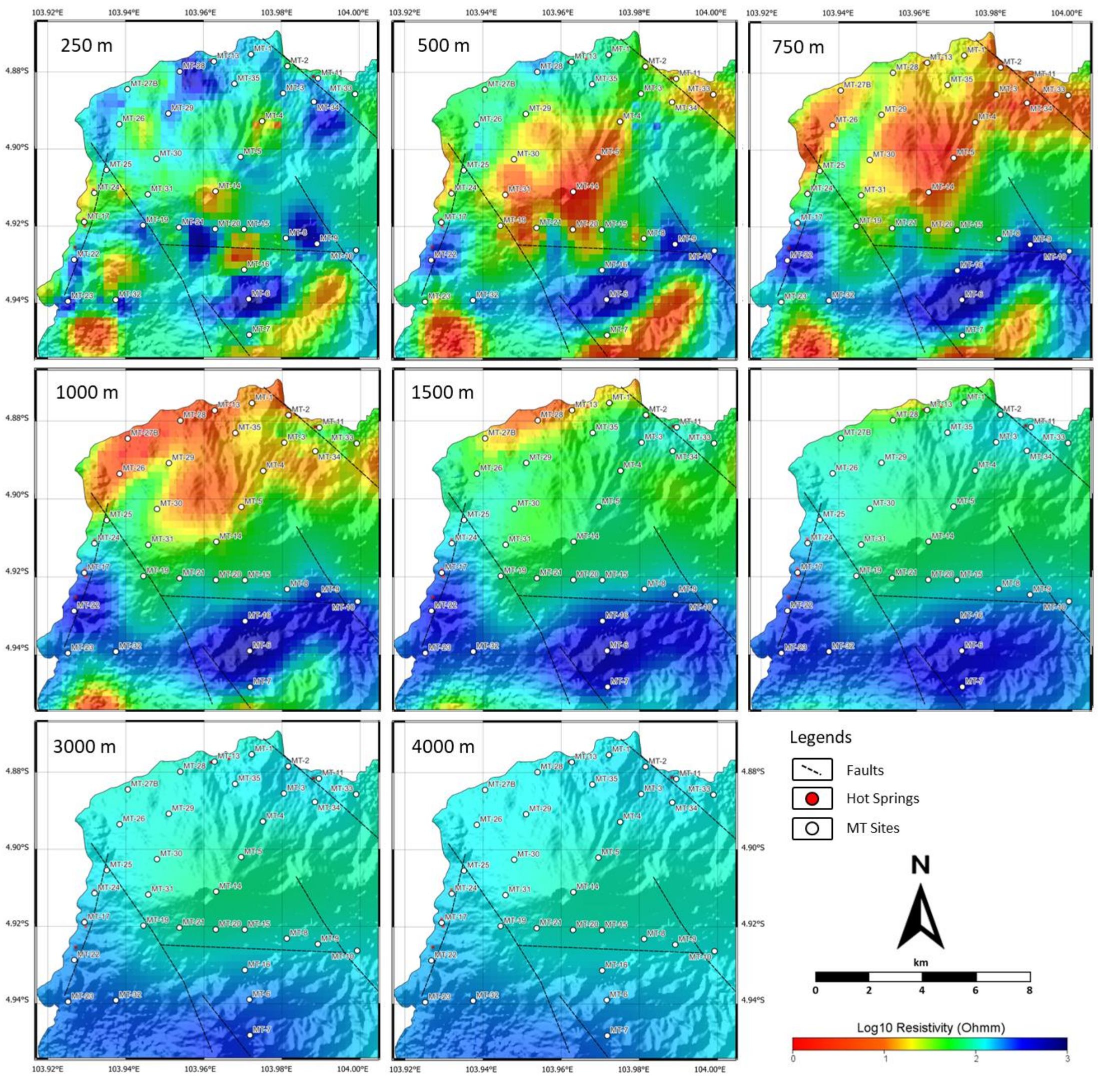

Figure 4.6. Horizontal resistivity distribution map at several depths resulting from the 3-D MT inversion.

While the conductive zone spread across the northern part of the study area, the highly resistive body dominates the southern region. The boundary between the highly resistive and conductive body coincides with the location of an E-W normal fault, which indicates that the electrical difference is associated with lithological contrast. The high resistivity anomaly could be related to the older volcanic bodies that extend to the deeper subsurface. Not so many resistivity variations at a depth deeper than 3,000 m. This finding could depict the depth of basement lava rocks of the Hulu Simpang Formation, the tertiary-aged product from the ancient Mt. Ranau. There is no indication of a geothermal heat source detected in the horizontal resistivity depth map, as no conductive anomaly is found below the reservoir zone. However, the electrical resistivity value in the center of the area is at more than 3,000 m depth, which is lower than the surroundings. It could indicate the heat conduction path between the heat source and the reservoir as the temperature is higher in this zone, which affects the rock's conductivity.

4.4.3 Vertical Resistivity Model

Vertical slices of the subsurface resistivity distribution are presented in the 3-D view of the Danau Ranau geothermal prospect area, as shown in Figure 4.7. The slices were made to understand the connection between the two groups of surface manifestation and the center of the reservoir. From the vertical slices, the impermeable conductive zone is mapped in an up-dome shape, with its base of conductor located below the summit of Mt. Seminung at a depth of about 1,500 m from the surface. The clay cap zone extends up to 5 km to the north and west areas with a thickness of about 1 km.

The vertical sections clearly show how the faults in the survey area control the geothermal systems and fluid flow from the reservoir to discharge points. The geothermal fluids are released at the end of the conductive, impermeable clay cap in the outflow zone. The finding agrees with the preliminary geochemistry survey, which stated the same based on the low value of Na/Ca analysis (Kusuma, 2005). In the northern part, the geothermal fluids follow the impermeable cap rock before finally appearing on the surface through the fault system. This result explains the high concentration of SiO_2 in the water sample (Afiat, 2021), as the water in this manifestation group originated directly from the reservoir. On the other hand, less SiO_2 concentration in the western manifestation group may be due to the presence of NE-SW normal fault structure crossing the conductive zone. This fault system ends the continuation of the conductive body in this direction and allows surface water to impurify the geothermal fluids on its way to the discharging points.

In the middle of the survey area, a medium resistivity zone acted as the geothermal reservoir, found at a depth of 1,500 m, with an area of approximately 16 km^2. This zone borders high resistivity zones in its surroundings, which are most probably associated with the older volcanic bodies with lower porosity than the reservoir rocks. The geothermal reservoir zone extends about 4 km to the bottom of its center. Despite having good imagery of the clay cap and reservoir zone, the 3-D resistivity model could not detect the geothermal system's heat source. As mentioned, the model shows no indication of magma or hot rock intrusions. The depth of the heat source is probably deeply seated and is not reachable by the MT signal, which also explains why the temperature of hot spring water and reservoir is not too high in this geothermal system.

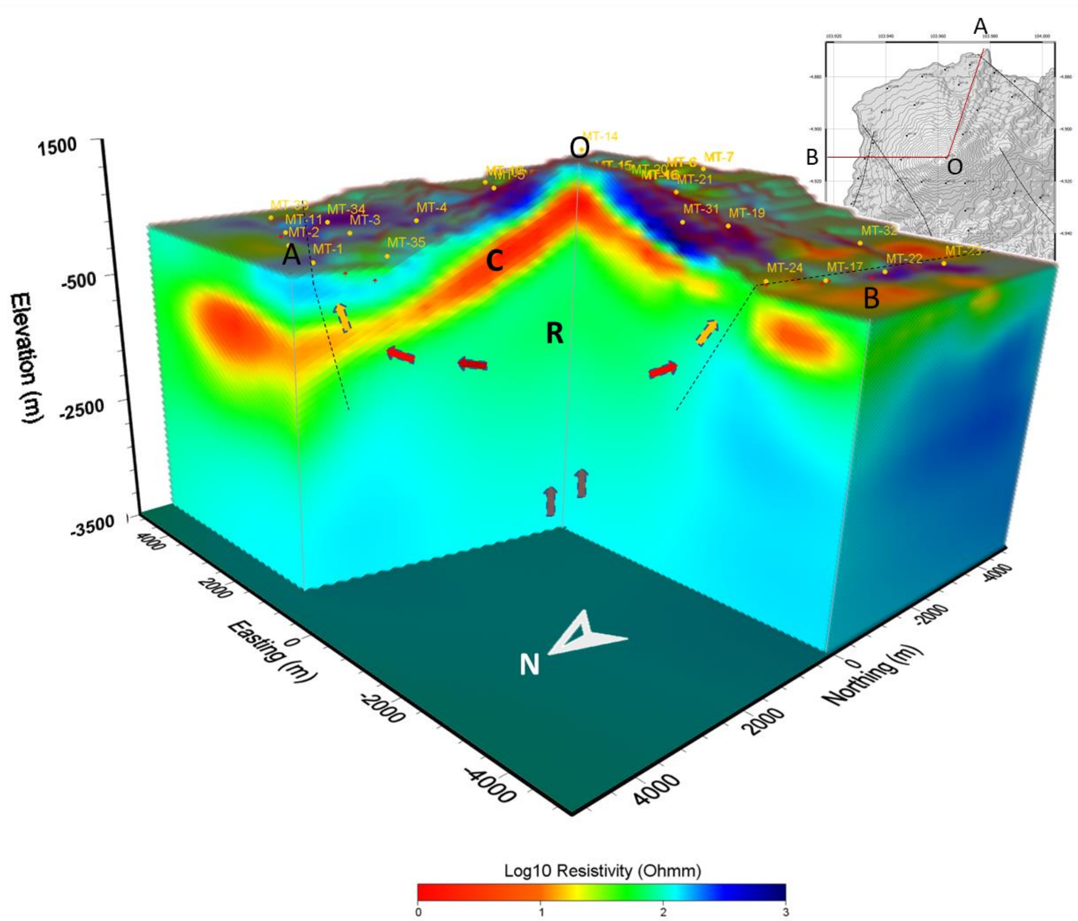

Figure 4.7. Three-dimensional resistivity model. The vertical slices connect both hot spring manifestation groups (A and B) to the summit of Mount Seminung (O). Letters C and R represent clay cap and reservoir zones, respectively. The dashed lines indicate the existing fault systems, while the arrows indicate the direction of fluid flows.

Considering all the results described previously, the geothermal system in the Danau Ranau geothermal area consists of several components. The overburden is found on the surface to a maximum depth of about 500 m. It has varying resistivity values as it comprises the unaltered bodies from several different lithologies on the surface. In the subsequent layer, the impermeable conductive zone has a resistivity value of less than 10 Ωm. Its coverage extends from the center of the survey area to the north and west direction and is bordered by geological structures and manifestations. This clay cap is probably formed from the quaternary-aged lava and tuff from Mt. Seminung, which is altered into argillitic-type minerals due to hydrothermal activity in the geothermal reservoir. The reservoir zone is in the middle of the survey area, first encountered at a depth of 1,500 m from the surface. This porous and permeable rock is most probably associated with the old volcanic lava and pyroclastic from the ancient Mt. Ranau, which have been altered and fractured. The adjacent NW-SE strike-slip fault and the NE-SW normal fault control the fluid migration in the northern and western parts of the area, respectively. The geothermal heat source is undetectable, but it is probably located in the center of the area as the resistivity is slightly lower in that zone. The heat source is expected to be the residual magma, which is also the source of the eruption of Mt. Seminung.

4.5 Concluding Remarks

The Danau Ranau geothermal fields preserve a geothermal potential under the ground as manifested on the surface. A preliminary geophysical, geological, and geophysical data survey was carried out last decade, but no exploitation attempt has been made. This paper presents additional information about the electrical resistivity distribution below the surface based on a 3-D inversion of all components of the magnetotelluric transfer function. The aim is to give new insight as the model includes the constraints from diagonal impedance elements and tipper vectors to compromise the effect of complex geoelectrical conditions.

Dimensionality and directionality analysis using phase tensor ellipses and skew angle revealed that the 3-D inversion was needed to compensate for the high distortion level due to complex dimensionality in the deeper depth. The analysis also showed the spatial (lateral) variation of geoelectrical directionality, suggesting the need to use the vertical magnetic transfer function in the inversion process. The inversion was done after 80 iterations with good fitting between the observed and inverted resistivity curves and a considerably small nRMS error of 2.2.

The 3-D MT inversion result effectively recovers the spread of highly conductive impermeable cap rock in the shallow depth with a maximum thickness of 1,000 m. The inverted model was also able to localize the more resistive zone seated at about 1.5 km depth below the summit of Mt. Seminung, which serves as the reservoir for the geothermal fluids. The total area of the reservoir zone is approximately 16 km^2. Most of the findings follow the preliminary geological and geochemical study, and the geothermal system can be explained clearly. From all the results, it could be concluded that the 3-D integrated inversion of impedance tensor and vertical magnetic transfer function could effectively describe the electrical resistivity distribution in the Danau Ranau geothermal prospect area. In terms of future works, it would also be beneficial to investigate the gravity variations in the geothermal area. The subsurface density distribution and the controlling geological structures delineated from the gravity study could then be integrated into the model resulting from this study. These continued efforts could lead to a more reliable conceptual model of the geothermal system in Danau Ranau prior to its exploitation stage.

CHAPTER 5
THREE-DIMENSIONAL INVERSION OF MAGNETOTELLURIC AND GRAVITY DATA IN MOUNT LAWU GEOTHERMAL PROSPECT

5.1 Introduction

Mount Lawu is a 3,265 m stratovolcano located on the borderline between the Central and East Java Provinces, Indonesia. The mountain has the potential to host geothermal resources due to its location within the Sunda Volcanic Arc and its proximity to other active and potentially active volcanoes (Purnomo and Pichler, 2014). Based on a preliminary geoscience study conducted in 2009, the area hosts a massive geothermal potential of as high as 137 MW (Hermawan and Permana, 2018). The geothermal potential in Mount Lawu is further supported by hot springs and fumaroles on the mountain slopes. At least 11 surface manifestations, including a fumarole, altered minerals, and hot springs, are found. These manifestations indicate the presence of a geothermal system under the ground. A thorough geophysical investigation is needed to understand the subsurface conditions and map the extent of the geothermal system.

Geophysical methods are used to understand the Earth's subsurface condition, including its structure and composition. These exploration techniques involve measuring fields (such as gravity, magnetic, and electromagnetic fields), which are dependent on the physical properties of rocks in the subsurface. The data are then processed and inverted to produce a detailed subsurface map that describes the variation of these physical properties in the lateral and vertical directions. Geothermal exploration uses geophysical methods to identify areas associated with alteration zones and locate the potential geothermal reservoirs. Geophysical inversion can also delineate subsurface structures and fluid flows that help characterize the geothermal system (Ars et al., 2019; Hormozzade Ghalati et al., 2022; Richards et al., 2010). However, each geophysical technique has its limitations. Therefore, combining different methods can provide complementary information and improve the accuracy of the interpretation.

One of the most commonly used geophysical methods for geothermal prospecting is the magnetotelluric (MT) method. The MT method can map the location and geometry of the geothermal system via its resistivity contrast with the host rock (Beka et al., 2016; Hill et al., 2009; Newman et al., 2008). Electrical resistivity is an essential physical property in geothermal exploration since the presence of hot fluids in the subsurface can cause significant changes in the electrical resistivity of the surrounding rocks. Massive ionic conduction in hydrothermal systems increases salinity and the amount of alteration minerals like clays and zeolites, leading to low resistivity anomalies (Gupta and Roy, 2006; Wright et al., 1985). By imaging the electrical properties of the subsurface, the MT method can identify zones of low resistivity, which can indicate geothermal resources. One can also delineate the extent of its overlying impermeable cap rocks by the low resistivity anomaly zone (Matsushima et al., 2020; Ussher et al., 2000). The MT method has been successfully used in geothermal exploration in volcanic areas as several related studies have imaged the low resistivity structures associated with a clay cap, reservoir zones, hydrothermal fluid pathways, and/or partial melting (Başokur et al., 2022; Hacıoğlu et al., 2020; Marwan et al., 2021; Piña-Varas et al., 2014; Zhou et al., 2022). Additionally, MT surveys typically have adequate resolution to image resistivity structures at great depths (up to hundreds of kilometers). This advantage is essential as most geothermal sources are located several kilometers below the surface.

One also needs to identify the geological structures controlling the circulation of geothermal fluids to understand hydrothermal systems. The gravity method could help detect geological structures involving blocks of rocks with different densities (Arisbaya et al., 2023). The gravity method has been proven to identify large-scale geological features related to geothermal systems, such as faults, folds, and intrusions, by detecting the variations in the Earth's gravity field caused by differences in the density and distribution of the subsurface rocks (Kanda et al., 2019; Mulugeta et al., 2021). Gravity anomalies in geothermal fields generally infer the lateral density variations associated with the geometry of fault structures, metamorphism from the thermal water, and the presence of the deep-seated magmatic body, which presumably serves as the heat source

(Atef et al., 2016; Nishijima & Naritomi, 2017). Fault zones, for example, can be identified by a gravity anomaly associated with the density difference between the rocks on either side of the fault. Similarly, a rock undergoing metamorphism or densification due to hydrothermal alteration can cause a higher gravity anomaly than unaffected rocks (Gupta and Roy, 2006).

Many studies discuss the integrated use of MT and gravity data (Abdelfettah et al., 2016; Le Pape et al., 2017; Roden et al., 2011), including some research in geothermal fields (Ars et al., 2019; Mitjanas et al., 2021). These studies concluded that gravity and MT surveys could provide complementary information and that combining them resulted in a more comprehensive understanding of the subsurface structure and the distribution of geothermal reservoirs. This study uses MT and satellite gravity data to explore the geothermal potential in Mount Lawu better. Integrating MT data that provides better vertical resolution with satellite gravity data with higher lateral coverage could give us more accurate results (Arisbaya et al., 2023). The geological structures of the Mount Lawu area are determined by using derivative analysis against the residual gravity anomaly and its modeling. At the same time, the distribution of the conductive alteration layer and its subsequent reservoir zone is modeled through a three-dimensional inversion of magnetotelluric data. The geophysical properties derived from both methods will be used to characterize the main features of the Mount Lawu geothermal system and aid in the successful exploration and development of geothermal energy resources in this area.

5.2 Mount Lawu Geothermal Prospect

5.2.1 Geological Setting

The study area is located in a high-elevation zone, ranging from 500 to 3,100 m above sea level. Mount Lawu's geology is dominated by quaternary volcanic products composed of andesite, basaltic andesite, and dacite. The mountain is believed to have formed around 780,000 years ago and has undergone several periods of activity and dormancy since then. The volcanic activity at Mount Lawu has resulted in the formation of several lava domes, craters, and pyroclastic deposits, which cover the mountain's slopes.

The geological structure of Mount Lawu is characterized by several fault systems, including the Lawu Fault and the Cemorolawang Fault, which run along the southern and northern slopes of the mountain, respectively. These faults have formed several grabens and horsts in the area, classic targets for geothermal exploration. The geological map is shown in Figure 5.1. In order of age, the lithological sequence includes Jobolarangan Volcanic Rocks, Lawu Volcanic Rocks, and Candradimuka Lava.

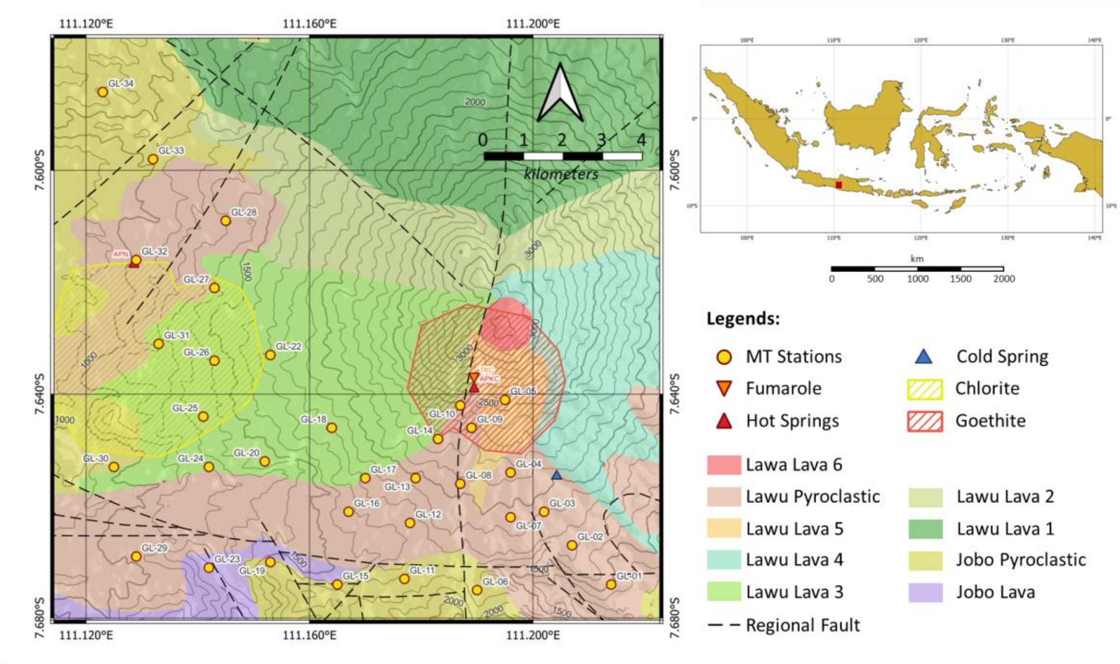

Figure 5.1. The geological map of the study area overlaid with the location of MT stations and hydrothermal manifestations (modified from Sampurno and Samodra, 1997).

Jobolarangan Volcanic Rocks are the oldest lithological group around the Mount Lawu geothermal prospect area, which is the product of Mount Jobolarangan, located in the southern part outside of the study area. The Jobolarangan lava flow is composed mainly of basaltic rock. This rock unit is distributed mainly in the southwestern part of Mount Lawu. The other product is the Jobolarangan pyroclastic rocks, consisting of breccia and tuffs. This volcanic unit was formed after a massive eruption of Mount Jobolarangan in the Pleistocene age. It was scattered in the southern part of Mount Lawu and spread across to the west. The series of volcanic eruptions of Mount Lawu formed the Lawu volcanic complex, which consisted of at least seven stratigraphical units (see Figure 5.1). Each unit was formed one after another and is mainly composed of andesite-basaltic rock containing some minerals such as pyroxene, hornblende, and plagioclase, except the Lawu Pyroclastic flow, which consists mainly of tuffs and volcanic breccias. Between the formation of the first and the second volcanic products of Mount Lawu, the

Candradimuka lava was formed as the product of the lateral eruption of Mount Lawu, which is composed mainly of basalt (Hermawan and Permana, 2018; Sari et al., 2021).

5.2.2 Geochemistry of Geothermal Fluids

Geothermal manifestations appear in cold springs, hot springs, and fumaroles, as shown in Figure 5.1. The fumarolic discharge located just south of Mount Lawu's summit at an elevation of 2,540 m has a temperature of about 93 °C. Hot springs are spread across the area, at elevations varying from 304 m up to 2,540 m. The temperature of the hot spring manifestations ranges from 32.4 to 90 °C. The geothermal fluids in the Gunung Lawu geothermal area contain bicarbonate, sulfate, and chlorite. Isotope analysis of the hot springs water conducted by Bagaskara et al. (2021) indicated that geothermal fluid is a mixture of acidic and meteoric water. The samples with higher temperatures have a high concentration of ^{18}O, which could result from the extensive interactions between hot water and subsurface rocks. The same study concluded that the reservoir system is liquid-dominated, with a temperature between 250 °C and 289 °C, indicating that it is a high enthalpy geothermal system.

5.3 Magnetotelluric Data

The magnetotelluric (MT) method is a valuable geophysical exploration technique that can identify and characterize subsurface geothermal resources. The MT method measures the natural variation of Earth's electromagnetic fields, generated by lightning strikes, and the interaction between the solar wind and the Earth's magnetic field. The MT method is beneficial for geothermal exploration because it can detect resistivity anomalies in the subsurface, indicating the presence of geothermal fluids and associated alteration zones (Maryadi et al., 2022; Nimalsiri et al., 2015; Wang et al., 2023a). The presence of hot geothermal fluids in the subsurface can cause significant changes in the electrical resistivity of the surrounding rocks. By imaging the electrical resistivity of the subsurface, MT inversion can identify zones of low resistivity, which can indicate geothermal resources. Additionally, the MT method can provide information on the depth, lateral extent, and structure of geothermal reservoirs, aiding their development and management.

This study analyzes magnetotelluric data from 33 MT stations, recorded mainly on the southwestern part of Mt. Lawu. The data were acquired using the MTU-5A from Phoenix Geophysics with MTC-50H magnetic sensors from the same manufacturer. The purpose of MT data analysis is to delineate the extent of conductive and resistive bodies underground, which correspond to the existence of the impermeable clay cap, reservoir zone, and geothermal heat source. The placement of the MT stations was made following a preliminary report that indicated that the primary prospective location was in the southwestern part of the field (Hermawan and Permana, 2018). MT data were recorded for 12 hours on average, with the most prolonged usable signal period of 100 s.

5.3.1 Dimensionality Analysis

Three-dimensional inversion of the MT full impedance tensor data is time-consuming and computationally expensive. Therefore, dimensionality analysis is needed to understand the complexity of the subsurface resistivity structure before undergoing the inversion. This study uses phase tensors to analyze the subsurface dimensionality and directionality (Bibby et al., 2005; Booker, 2014; Caldwell et al., 2004). The phase tensor, $\mathbf{\Phi}$, is a complex-valued matrix that characterizes the anisotropic electrical conductivity structure of the Earth at a given location. It is commonly displayed as an ellipse with its semi-major and semi-minor axes representing the maximum (Φ_{max}) and minimum phase (Φ_{min}).

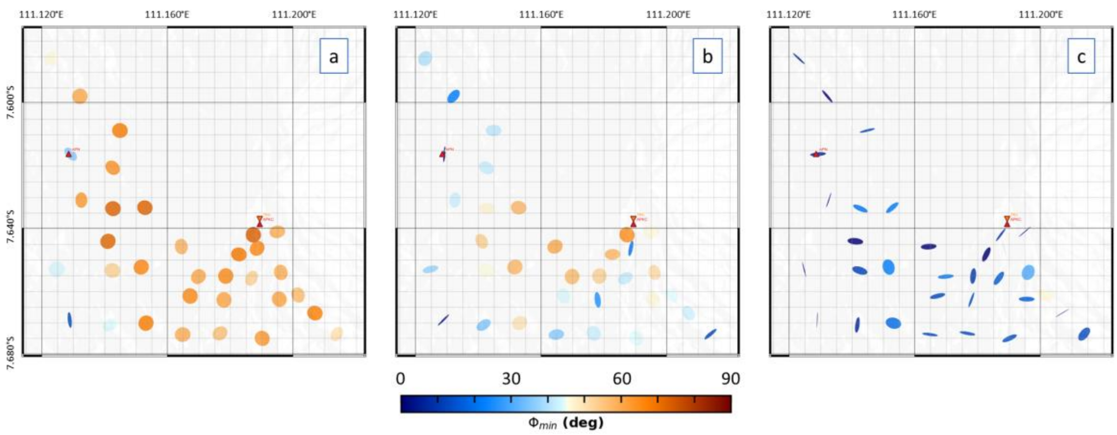

Figure 5.2. Phase tensor maps at several periods: (a) 0.1 s, (b) 1 s, and (c) 10 s.

Figure 5.2 shows the differences in dimensionality of the subsurface features around the survey area. The results indicate that for short periods (less than 1 s), which correspond to a depth of less than 1 km based on the background resistivity, the dimensionality is predominantly 1-D to 2-D. However, the highly varying elongation of the phase tensor ellipses for more extended periods suggests a complex 3-D subsurface structure at deeper depths. The axes of the ellipses in this period range reveal that certain MT stations adjacent to the fumarolic discharge in the southern region exhibit a geoelectrical strike that is almost oriented in a north-south direction. The phase tensor ellipses near the hot spring have a distinct NW-SE orientation at longer periods.

5.3.2 MT 3-D Inversion

The ModEM inversion scheme was used to reconstruct a 3-D model of the subsurface resistivity (Egbert and Kelbert, 2012) from the full impedance tensor. During the inversion process, the penalty function (*U*) was minimized,

$$U(\boldsymbol{m},\boldsymbol{d}) = \left(\boldsymbol{d} - \boldsymbol{f}(\boldsymbol{m})\right)^T \boldsymbol{C_d}^{-1}\left(\boldsymbol{d} - \boldsymbol{f}(\boldsymbol{m})\right) + \alpha(\boldsymbol{m} - \boldsymbol{m_0})^T \boldsymbol{C_m}^{-1}(\boldsymbol{m} - \boldsymbol{m_0}), \quad (5.1)$$

where $\boldsymbol{d}$ is the data matrix, and $\boldsymbol{m}$ denotes the model. The variables $\boldsymbol{C_d}$ and $\boldsymbol{C_m}$ are covariance matrices for both data and model. A regularization parameter (α) is used to stabilize the ill-posed inversion processes (Bell et al., 1978).

The minimum lateral cell size in the model mesh is 500 m × 500 m, except for the padding cells added on all sides (see Figure 5.3a). In the z direction, the model cell thickness increases with depth by 1.3 from 50 m at the surface to the maximum model depth of 12 km. This depth was chosen after calculating the estimated penetration depth using the Bostick transformation formula (Bostick, 1997; Rodríguez et al., 2010), as shown in Figure 5.3b. The total number of model cells is 36×36×51 for easting, northing, and Z orientation, respectively. The topography data from the ETOPO Global Relief Model (NOAA, 2022) was included in the mesh. To include the topography in the model, one must turn off or reduce the smoothing factors between air and land boundaries. The model cells outside the topography are frozen and given a fixed value of 10^{12} Ωm for air resistivity before the inversion process.

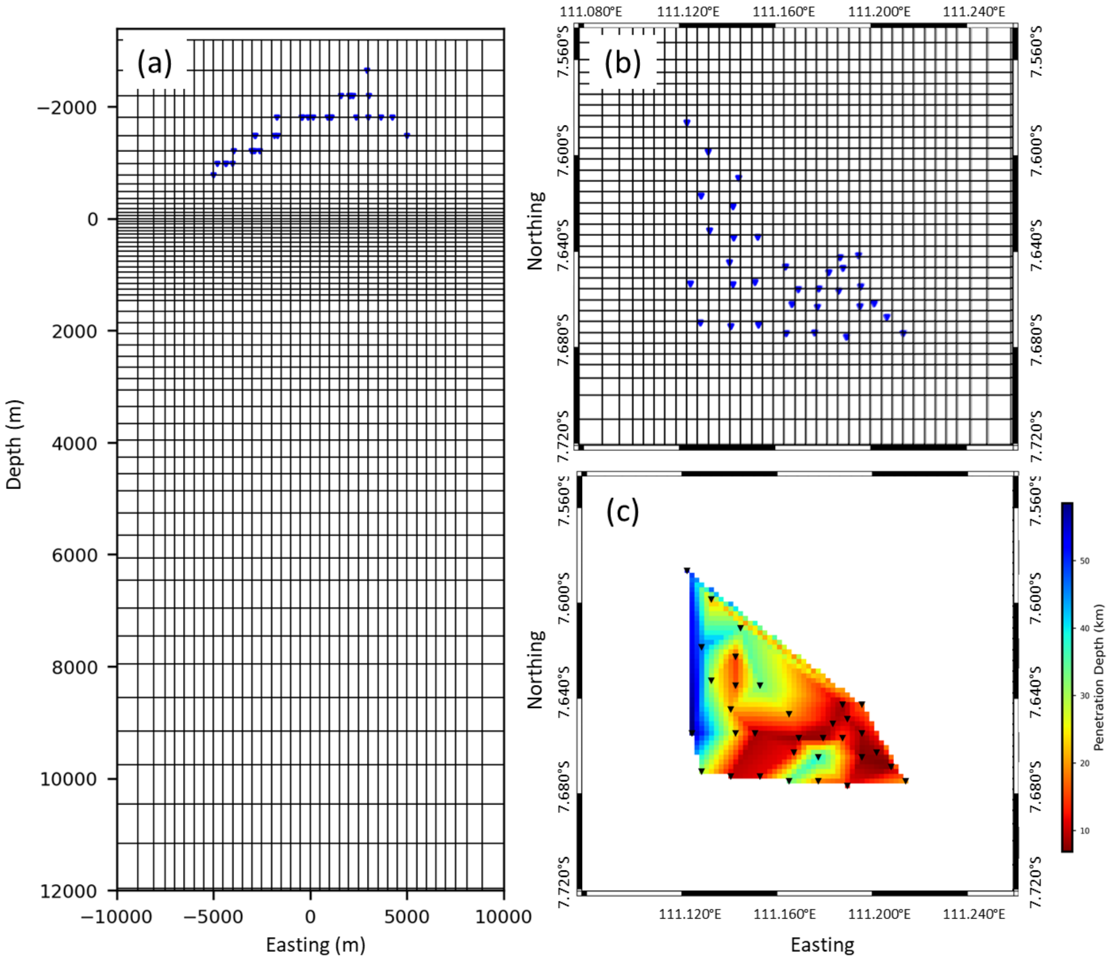

Figure 5.3. (a) Vertical and (b) horizontal model mesh for 3-D inversion and (c) maximum theoretical penetration depth for each station at the minimum frequency.

5.4 Satellite Gravity Data

Geological structures, composed of rocks with differing densities, within the Earth's interior result in variations of gravitational acceleration at every point on its surface. This study used the gravity disturbance, which is the differences between the measured gravitational acceleration and a reference gravity produced by an ellipsoid at the same observation point (P) as follows:

$$\delta g(P) = g(P) - \gamma(P), \tag{5.2}$$

where δg is the gravity disturbance and g and γ are the measured and reference gravity, respectively. The data was downloaded from the GGMplus project (Hirt et al., 2013). It has a relatively sharp resolution (7.2 arcsecs) at the latitudes between 60° N and 60° S.

5.4.1 Topography-Free Disturbance

The gravity disturbance data should be corrected to get the gravity anomaly map by removing the gravitational effect of the topography. The gravity variations caused by topography can mask or distort the gravity signal generated by subsurface structures and bodies related to the geothermal system. The process was done by forward modeling the terrain effect at each observation point. I used the topography data from the same datasets and modeled them as rectangular prisms. I assigned the Parasnis density value of 2.70 gr/cc for each prism. Analytical solutions proposed by Nagy et al. (2000, 2002) were used to calculate gravitational fields across the entire area. Therefore, the computations can be performed at any point, whether inside or outside the prism. The modified arctangent function suggested by Fukushima (2020) is utilized in the implementation to optimize the computation.

The topographic correction was applied using Harmonica (Esteban et al., 2023), a Python package for potential field data processing. The resulting terrain effect was then subtracted from the gravity disturbance value to get the topography-free disturbance δg_{TF} at a measurement point P, as follows:

$$\delta g_{TF}(P) = \delta g(P) - \sum_{i=1}^{N} T_i(P), \tag{5.3}$$

where T_i is the gravitational acceleration due to the i-th topographic prism, and N is the total number of prisms in the terrain model. The value is equivalent to the traditional Bouguer anomaly as both methods mean removing the impact of the Earth's topography from the measured gravity signal. The Bouguer anomaly g_B is, however, relies on a more general approach where the gravity disturbance is subtracted by Bouguer reduction δg_B at measurement point P, as follows:

$$g_B(P) = \delta g(P) - \delta g_B(P), \tag{5.4}$$

where,

$$\delta g_B(P) = 2\pi\rho G H(P). \tag{5.5}$$

In the above equation, G is the gravitational constant, ρ is the average density of the rocks or materials, and H denotes the elevation at point P (Hofmann-Wellenhof and Moritz, 2006).

The corrected signal can then identify and map subsurface features more accurately. However, the topography-free disturbance may still contain gravity contributions from subsurface features that are not interesting or resolved. Anomaly separation was performed to identify and map these subsurface features to separate regional and local anomalies. The decomposition was done by first estimating the wavelength and the depth of regional and local gravity sources through spectral analysis. Butterworth filtering was then used to filter out the unwanted signal so that only the regional or local anomaly remained. Depth estimate calculations based on slope analysis in the power spectrum (Spector and Grant, 1970) imply that the regional and residual depths are approximately 15 km and 4 km, respectively, as shown in Figure 5.4. The resulting regional and residual anomalies are shown in Figure 5.5. Derivative analysis was then carried out based only on the residual anomaly. It provides a more detailed and focused view of the local gravity field that may contain local geological features related to the geothermal system, including rock types, faults, and hydrothermal activities.

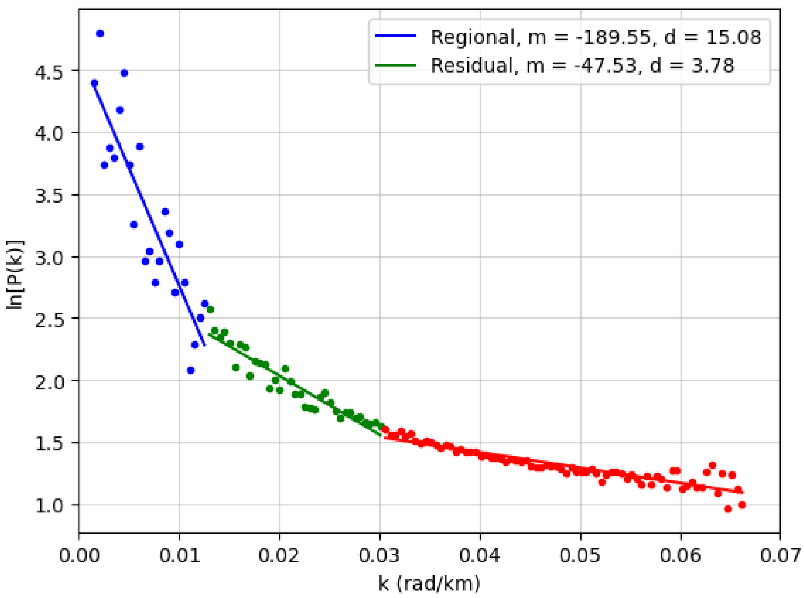

Figure 5.4. Power spectrum analysis of gravity data showing the depth estimation (d) for regional and residual anomaly based on the slopes (m).

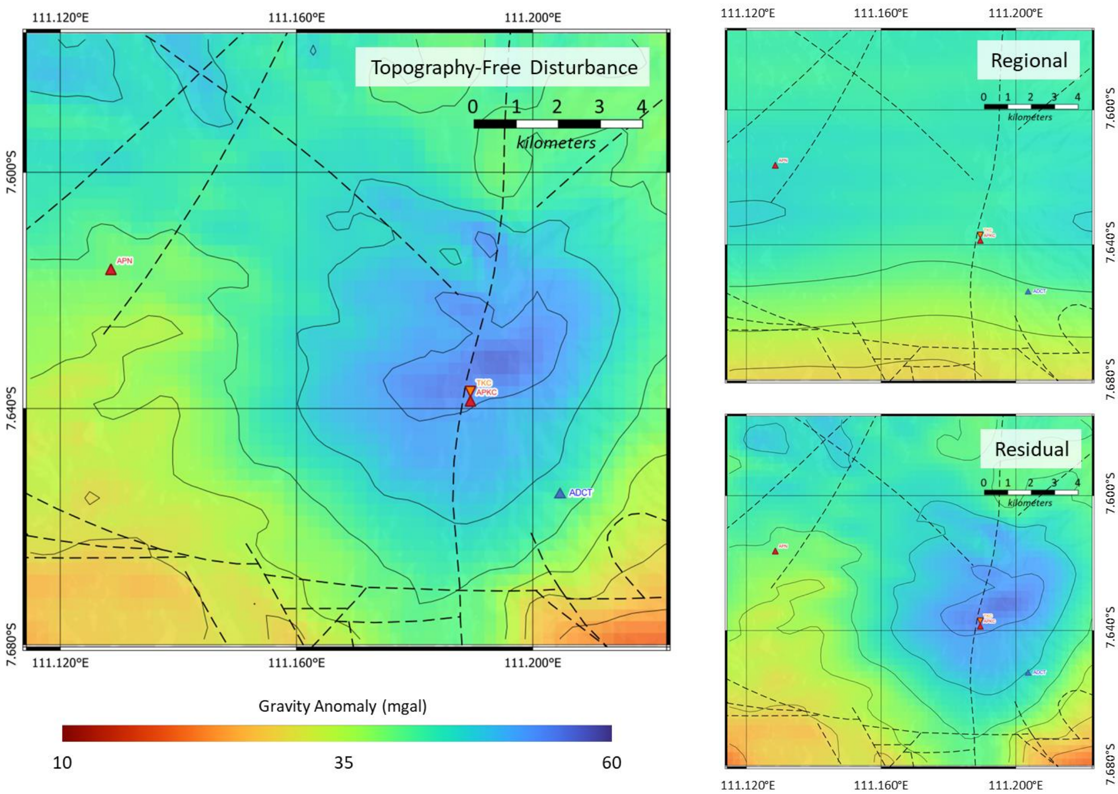

Figure 5.5. The topography-free gravity disturbance map and the regional and residual maps resulting from anomaly separation.

5.4.2 Derivative Analysis

I applied several derivative analyses to this data to emphasize the edges of each anomalous source and detect geological boundaries corresponding to faults. Three kinds of derivative formulas were used on this dataset, including the horizontal derivative (HD), vertical derivative (VD), and theta map (TM). The results are shown in Figure 5.6.

A horizontal derivative map of gravity Bouguer anomaly provides insights into the subsurface's lateral variations in density and structure. The map can highlight areas where the changes in gravity are occurring rapidly and indicate the presence of subsurface geological structures, such as faults or geological contacts, indicating areas of geothermal potential (Maithya et al., 2020; Saibi et al., 2022). The left-hand side of Figure 5.6 (HD) shows that the high horizontal gradients mainly coincide with the regional faults (dashed lines). One of the most significant horizontal variations in gravity across the study area is observed in the southern region. This area contains structural faults corresponding to the boundaries between ancient volcanic rock formed by the Jobolarangan volcano and more recent volcanic materials from Mount Lawu. Additionally, steep anomalies are present in the northern and southern areas of the fumarolic discharge, which aligns with the pre-existing N-S fault in this zone. The result also shows some moderately high gravity gradients at the eastern part of the APN hot spring area, which seems to be oriented NW-SE.

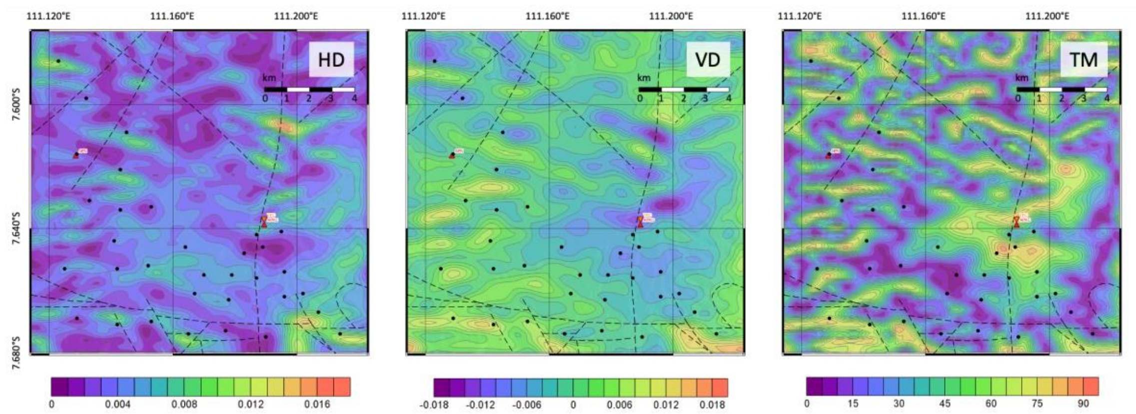

Figure 5.6. The results of residual gravity derivative analysis, including the horizontal derivative (HD), vertical derivative (VD), and theta map (TM).

The first vertical derivative map of gravity anomaly is shown in the center of Figure 5.6 (VD). In geophysical exploration, a vertical gradient map is used to highlight areas where the changes in gravity are occurring vertically and indicate the presence of edges or boundaries of geological structures, such as sedimentary basins or volcanic structures (De Ritis et al., 2010; Gönenç, 2014; Sandwell and Smith, 1997; Vaish and Pal, 2015). In geothermal exploration, the vertical derivative map can also help identify the location of high-density bodies, such as magmatic intrusions, indicating areas of geothermal potential. Based on the map, the southern and western regions have the highest vertical gradients, which aligns with the NW-SE regional fault. The map suggests that there could be denser material deep down or a steeply dipping geological structure like a fault in the southern part of the map. Another exciting feature of this map is the low or negative vertical gradients near the fumarole manifestation. That could indicate the possibility of a geothermal up-flow zone with a lower density than the surrounding colder rocks. The low-density anomaly is probably produced after the rock composition and compaction change due to a significant hydrothermal alteration event.

Another gravity derivative analysis used in this study is a theta map, a graphical representation of the orientation of geological structures relative to the gravity field, as shown on the right-hand side of Figure 5.6 (TM). By calculating the frequency of the spatial variations in the gravity data, the theta map can detect the edge of the potential sources and, therefore, can identify areas where subsurface structures intersect or where lithology changes occur (Eldosouky et al., 2022; Kumar et al., 2019; Sarkar et al., 2022). A detailed explanation of calculating the theta map from potential field data is presented by (Wijns et al., 2005). The high degree of theta corresponds to shorter wavelength spatial variations, which are usually caused by the presence of geological faults. According to the theta map, high theta values mostly align with the known Mt. Lawu lineament systems, which are oriented radially from the mountain`s peak. The most interesting feature of this map is the area with high theta values around the location of the fumarolic discharge. This feature may suggest the existence of unseen local fault systems controlling the fluid flow in the up-flow zone.

5.4.3 Gravity 3-D Inversion

Three-dimensional gravity inversions are used in geophysical exploration to create a 3-D subsurface model based on the measured gravity anomaly data. In this study, the inversion was performed using SimPEG (Simulation and Parameter Estimation in Geophysics), an open-source Python package designed to analyze geophysical data (Cockett et al., 2015). The use of SimPEG in gravity inversions, especially in volcanology and geothermal research, has been successfully demonstrated in several studies (Ardestani et al., 2022; Miller et al., 2022, 2017; Mitchell et al., 2023). The gravity inversion aims to find a density distribution model that best explains the observed gravity anomaly data by minimizing the composite objective function (ϕ) as:

$$\phi(\boldsymbol{m}) = \phi_d(\boldsymbol{m}) + \beta\phi_m(\boldsymbol{m}), \tag{5.6}$$

where β is the trade-off parameter between data misfit (ϕ_d) and model objective function (ϕ_m). I applied the β-scheduling scheme, which is made possible by SimPEG, to find the optimum β value iteratively. The data misfit is used to ensure that the model produces the forward response $F(\boldsymbol{m})$ that fits the observed data vector ($\boldsymbol{d_{obs}}$) and is expressed as:

$$\phi_d(\boldsymbol{m}) = \|\boldsymbol{W}_d(F(\boldsymbol{m}) - \boldsymbol{d}_{obs}\|^2, \tag{5.7}$$

which is known as the L2 norm of a weighted residual. The term $\boldsymbol{W_d}$ is a diagonal data weighting matrix containing the data uncertainties' reciprocal. The assigned data uncertainty for each datum was 1% of the maximum observed value. The model objective function, also known as the regularization function, is used to determine how I impose a plausible geological structure in the reconstructed model and to stabilize the inversion process. I used the smoothness-constrained L2 norm weighted least squares regularization with the iteratively updated sensitivity weighting.

The model was reconstructed based on the residual gravity anomaly. The subsurface model was represented as a grid of cells in a tensor mesh, with each cell assigned a density value. The horizontal cell size used in the inversion was 200 x 200 m, and I added 2 km of padding on each side of the grid to reduce edge effects. The total number of cells in easting and northing directions is 69 and 66, respectively. The thickness of each cell was 200 m for the first 2 km depth, then increasing by a factor of 1.3 for each subsequent layer until reaching the base of the grid at 8.8 km depth. The total number of vertical layers is 37. The model depth was chosen in accordance with the depth of residual anomaly calculated earlier so that it could be deep enough to include essential geologic structures while providing an adequate level of detail. In advance, I assigned a bound of density contrast (from 2.3 to 3.3 gr/cc) to constrain the inversion process. This boundary is determined based on the various densities of rocks in the field, including the altered minerals and the unaltered volcanic basalt. I used the density table from Sharma (1997) for the reference values.

In addition to the gravity data, I included topography data in the inversion model. During the inversion process, the inversion cells with air density would remain unchanged (inactive). That allowed us to accurately account for the gravitational effects of the Earth's surface, which can vary significantly depending on the area's topography. The final inverted model was then compared and validated using prior geological knowledge and the resistivity model from the MT inversion.

5.5 Inversion Results

5.5.1 MT Inversion Result

To image subsurface resistivity structures, which can provide information about permeability and the presence of hydrothermal fluids, the MT data were inverted using a 3-D non-linear conjugate gradient scheme based on the full-impedance tensor data. I assign the error floor of 5% and 10% for the off-diagonal and diagonal components, respectively. During the inversion process, the regularization parameter (α) was updated iteratively to maintain an efficient and stable inversion (Zhang et al., 2012; Zhou et al., 2020).

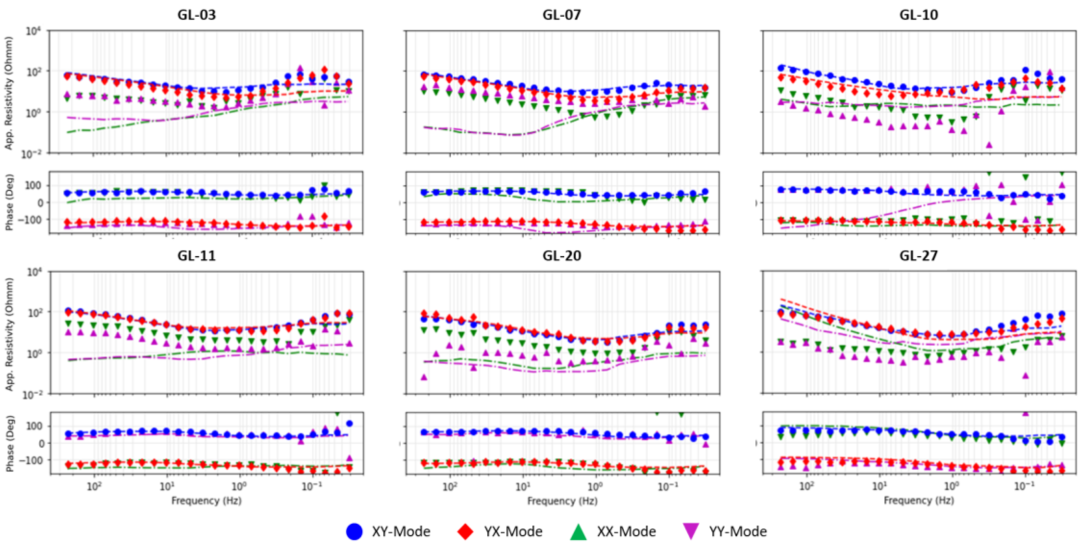

Figure 5.7. Comparison between observed (dotted) and inverted (dashed) apparent resistivity and phase curves at several MT stations after the last iteration.

The inversion was stopped after 79 iterations with an overall root mean squared error (RMS) of 6%. Figure 5.7 compares the observed and calculated apparent resistivity and phase from six sample stations after the last iteration. These results show that the inversion process was acceptable, as the curves inverted from the model generally fit the observed data within the assigned uncertainties over most locations and frequencies. For the diagonal components, however, the inverted curves could not properly fit the observed data, which could be caused by their tendency to have a larger error than the off-diagonal ones. Thus, they are typically down-weighted during the inversion process (Roots and Craven, 2017).

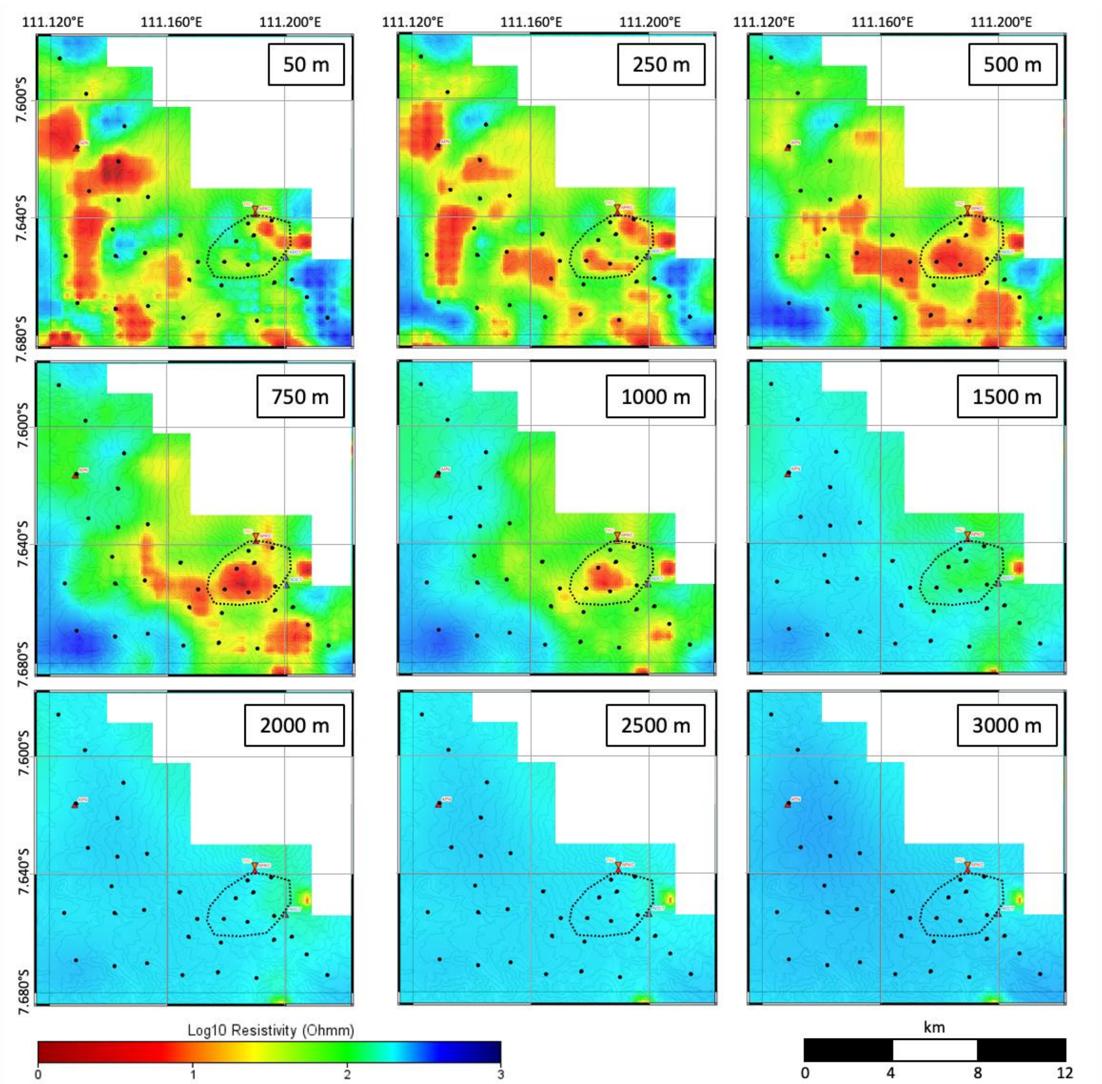

Figure 5.8. Depth slices of the resistivity model from the 3-D magnetotelluric inversion result.

Figure 5.8 shows a series of depth slices through the electrical resistivity model (ranging from 50 to 3,000 m) resulting from the 3-D MT inversion. Most of the cells in the northeastern part of the mesh were masked out since insufficient MT stations constrain the model in this region. These depth slices image shallow conductive bodies between the fumarole and hot spring manifestation points. It is apparent from Figure 5.7 that the thickness of these low resistivity anomalies varies spatially. The conductive blocks next to the fumarole are generally thicker and more conductive than those at Mount Lawu's western flank. It could indicate a more extensive zone of hydrothermal alteration under this location (marked with dashed circles) since the low resistivity anomalies commonly represent the existence of impermeable clay cap rock. Since the high temperature can also reduce the resistivity of the rock, the low resistivity values could also mark the more geothermically active area (Ussher et al., 2000).

Beneath the base of the highly conductive alteration zone at a depth of 1,500 m, there is a marked increase in resistivity across the entire model. However, a more subtle conductive anomaly extends directly beneath the extensive alteration zone. This finding may indicate a hydrothermal reservoir zone, where the less conductive alteration minerals such as illites and epidotes are formed due to the reaction between the rock matrix and very high-temperature hydrothermal fluids (Ussher et al., 2000). However, the model provides no evidence of the geothermal source rock at the deeper depths. These results provide an essential insight into the distribution of conductive and resistive zones, which can be used to delineate the existing geothermal system.

5.5.2 Gravity Inversion Result

The 3-D inversion of residual gravity anomaly was performed to provide a reliable estimation of the depth and geometry of anomalous density structures. Information about rock densities is essential to understand how the geothermal system was formed and which rock types are included. The 3-D least-squares inversion routine, which employs a Gauss-Newton conjugate gradient algorithm to minimize the objective function, was used to recover the density contrast model. Figure 5.9 displays the difference between the observed data and the calculated gravity value from the inversion model. The estimated anomaly is smoother than the observed one, which could be the effect of using the L2-norm regularization in the inversion. From the map of the normalized misfit at the last iteration, shown on the right-hand side of Figure 5.9, it can be seen that the computed anomaly generally fits well with the observed data, indicating an acceptable inversion result.

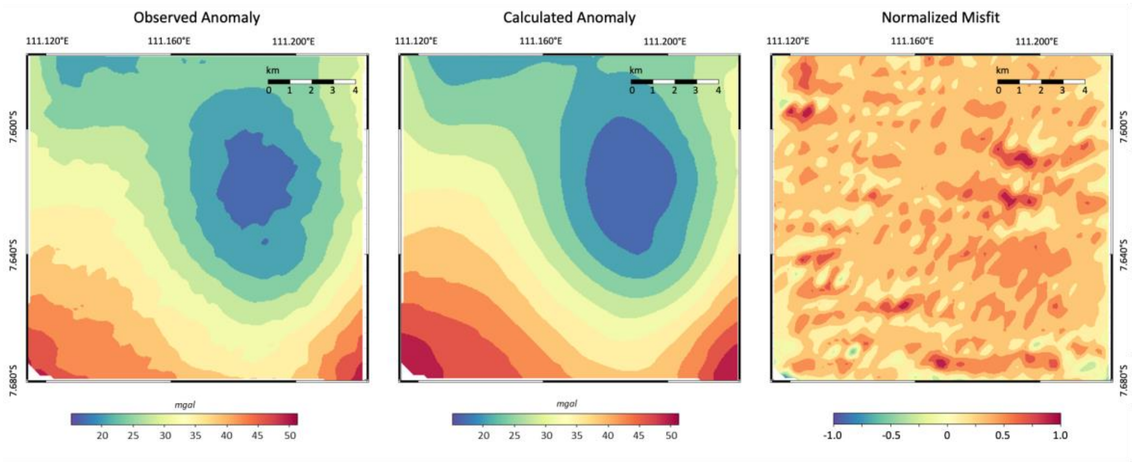

Figure 5.9. Comparison between the observed and predicted gravity anomaly and the misfit.

A series of depth slices of the density contrast model obtained from the gravity inversion procedure is presented in Figure 5.10. It is important to note that the gravity interpretation is ambiguous and uncertain as the data itself does not contain independent information about the depth of causative bodies. The colormap representation of the density model has been made similar to the one used in the MT model for easier comparison. The images in Figure 5.10 show the downward extent of low-density contrast (from -0.3 gr/cc to 0 gr/cc, relative to the mean density of 2.7 gr/cc) under Mount Lawu's body. The low-density anomaly in the shallower part could be caused by the graben caldera infill (tuffs and volcanic breccia), which is the product of the volcano-tectonic activity of Mount Lawu, as stated earlier. Considering the presence of fumarole manifestation (marked by a reversed triangle) adjacent to this anomaly, it could also suggest the existence of faults and fractures that lower the density of the rock. Some of this low-density anomaly coincides with the low resistivity anomaly (marked with dashed circles) found earlier from the MT result, indicating the presence of clay alteration. However, the lateral extent of the low resistivity body detected in the MT data is not fully comparable with the low-density anomaly since the former lacks measurement points in the northern and western flank of Mount Lawu.

The gravity model shows moderate and high-density anomalies at a more than 1,500 m depth. The moderate density contrast anomaly (ranging from 0 gr/cc to 0.1 gr/cc) is found under the previously discussed low-density counterpart. Considering the previous MT resistivity map and prior geological knowledge, this moderate density body in this location and depth could be associated with fractured and permeable volcanic rock. Hydrothermal fluids that permeate the rock matrix could also affect this density range and cause densification and metamorphism. However, it is highly uncertain since no petrological or well data supports this hypothesis. The high-density contrast anomalies (more than 0.3 gr/cc) are detected in the southeastern and southwestern corners of the study area. This rock body seems unaffected by the hydrothermal activity, which is supported by the high resistivity anomaly resulting from the MT inversion result. Based on the geological information, it could be part of the Jobolarangan volcanic rock, composed mainly of basalt rock.

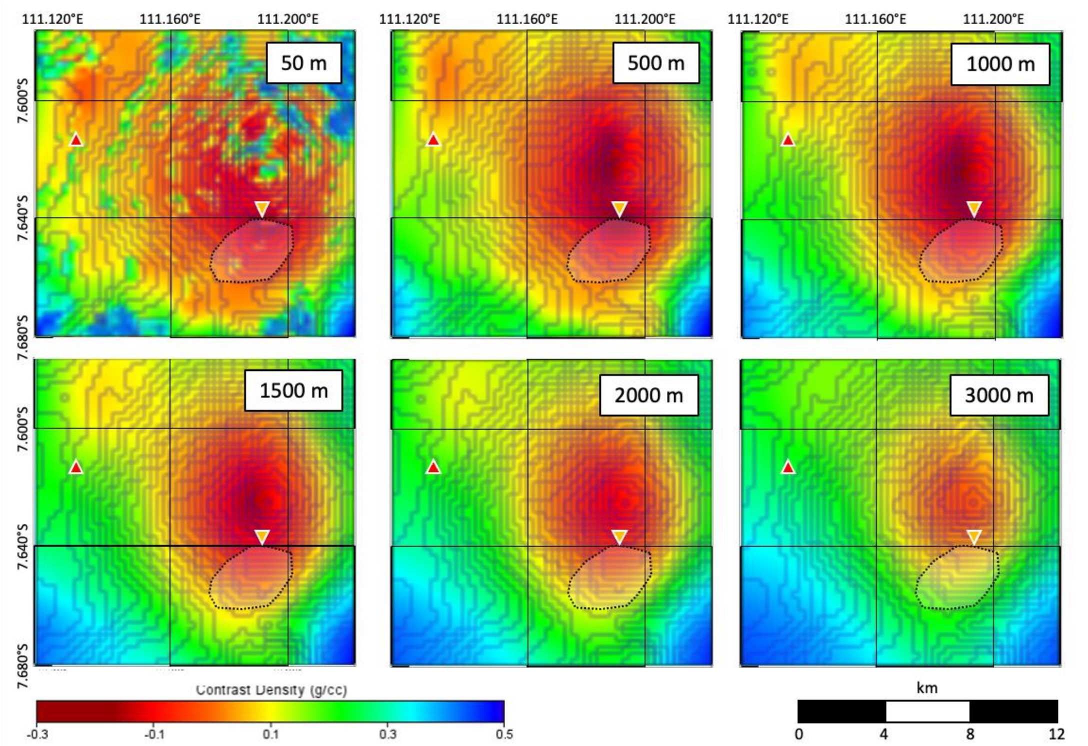

Figure 5.10. Depth slices of the density model from the 3-D gravity inversion result.

5.5.3 Integrated Interpretation

A 3-D visualization of the MT inversion result is shown in Figure 5.11. The vertical sections connect the GL-08 station (2 km South of fumarole manifestation) to the nearest hot spring (adjacent to the GL-31 station) and the rest of the MT stations in the southeastern field. The corresponding 3-D visualization of the density model is shown in Figure 5.12 so that direct comparisons can be made. However, the topography of both 3-D models does not look identical due to slight differences in the MT and gravity inversion meshes.

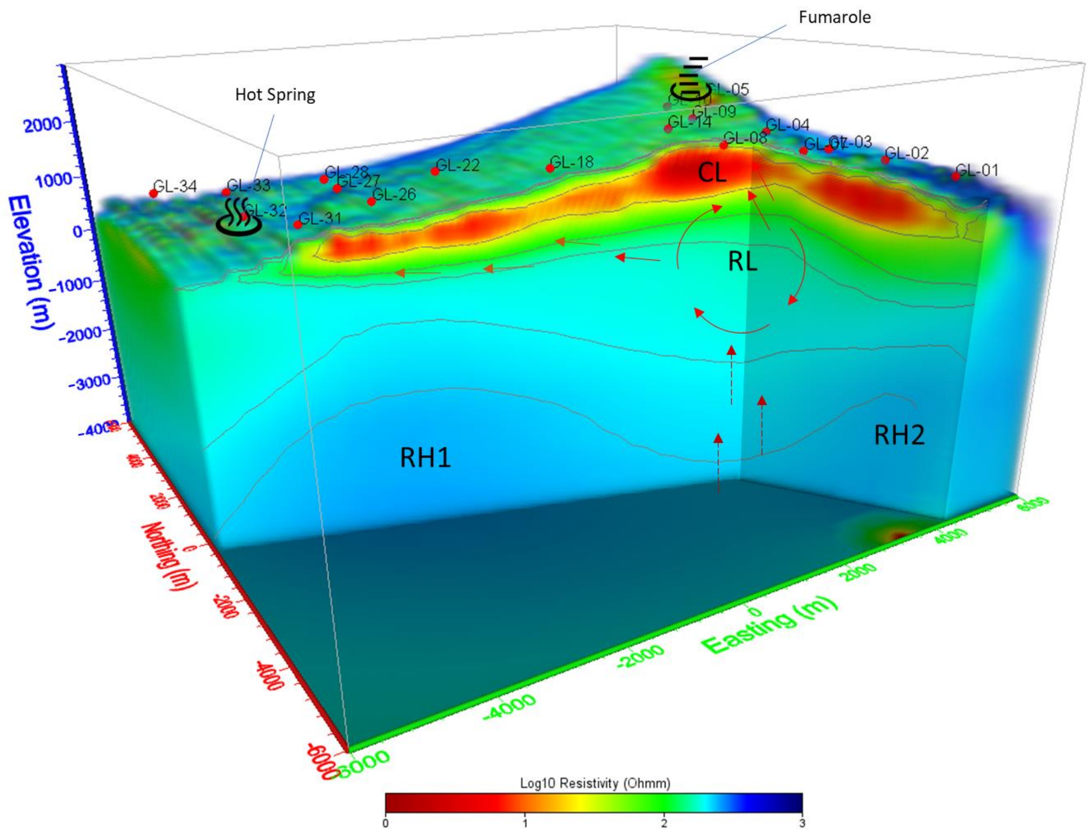

Figure 5.11. Three-dimensional MT inversion result. The vertical slice connects the fumarole near the GL-04 station and the hot spring in GL-31.

At shallow depths above 0 m elevation, the model shows a high conductivity zone (marked CL). The conductive layer is spread horizontally along the entire length of the vertical sections. This conductive layer coincides with the finding of alteration minerals in the rock samples in the same location, as Sari et al. (2021) reported. The high conductivity anomaly found under GL-08 indicates a strong-intensity alteration zone characterized by clay and goethite minerals within the sulfur deposit lithology on the surface (see Figure 5.1). The gravity result at the same zone shows a broad low-density anomaly. The density contrast in this zone is between -0.3 gr/cc and 0 gr/cc relative to the mean density of 2.7 gr/cc. This density range could represent the presence of fractured rocks, loose volcanic deposits, or heavily altered rocks. Considering the petrological study by Sari et al. (2021), heavily altered rocks seem to be the most likely explanation. The study shows that rock samples from this zone contain more than 70% clay, typically formed due to hydrothermal alteration. Taking into account all findings, the zone of high conductivity and low density beneath station GL-08 appears to be the up-flow zone where the high-temperature hydrothermal fluids use the N-S fault system (detected in geological and gravity derivative maps) as a pathway to discharge, altered the surrounding rocks and create a fumarole at the surface.

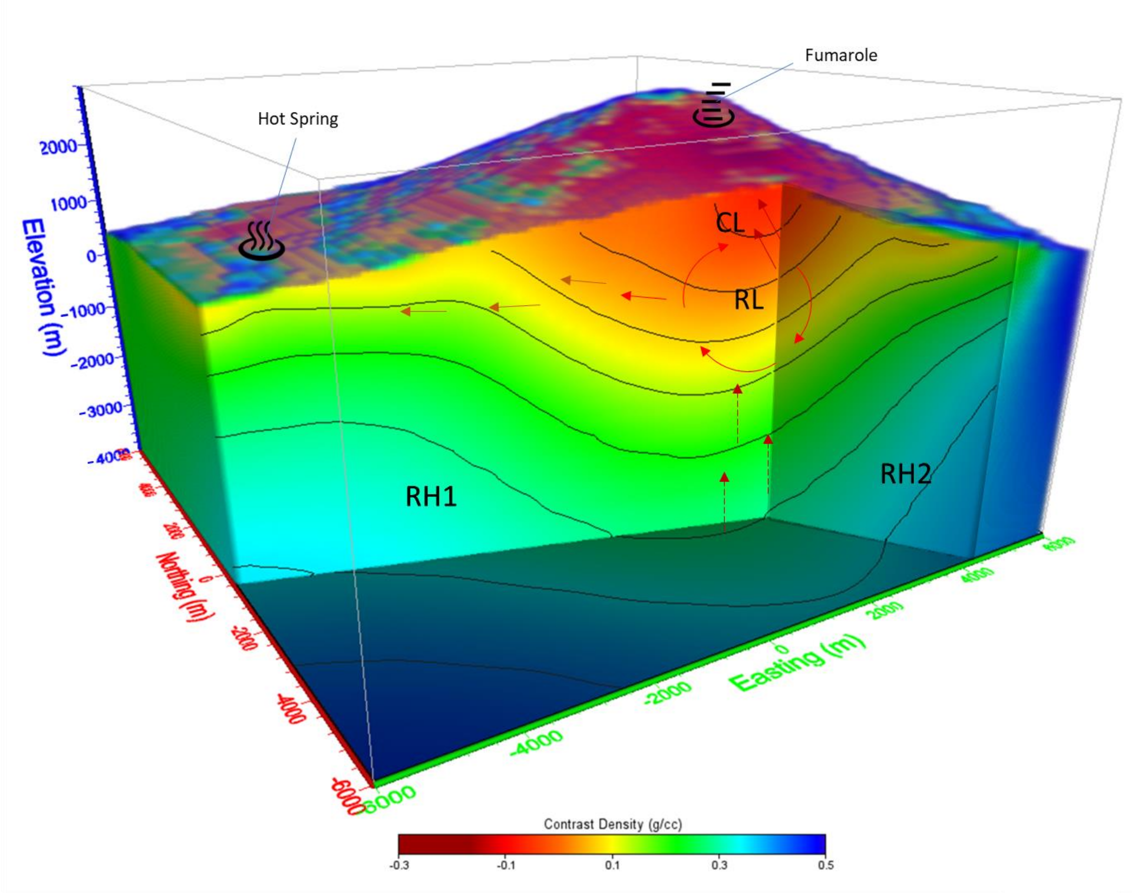

Figure 5.12. Three-dimensional gravity inversion result (showing the same section as the 3-D resistivity model).

Around GL-31, surface outcrops show less alteration where chlorite minerals appeared in volcanic breccia and pyroclastic deposits (Figure 5.1). As the degree of alteration intensity decreases, the anomalously high conductivity also gets thinner towards the western region in the MT inversion result. According to the gravity inversion, this area contains rocks with a higher density of about 2.8-2.9 gr/cc. Rocks of this density could be interpreted as a minor hydrothermal alteration of mafic lithology. These geological and geophysical observations suggest that the hot spring in the western portion of the study area may serve as a lateral outflow zone where the hydrothermal fluids come to the surface. Additionally, the gravity gradient analysis explained earlier shows the possible existence of an NW – SE fault system around this area, which may function as a passageway for fluids.

In the MT model, the area below the center of the low resistivity zone is marked RL, defined by the intermediate level of resistivity values. This resistivity range is typical in areas where volcanic rocks reacted with hydrothermal fluids at high temperatures, producing less conductive alteration minerals such as illite and epidote (Árnason et al., 2010; Flovenz et al., 2005; Gasperikova et al., 2015). However, there is still no petrological evidence supporting the presence of those minerals. On the other hand, this region also has a relatively low density based on the gravity inversion. The density is mainly affected by fractures, faulting, and permeable volcanic rocks, which form preferential passageways for the hydrothermal fluids to saturate, flow, and circulate. My models suggest that this area serves as the geothermal reservoir where the hydrothermal fluids are being heated and should, therefore, be the main target of geothermal exploration around Mount Lawu.

Below the low resistivity zone (RL) and on the opposite sides of the vertical sections, the inversion models show highly resistive and dense (RH1 and RH2) bodies, which could represent unaltered volcanic rocks. Based on their high resistivity and density, these rocks appear unaffected by hydrothermal activity and have low temperature, porosity, saturation, and permeability. According to the geological data, it is likely a part of Jobolarangan volcanic rock, mainly composed of basalt. A more intermediate resistivity zone is present between these more resistive bodies at the point of convergence of the two vertical slices. The density in this zone is also less than its surroundings (2.7 – 2.9 gr/cc), which may indicate an andesite-basaltic body that is crystallized and densified due to a very high-temperature hydrothermal fluid. This zone may serve as the conducting channel through which heat emanates from a deep-down geothermal heat source. The body of the heat source may be located deeper than the modeling depth and, therefore, could not be resolved using these MT and gravity data. In a liquid-dominated geothermal system where the reservoir temperature reaches more than 250°C (Bagaskara et al., 2021), the heat source should be close to the system and young enough to have an enormous heat content (Gupta and Roy, 2006). In this geothermal field, one potential heat source could be a young intrusive magma of Mount Lawu, where the heat reaches the reservoir system through a faulting system (most probably the N-S oriented Lawu fault). Integrating MT and gravity subsurface models in this study has yielded a valuable understanding of the geothermal system. The inversion process has revealed resistivity and density features that align with the typical physical characteristics of each component of a geothermal resource. However, additional borehole drilling data could achieve a more comprehensive conceptual model of the Mount Lawu geothermal area. The potential for further exploration and development of this resource is promising, and with continued research and investment, it could prove to be a valuable asset in pursuing sustainable energy.

5.6 Concluding Remarks

This study aimed to understand the geothermal potential in the Mount Lawu prospect area based on magnetotelluric and gravity data analysis. The idea is to jointly interpret 3-D subsurface resistivity and gravity models to image the existing geothermal system, including the structure of the reservoir, impermeable clay cap, hydrothermal fluid flow pathways, and the depth of the magmatic heat source. The results show that the geothermal system's primary location is just south of Mt. Lawu and its fumarolic manifestation. This conclusion is based on the highly conductive, low-density thickest near the GL-08 MT station. This conductive layer narrows on either side, resembling an impermeable clay cap. Geothermal fluids are thought to flow along the base of the clay cap to the west, where they eventually reach the surface and form hot springs near GL-32. The geothermal reservoir is located under the thickest part of the clay cap near station GL-08. It is characterized by intermediate conductivity and low density, which is thought to result from highly fractured rocks saturated by hydrothermal fluids. Despite the models' inability to definitively image the heat source, the models offer insights into the presence of a conducting zone where the heat is transferred to the reservoir system. Additional information about rock alteration and subsurface temperature would be beneficial to establish a more comprehensive conceptual model with a higher degree of reliability.

CHAPTER 6
CONCLUDING REMARKS

6.1 Conclusions

Geothermal energy is currently one of the most emerging green energy sources on Earth, as it offers carbon-neutral and renewable forms of energy. As a home for 40% of the world's geothermal energy resources, Indonesia is looking forward to maximizing its geothermal potential through significant changes in the energy policies followed by massive geothermal exploration and development strategies. In the exploration stage, the geophysical prospecting technique is instrumental in understanding the unseen conditions of the subsurface, including the effort to locate the geothermal reservoir and imaging the entire prospect area geothermal system. The most widely used geophysical technique for geothermal exploration is the magnetotelluric method, which can image the subsurface resistivity structure of a geothermal field up to a large depth.

The magnetotelluric (MT) method utilizes the fluctuation of naturally occurring electromagnetic fields recorded on the Earth's surface. These time-varying electromagnetic (EM) fields are generated due to the disturbance of the solar wind and lightning activities against the Earth's natural magnetic field. In time, the variation of EM fields induces the subsurface rocks and materials concerning their electrical properties. The recorded electric and magnetic time series data will undergo several data processing steps before finally providing information about the subsurface electrical resistivity structure. However, the natural MT signal has a weak amplitude and is highly susceptible to EM noise interference, especially when the survey location is adjacent to an urban area. Due to this problem, the reliability of the magnetotelluric method to accurately image the subsurface resistivity becomes questionable.

Many attempts have been made to address this issue, including remote reference (RR) technique and robust estimation. However, finding a suitable remote station is difficult due to current industrialization. On the other hand, the robust estimation technique becomes counterproductive when dealing with cultural EM noises since they are usually correlated and affect most parts of the recording. In recent years, many denoising efforts have utilized deep learning to separate signals from noise in many research fields. This study proposes an MT time series denoising method adapted from the neural network architecture. Since the EM noises have certain patterns and characteristics, the trained neural network can autonomously discriminate those noises when unseen noisy data is fed to the network. Firstly, synthetic MT time series data was generated. Four typical EM noises were added to the clean synthetic data before being used as the training input and output. Since the patterns and characteristics of each noise source are different, the neural network model and parameters were made unique for each of them. On the one hand, convolutional neural networks (CNN) were utilized to learn the temporal noises, such as pulse (spike) and triangle noises. On the other hand, the recurrent neural networks (RNN) algorithms were used to identify more continuous noises, such as signal step or jump, and sinusoidal noise due to power grid interference. The training processes result in a modular denoiser system whose usage can be tailored according to the type of noises contaminating the data. The performance of the denoising machine has been tested, and the quality of MT time series data has been improved.

Another major issue in geothermal exploration using the MT method is inverse modeling. Subsurface electrical resistivity distribution needs to be revealed through the inversion process to explore the geothermal potential, as the components in geothermal systems could be easily characterized by their resistivity contrasts. One of Indonesia's most promising geothermal potentials is located in the Danau Ranau prospect area. I performed a three-dimensional inversion based on the MT impedance tensor and tipper vector to understand its geothermal system. Prior dimensionality analysis using phase tensor revealed that the MT data contains a high dimensionality distortion and shows significant horizontal geoelectrical variations. The three-dimensional inversion was then carried out after taking control of the model mesh dimension and the regularization parameter. The 3-D resistivity model showed an overburden layer with varying resistivity in the shallow depth. In the subsequent layer, a conductive anomaly representing impermeable cap rock is distributed from the center to the northern and western parts of the study area, bordered by faults and manifestations. All the findings agree with the existing geological and geochemical survey data and can explain the hydrothermal activities in the Danau Ranau geothermal prospect area.

The MT method was also applied to geothermal exploration in the Mount Lawu geothermal area. Satellite gravity data was incorporated to support the resistivity model describing the geothermal system. It is inferred from the gravity derivative analysis that fault structures exist in a location with high permeability, which acts as a controlling structure for geothermal manifestations. The 3-D resistivity modeling was carried out for MT data based on the full-impedance component, while the 3-D density model was reconstructed based on the residual anomaly computed from topography-free gravity disturbance. The 3-D resistivity model from magnetotelluric inversion shows a distribution pattern of clay cap centered at the southern part of the mountain peak with a thickness of about 1 kilometer, and it narrows to the western region where the hot spring appeared as an outflow manifestation. The gravity data shows an agreement as the low-density bodies are detected at the exact location, indicating the presence of highly altered and fractured rocks. The integration of resistivity and density models shows that the geothermal reservoir is subsequently seated around similar horizontal coordinates, while the heat from the heat source emanates from the conducting passage deeper down than the reconstructed models.

As a conclusion of all the works done in this study, it is apparent that the modular time series denoiser works well as an alternative to filter out unwanted noises from the MT signal. The method was able to recover the clean signal without missing important information. In the later stages of data processing, the 3-D inversion of MT data was able to delineate the subsurface conditions concerning the existing geothermal system in the Danau Ranau and Mount Lawu geothermal prospect area.

6.2 Recommendations

Although the results are satisfying, there is room for improvement to enhance this research. I have identified three main concerns, which I outline below. Developing a system that automatically identifies segments requiring attention would be helpful. Additionally, building a noise removal system that can learn patterns from all measurement channels at once, rather than fixing each component individually, would enhance the benefits of this method. For future work of Danau Ranau geothermal prospecting, investigating gravity variations in the geothermal area would also be beneficial. The subsurface density distribution and controlling geological structures delineated from the gravity study could then be integrated into the model resulting from this study. These continued efforts could lead to a more reliable conceptual model of the geothermal system in Danau Ranau prior to its exploitation stage. For the Mount Lawu case, additional information about rock alteration and subsurface temperature would aid in establishing a more comprehensive conceptual model with higher reliability. I hope advancements in MT survey, processing, and modeling technology will continue improving MT exploration, especially related to geothermal prospections.

ACKNOWLEDGMENTS

All praises are due to Allah Azza wa Jalla, the Most Gracious, the Most Merciful, for the countless blessings He has bestowed upon me throughout my life. I firmly believe that all the good things that have happened to me result from His benevolence. I am thankful to Allah for providing me with the resources, knowledge, and skills to complete my doctoral studies successfully.

I am writing to express my sincere gratitude to my supervisor, Associate Professor Hideki Mizunaga, for his invaluable guidance, support, and encouragement throughout my academic journey. His insightful feedback and constructive criticism have inspired me to strive for excellence and enabled me to grow personally and professionally. I also want to thank Assistant Professor Toshiaki Tanaka for my research and countless help, constructive suggestions, and criticisms.

I would like to express my sincere gratitude to the Japan Science and Technology Agency for their immensely generous financial support through the K-SPRING Program. Their assistance has been instrumental in advancing my research and studies and has provided me with invaluable opportunities to grow and develop as a researcher. The interdisciplinary approach taught in the MIRAI course has been incredibly enriching and opened up new research avenues that would not have been possible otherwise.

I would like to thank all the members of the Exploration Geophysics Laboratory for their invaluable assistance and unwavering support. Their contributions have been instrumental in the success of my project. I am truly grateful for their willingness to go above and beyond to help me with every step of the process and make it a truly collaborative and fulfilling experience.

Lastly, I thank my wife, Desy Rhobiatul Adhawiyah, my son, Mushab Abdurrahman, and my daughter, Asiyah Amaturrahman, for their accompany and moral support throughout this journey.

LIST OF REFERENCES

Abdelfettah, Y., Tiercelin, J.J., Tarits, P., Hautot, S., Maia, M., Thuo, P., 2016. Subsurface Structure and Stratigraphy of The Northwest End of The Turkana Basin, Northern Kenya Rift, As Revealed by Magnetotellurics and Gravity Joint Inversion. Journal of African Earth Sciences 119, 120–138. DOI: 10.1016/J.Jafrearsci.2016.03.008

Abdelzaher, M., Nishijima, J., Saibi, H., El-Qady, G., Massoud, U., Soliman, M., Younis, A., Ehara, S., 2012. A Coastal Aquifer Study Using Magnetotelluric and Gravity Methods In Abo Zenema, Egypt. Pure Appl Geophys 169, 1679–1692. DOI: 10.1007/S00024-011-0407-Y/Tables/1

Afiat, Idianto, O., Rera, G.F., Wardoyo, G.K., Sutopo, Pratama, H.B., Hamdani, M.R., 2021. Updated Conceptual Model and Resource Assessment Using Numerical Reservoir Simulation of Danau Ranau Geothermal Field Indonesia, in: IOP Conference Series: Earth and Environmental Science. IOP Publishing Ltd. DOI: 10.1088/1755-1315/732/1/012027

Anderson, E., Ussher, G., Crosby, D., 2000. Bulls Eye! – Simple Resistivity Imaging To Reliably Locate The Geothermal Reservoir, in: Proceedings World Geothermal Congress. Beppu.

Ardestani, V.E., Fournier, D., Oldenburg, D.W., 2022. A Localized Gravity Modeling of The Upper Crust Beneath Central Zagros. Pure Appl Geophys 179, 2365–2381. DOI: 10.1007/S00024-022-03065-1/Metrics

Ardid, A., Dempsey, D., Bertrand, E., Sepulveda, F., Tarits, P., Solon, F., Archer, R., 2021. Bayesian Magnetotelluric Inversion Using Methylene Blue Structural Priors For Imaging Shallow Conductors in Geothermal Fields. Geophysics 86, E171–E183. DOI: 10.1190/Geo2020-0226.1/Asset/Images/Large/Figure8.Jpeg

Arisbaya, I., Wijanarko, E., Warsa, Sumintadireja, P., Sudrajat, Y., Handayani, L., Mukti, M.M. Ruf, Grandis, H., 2023. Magnetotellurics (MT) and Gravity Study of A Possible Active Fault in Southern Garut, West Java, Indonesia. International Journal of Geophysics 2023. DOI: 10.1155/2023/4482074

Árnason, K., Eysteinsson, H., Hersir, G.P., 2010. Joint 1D Inversion of TEM and MT Data and 3d Inversion of MT Data in The Hengill Area, Sw Iceland. Geothermics 39. DOI: 10.1016/J.Geothermics.2010.01.002

Ars, J.M., Tarits, P., Hautot, S., Bellanger, M., Coutant, O., Maia, M., 2019. Joint Inversion of Gravity and Surface Wave Data Constrained By Magnetotelluric: Application To Deep Geothermal Exploration of Crustal Fault Zone in Felsic Basement. Geothermics 80, 56–68. DOI: 10.1016/J.Geothermics.2019.02.006

Atef, H., Abd El-Gawad, A.M.S., Abdel Zaher, M., Farag, K.S.I., 2016. The Contribution of Gravity Method in Geothermal Exploration of Southern Part of The Gulf of Suez–Sinai Region, Egypt. Nriag Journal of Astronomy and Geophysics 5, 173–185. DOI: 10.1016/J.Nrjag.2016.02.005

Bagaskara, M.F., Oktaviani, A.D., Setyadi, R., Yoga, D.A., Sahdarani, D.N., Kurniadi, D.T., 2021. Gas Geochemistry Analysis in Candradimuka Crater, Mount Lawu, Central Java, Indonesia. IOP Conf Ser Earth Environ Sci 851, 012036. DOI: 10.1088/1755-1315/851/1/012036

Başokur, A.T., Koçyiğit, A., Hacıoğlu, Ö., Arslan, H.İ., Meqbel, N., 2022. Magnetotelluric Imaging of The Shallow-Seated Magma Reservoir Beneath The Karadağ Stratovolcano, Central Anatolia, Turkey. Journal of Volcanology and Geothermal Research 427, 107567. DOI: 10.1016/J.Jvolgeores.2022.107567

Båth, M., 1965. Lateral Inhomogeneities of The Upper Mantle. Tectonophysics 2, 483–514. DOI: 10.1016/0040-1951(65)90003-X

Becken, M., Ritter, O., 2012. Magnetotelluric Studies At The San Andreas Fault Zone: Implications For The Role of Fluids. Surv Geophys 33. DOI: 10.1007/S10712-011-9144-0

Beka, T.I., Smirnov, M., Birkelund, Y., Senger, K., Bergh, S.G., 2016. Analysis and 3d Inversion of Magnetotelluric Crooked Profile Data From Central Svalbard For Geothermal Application. Tectonophysics 686. DOI: 10.1016/J.Tecto.2016.07.024

Bell, J.B., Tikhonov, A.N., Arsenin, V.Y., 1978. Solutions of Ill-Posed Problems. Math Comput 32. DOI: 10.2307/2006360

Berdichevsky, M.N., Dmitriev, V.I., Golubtsova, N.S., Mershchikova, N.A., Pushkarev, P.Y., 2003. Magnetovariational Sounding: New Possibilities. Izvestiya, Physics of The Solid Earth 39.

Berdichevsky, M.N., Golubtsova, N.S., Varentsov, I.M., Pushkarev, P.Y., Rybin, A.K., Sokolova, E.Y., 2010. Geoelectric Section of The Central Tien Shan: Sequential Inversion of The Magnetovariational and Magnetotelluric Data Along The Naryn Line. Izvestiya, Physics of The Solid Earth 46, 698–706. DOI: 10.1134/S1069351310080069

Berdichevsky, M.N., Kuznetsov, V.A., Pal'shin, N.A., 2009. Analysis of Magnetovariational Response Functions. Izvestiya, Physics of The Solid Earth 45, 179–198. DOI: 10.1134/S106935130903001x

Bibby, H.M., Caldwell, T.G., Brown, C., 2005. Determinable and Non-Determinable Parameters of Galvanic Distortion in Magnetotellurics. Geophys J Int 163. DOI: 10.1111/J.1365-246x.2005.02779.X

Booker, J.R., 2014. The Magnetotelluric Phase Tensor: A Critical Review. Surv Geophys 35, 7–40. DOI: 10.1007/S10712-013-9234-2/Tables/2

Borzotta, E., 2012. Magnetovariational Information To Improve Distortion Diagnostics in Deep Magnetotelluric Soundings. Izvestiya, Physics of The Solid Earth 48, 766–783. DOI: 10.1134/S1069351312070014

Bostick, F.X., 1997. A Simple Almost Exact Method of Magnetotelluric Analysis, in: Ward, S.H. (Ed.), Workshop On Electrical Methods in Geothermal Exploration. U.S.G.S Contract 14-08-001-G-359, University of Utah.

Cagniard, L., 1953. Basic Theory of The Magnetotelluric Method of Geophysical Prospecting. Geophysics 18, 605. DOI: 10.1190/1.1437915

Caldwell, T.G., Bibby, H.M., Brown, C., 2004. The Magnetotelluric Phase Tensor. Geophys J Int 158. DOI: 10.1111/J.1365-246x.2004.02281.X

Carbonari, R., Di Maio, R., Piegari, E., D'auria, L., Esposito, A., Petrillo, Z., 2018. Filtering of Noisy Magnetotelluric Signals By Som Neural Networks. Physics of The Earth and Planetary Interiors 285, 12–22. DOI: 10.1016/J.Pepi.2018.10.004

Carrier, A., Fischanger, F., Gance, J., Cocchiararo, G., Morelli, G., Lupi, M., 2019. Deep Electrical Resistivity Tomography For The Prospection of Low- To Medium-Enthalpy Geothermal Resources. Geophys J Int 219, 2056–2072. DOI: 10.1093/Gji/Ggz411

Chave, A.D., Jones, A.G., 2012. The Magnetotelluric Method: Theory and Practice, The Magnetotelluric Method: Theory and Practice. DOI: 10.1017/Cbo9781139020138

Chave, A.D., Thomson, D.J., 2004. Bounded Influence Magnetotelluric Response Function Estimation. Geophys J Int 157, 988–1006. DOI: 10.1111/J.1365-246x.2004.02203.X

Cherkose, B.A., Saibi, H., 2021. Investigation of The Ayrobera Geothermal Field Using 3d Magnetotelluric Data Inversion, Afar Depression, Ne Ethiopia. Geothermics 94, 102114. DOI: 10.1016/J.Geothermics.2021.102114

Cockett, R., Kang, S., Heagy, L.J., Pidlisecky, A., Oldenburg, D.W., 2015. Simpeg: An Open Source Framework For Simulation and Gradient Based Parameter Estimation in Geophysical Applications. Comput Geosci. DOI: 10.1016/J.Cageo.2015.09.015

De Ritis, R., Ventura, G., Chiappini, M., Carluccio, R., Von Frese, R., 2010. Regional Magnetic and Gravity Anomaly Correlations of The Southern Tyrrhenian Sea. Physics of The Earth and Planetary Interiors 181. DOI: 10.1016/J.Pepi.2010.04.003

Dehkordi, B.H., Montahaei, M., 2016. Horizontal Magnetovariational Responses in Geothermal Exploration: Synthetic Model Studies. Geosciences Journal 20, 903–909. DOI: 10.1007/S12303-016-0010-4

Di Paolo, F., Ledo, J., Ślęzak, K., Martínez Van Dorth, D., Cabrera-Pérez, I., Pérez, N.M., 2020. La Palma Island (Spain) Geothermal System Revealed By 3d Magnetotelluric Data Inversion. Scientific Reports 2020 10:1 10, 1–8. DOI: 10.1038/S41598-020-75001-Z

Egbert, G.D., Booker, J.R., 1986. Robust Estimation of Geomagnetic Transfer Functions. Geophys J Int 87, 173–194. DOI: 10.1111/J.1365-246x.1986.Tb04552.X

Egbert, G.D., Kelbert, A., 2012. Computational Recipes For Electromagnetic Inverse Problems. Geophys J Int 189. DOI: 10.1111/J.1365-246x.2011.05347.X

Eldosouky, A.M., El-Qassas, R.A.Y., Pham, L.T., Abdelrahman, K., Alhumimidi, M.S., Bahrawy, A. El, Mickus, K., Sehsah, H., 2022. Mapping Main Structures and Related Mineralization of The Arabian Shield (Saudi Arabia) Using Sharp Edge Detector of Transformed Gravity Data. Minerals 12. DOI: 10.3390/Min12010071

ESDM, 2020. Potensi Pengembangan Panas Bumi Di Indonesia (in: Bahasa). Jakarta.

Esteban, F. D., Li, L., Oliveira Jr, V. C., Pesce, A., Shea, N., Soler, S. R., Tankersley, M., Uieda, L., 2023. Harmonica v0.6.0: Forward modeling, inversion, and processing gravity and magnetic data (v0.6.0). Zenodo. DOI: 10.5281/zenodo.7690145

Flovenz, O.G., Spangenberg, E., Kulenkampff, J., Arnason, K., Karlsdottir, R., Huenges, E., 2005. The Role of Electrical Interface Conduction in Geothermal Exploration, in: World Geothermal Congress 2005.

Fukushima, T., 2020. Speed and Accuracy Improvements in Standard Algorithm For Prismatic Gravitational Field. Geophys J Int 222, 1898–1908. DOI: 10.1093/Gji/Ggaa240

Gamble, T.D., Goubau, W.M., Clarke, J., 1979. Magnetotellurics With A Remote Magnetic Reference. DOI: 10.1190/1.1440923 44, 53–68. DOI: 10.1190/1.1440923

Gasperikova, E., Rosenkjaer, G.K., Arnason, K., Newman, G.A., Lindsey, N.J., 2015. Resistivity Characterization of The Krafla and Hengill Geothermal Fields Through 3d MT Inverse Modeling. Geothermics 57. DOI: 10.1016/J.Geothermics.2015.06.015

Gönenç, T., 2014. Investigation of Distribution of Embedded Shallow Structures Using The First Order Vertical Derivative of Gravity Data. J Appl Geophy 104. DOI: 10.1016/J.Jappgeo.2014.02.010

Gupta, H., Roy, S., 2007. Geothermal Energy: An Alternative Resource For The 21st Century, Geothermal Energy: An Alternative Resource For The 21st Century. Elsevier.

Hacıoğlu, Ö., Başokur, A.T., Diner, Ç., 2021. Geothermal Potential of The Eastern End of The Gediz Basin, Western Anatolia, Turkey Revealed By Three-Dimensional

Inversion of Magnetotelluric Data. Geothermics 91, 102040. DOI: 10.1016/J.Geothermics.2020.102040

Hermawan, D., Permana, L.A., 2018. Keprospekan Panas Bumi Gunung Lawu Berdasarkan Kajian Vulkanostratigrafi. Buletin Sumber Daya Geologi 13, 199–213. DOI: 10.47599/Bsdg.V13i3.232

Hill, G.J., Caldwell, T.G., Heise, W., Chertkoff, D.G., Bibby, H.M., Burgess, M.K., Cull, J.P., Cas, R.A.F., 2009. Distribution of Melt Beneath Mount St Helens and Mount Adams Inferred From Magnetotelluric Data. Nat Geosci 2. DOI: 10.1038/Ngeo661

Hirt, C., Claessens, S., Fecher, T., Kuhn, M., Pail, R., Rexer, M., 2013. New Ultrahigh-Resolution Picture of Earth’s Gravity Field. Geophys Res Lett 40. DOI: 10.1002/Grl.50838

Hofmann-Wellenhof, B., Moritz, H., 2006. Physical Geodesy (2nd edition ed.) Springer. Vienna. ISBN: 3-211-33544-7

Hormozzade Ghalati, F., Craven, J.A., Motazedian, D., Grasby, S.E., Tschirhart, V., 2022. Modeling A Fractured Geothermal Reservoir Using 3-D Amt Data Inversion: Insights From Garibaldi Volcanic Belt, British Columbia, Canada. Geothermics 105, 102528. DOI: 10.1016/J.Geothermics.2022.102528

Kanda, I., Fujimitsu, Y., Nishijima, J., 2019. Geological Structures Controlling The Placement and Geometry of Heat Sources Within The Menengai Geothermal Field, Kenya As Evidenced By Gravity Study. Geothermics 79, 67–81. DOI: 10.1016/J.Geothermics.2018.12.012

Kanda, W., Yamazaki, T., Ogawa, Y., Hashimoto, T., Sakanaka, S., Aizawa, K., Takakura, S., Koyama, T., Yamada, K., Kobayashi, T., Komori, S., 2013. Shallow Resistivity Structure of Sakurajima Volcano Revealed By Audio-Frequency Magnetotellurics(＜Special Section＞Sakurajima Special Issue). Bulletin of The Volcanological Society of Japan 58, 251-267. DOI: 10.18940/Kazan.58.1_251

Kaufman, A.A., Keller, G. V., 1981. The Magnetotelluric Sounding Method, in: Methods in Geochemistry and Geophysics. Elsevier Scientific Publishing Company, Amsterdam. DOI: 10.1029/Eo063i029p00578-06

Kelbert, A., Meqbel, N., Egbert, G.D., Tandon, K., 2014. Modem: A Modular System For Inversion of Electromagnetic Geophysical Data. Comput Geosci 66. DOI: 10.1016/J.Cageo.2014.01.010

Kirkby, A., Zhang, F., Peacock, J., Hassan, R., Duan, J., 2019. The Mtpy Software Package For Magnetotelluric Data Analysis and Visualisation. J Open Source Softw 4. DOI: 10.21105/Joss.01358

Kiyan, D., Jones, A.G., Vozar, J., 2014. The Inability of Magnetotelluric Off-Diagonal Impedance Tensor Elements To Sense Oblique Conductors in Three-Dimensional Inversion. Geophys J Int 196. DOI: 10.1093/Gji/Ggt470

Kumar, U., Narayan, S., Pal, S.K., 2019. New Insights On Structure and Tectonics Over The Laxmi Ridge Using Eigen6c4 Modelled Gravity Data. Indian Journal of Geo-Marine Sciences 48.

Kusuma, D.S., Widodo, S., Bakrun, Suhanto, E., Mustang, A., Foeh, I.M., Sulaeman, B., 2005. Prospek Panas Bumi Di Daerah Danau Ranau, Lampung Dan Sumatera Selatan [Geothermal Prospect in Danau Ranau Area, Lampung and South Sumatera], in: Prosiding Kolokium Hasil Lapangan - Dim 2005. Bandung, Pp. 391–398.

Larnier, H., Sailhac, P., Chambodut, A., 2016. New Application of Wavelets in Magnetotelluric Data Processing: Reducing Impedance Bias 1. Geomagnetism. Earth, Planets and Space 68, 1–11. DOI: 10.1186/S40623-016-0446-9/Figures/12

Larsen, J.J., Levy, L., Asif, M.R., 2022. Removal of Powerline Noise in Geophysical Datasets With A Scientific Machine-Learning Based Approach. Ieee Transactions On Geoscience and Remote Sensing 60. DOI: 10.1109/Tgrs.2022.3223737

Le Pape, F., Jones, A.G., Jessell, M.W., Perrouty, S., Gallardo, L.A., Baratoux, L., Hogg, C., Siebenaller, L., Touré, A., Ouiya, P., Boren, G., 2017. Crustal Structure of Southern Burkina Faso Inferred From Magnetotelluric, Gravity and Magnetic Data. Precambrian Res 300, 261–272. DOI: 10.1016/J.Precamres.2017.08.013

Ledo, J., 2005. 2-D Versus 3-D Magnetotelluric Data Interpretation. Surv Geophys 26, 511–543. DOI: 10.1007/S10712-005-1757-8

Lévy, L., Gibert, B., Sigmundsson, F., Flóvenz, O.G., Hersir, G.P., Briole, P., Pezard, P.A., 2018. The Role of Smectites in The Electrical Conductivity of Active

Hydrothermal Systems: Electrical Properties of Core Samples From Krafla Volcano, Iceland. Geophys J Int 215, 1558–1582. DOI: 10.1093/Gji/Ggy342

Li, G., Gu, X., Ren, Z., Wu, Q., Liu, X., Zhang, L., Xiao, D., Zhou, C., 2022. Deep Learning Optimized Dictionary Learning and Its Application in Eliminating Strong Magnetotelluric Noise. Minerals 12. DOI: 10.3390/Min12081012

Li, J., Peng, Y., Tang, J., Li, Y., 2021. Denoising of Magnetotelluric Data Using K-Svd Dictionary Training. Geophys Prospect 69, 448–473. DOI: 10.1111/1365-2478.13058

Maithya, J., Fujimitsu, Y., Nishijima, J., 2020. Analysis of Gravity Data To Delineate Structural Features Controlling The Eburru Geothermal System in Kenya. Geothermics 85. DOI: 10.1016/J.Geothermics.2019.101795

Manoj, C., Nagarajan, N., 2003. The Application of Artificial Neural Networks To Magnetotelluric Time-Series Analysis, Geophys. J. Int.

Martí, A., Queralt, P., Marcuello, A., Ledo, J., Rodríguez-Escudero, E., Martínez-Díaz, J.J., Campanyà, J., Meqbel, N., 2020. Magnetotelluric Characterization of The Alhama De Murcia Fault (Eastern Betics, Spain) and Study of Magnetotelluric Interstation Impedance Inversion. Earth, Planets and Space 72. DOI: 10.1186/S40623-020-1143-2

Marwan, M., Yanis, M., Nugraha, G.S., Zainal, M., Arahman, N., Idroes, R., Dharma, D.B., Saputra, D., Gunawan, P., 2021. Mapping of Fault and Hydrothermal System Beneath The Seulawah Volcano Inferred From A Magnetotellurics Structure. Energies 2021, Vol. 14, Page 6091 14, 6091. DOI: 10.3390/En14196091

Maryadi, M., Firdaus, A., Zarkasyi, A., Mizunaga, H., 2022. Electrical Resistivity Structure of Danau Ranau Geothermal Prospect Area Based On Integrated 3-D Inversion of Impedance Tensor and Tipper Vector. Geothermics 106, 102575. DOI: 10.1016/J.Geothermics.2022.102575

Matsushima, N., Utsugi, M., Takakura, S., Yamasaki, T., Hata, M., Hashimoto, T., Uyeshima, M., 2020. Magmatic–Hydrothermal System of Aso Volcano, Japan, Inferred From Electrical Resistivity Structures. Earth, Planets and Space 72. DOI: 10.1186/S40623-020-01180-8

Miller, C.A., Williams-Jones, G., Fournier, D., Witter, J., 2017. 3d Gravity Inversion and Thermodynamic Modelling Reveal Properties of Shallow Silicic Magma Reservoir Beneath Laguna Del Maule, Chile. Earth Planet Sci Lett 459, 14–27. DOI: 10.1016/J.Epsl.2016.11.007

Mitchell, M.A., Peacock, J.R., Burgess, S.D., 2023. Imaging The Magmatic Plumbing of The Clear Lake Volcanic Field Using 3-D Gravity Inversions. Journal of Volcanology and Geothermal Research 435, 107758. DOI: 10.1016/J.Jvolgeores.2023.107758

Mitjanas, G., Ledo, J., Macau, A., Alías, G., Queralt, P., Bellmunt, F., Rivero, L., Gabàs, A., Marcuello, A., Benjumea, B., Martí, A., Figueras, S., 2021. Integrated Seismic Ambient Noise, Magnetotellurics and Gravity Data For The 2d Interpretation of The Vallès Basin Structure in The Geothermal System of La Garriga-Samalús (Ne Spain). Geothermics 93. DOI: 10.1016/J.Geothermics.2021.102067

Mizunaga, H., Tanaka, T., Hashimoto, K., Onodera, S., 2022. Advancement of MT Exploration Techniques Utilizing Compact and Lightweight Equipment (1): Summary of the Project. Proceedings of the 146th SEGJ Conference. Tokyo

Moeck, I.S., 2014. Catalog of Geothermal Play Types Based On Geologic Controls. Renewable and Sustainable Energy Reviews 37, 867–882. DOI: 10.1016/J.Rser.2014.05.032

Mulugeta, B.D., Fujimitsu, Y., Nishijima, J., Saibi, H., 2021. Interpretation of Gravity Data To Delineate The Subsurface Structures and Reservoir Geometry of The Aluto–Langano Geothermal Field, Ethiopia. Geothermics 94. DOI: 10.1016/J.Geothermics.2021.102093

Muñoz, G., 2014. Exploring For Geothermal Resources With Electromagnetic Methods. Surv Geophys 35, 101–122. DOI: 10.1007/S10712-013-9236-0/Figures/11

Nagy, D., Papp, G., Benedek, J., 2002. Corrections To "The Gravitational Potential and Its Derivatives For The Prism." Journal of Geodesy 2002 76:8 76, 475–475. DOI: 10.1007/S00190-002-0264-7

Nagy, D., Papp, G., Benedek, J., 2000. The Gravitational Potential and Its Derivatives For The Prism. J Geod 74, 552–560. DOI: 10.1007/S001900000116

NASA (2013). NASA Shuttle Radar Topography Mission Global 1 arc second [Data set]. NASA EOSDIS Land Processes Distributed Active Archive Center. Accessed 2022-06-03 from https://doi.org/10.5067/MEaSUREs/SRTM/SRTMGL1.003

Natawidjaja, D.H., 2018. Updating Active Fault Maps and Sliprates Along The Sumatran Fault Zone, Indonesia. IOP Conf Ser Earth Environ Sci 118. DOI: 10.1088/1755-1315/118/1/012001

Neukirch, M., Garcia, X., 2014. Nonstationary Magnetotelluric Data Processing With Instantaneous Parameter. J Geophys Res Solid Earth 119, 1634–1654. DOI: 10.1002/2013jb010494

Newman, G.A., Gasperikova, E., Hoversten, G.M., Wannamaker, P.E., 2008. Three-Dimensional Magnetotelluric Characterization of The Coso Geothermal Field. Geothermics 37. DOI: 10.1016/J.Geothermics.2008.02.006

Newman, G.A., Lindsey, N.J., Gasperikova, E., Bertrand, E.A., Caldwell, T.G., 2015. The Importance of Full Impedance Tensor Analysis For 3d Magnetotelluric Imaging The Roots of High Temperature Geothermal Systems: Application to The Taupo Volcanic Zone, New Zealand. World Geothermal Congress 2015.

Nimalsiri, T.B., Suriyaarachchi, N.B., Hobbs, B., Manzella, A., Fonseka, M., Dharmagunawardena, H.A., Subasinghe, N.D., 2015. Structure of A Low-Enthalpy Geothermal System Inferred From Magnetotellurics — A Case Study From Sri Lanka. J Appl Geophy 117, 104–110. DOI: 10.1016/J.Jappgeo.2015.03.025

Nishijima, J., Naritomi, K., 2017. Interpretation of Gravity Data To Delineate Underground Structure in The Beppu Geothermal Field, Central Kyushu, Japan. J Hydrol Reg Stud 11, 84–95. DOI: 10.1016/J.Ejrh.2015.11.022

NOAA, 2022. ETOPO 2022 15 Arc-Second Global Relief Model. National Centers For Environmental Information [Www Document]. DOI: 10.25921/Fd45-Gt74

Pedersen, L.B., 1982. The Magnetotelluric Impedance Tensor—Its Random and Bias Errors. Geophys Prospect 30, 188–210. DOI: 10.1111/J.1365-2478.1982.Tb01298.X

Pellerin, L., Alumbaugh, D., Reinemann, D. J., Thompson, P. D., 2004. Power line induced current in the Earth determined by magnetotelluric techniques. Applied Engineering in Agriculture 20, 703-706. DOI: 10.13031/2013.17450

Piña-Varas, P., Ledo, J., Queralt, P., Marcuello, A., Bellmunt, F., Hidalgo, R., Messeiller, M., 2014. 3-D Magnetotelluric Exploration of Tenerife Geothermal System (Canary Islands, Spain). Surv Geophys 35, 1045–1064. DOI: 10.1007/S10712-014-9280-4/Figures/11

Purnomo, B.J., Pichler, T., 2014. Geothermal Systems on The Island of Java, Indonesia. Journal of Volcanology and Geothermal Research 285, 47–59. DOI: 10.1016/J.Jvolgeores.2014.08.004

Richards, K., Revil, A., Jardani, A., Henderson, F., Batzle, M., Haas, A., 2010. Pattern of Shallow Ground Water Flow at Mount Princeton Hot Springs, Colorado, Using Geoelectrical Methods. Journal of Volcanology and Geothermal Research 198, 217–232. DOI: 10.1016/J.Jvolgeores.2010.09.001

Ritter, O., Junge, A., Dawes, G., Ritter, O., Junge, A., Dawes, G., 1998. New Equipment and Processing for Magnetotelluric Remote Reference Observations. Geoji 132, 535–548. DOI: 10.1046/J.1365-246x.1998.00440.X

Robertson, K., Thiel, S., Meqbel, N., 2020. Quality Over Quantity: On Workflow and Model Space Exploration of 3D Inversion of MT Data. Earth, Planets and Space 72. DOI: 10.1186/S40623-019-1125-4

Roden, J., Abdelsalam, M.G., Atekwana, E., El-Qady, G., Tarabees, E.A., 2011. Structural Influence on The Evolution of The Pre-Eonile Drainage System of Southern Egypt: Insights From Magnetotelluric and Gravity Data. Journal of African Earth Sciences 61, 358–368. DOI: 10.1016/J.Jafrearsci.2011.08.007

Rodríguez, J., Esparza, F.J., Gómez-Treviño, E., 2010. 2-D Niblett-Bostick Magnetotelluric Inversion. Geologica Acta 8. DOI: 10.1344/105.000001513

Rodriguez, J.A., Gharibi, M., Kuhn, O., 2021. Magnetotellurics in Exploration for Geothermal Targets. Recorder, Canadian Society of Exploration Geophysicist 46, 1–16.

Roots, E., Craven, J.A., 2017. 3-D Modelling of Magnetotelluric Data from The Western Superior Province, Ontario. DOI: 10.4095/306191

Saibi, H., Amrouche, M., Batir, J., Gabr, A., Fowler, A.R., 2022. Magnetic and Gravity Modeling and Subsurface Structure of Two Geothermal Fields in The UAE Geothermal Energy 10. DOI: 10.1186/S40517-022-00240-4

Saibi, H., Khosravi, S., Cherkose, B.A., Smirnov, M., Kebede, Y., Fowler, A.R., 2021. Magnetotelluric Data Analysis Using 2D Inversion: A Case Study from Al-Mubazzarah Geothermal Area (Amga), Al-Ain, United Arab Emirates. Heliyon 7, E07440. DOI: 10.1016/J.Heliyon.2021.E07440

Sampurno, Samodra, H., 1997. Geological Map of the Ponorogo Quadrangle, Jawa. Geological Research and Development Center. Bandung

Sandwell, D.T., Smith, W.H.F., 1997. Marine Gravity Anomaly from Geosat and ERS 1 Satellite Altimetry. Journal of Geophysical Research B: Solid Earth 102. DOI: 10.1029/96jb03223

Sari, E.K., Ponka, M.A., Sahradani, D.N., Yoga, D.A., Supriyanto, 2021. Study of Altered Lithologies in Gunung Lawu, Central Java, Indonesia Using Petrographic Analysis, in: IOP Conference Series: Earth and Environmental Science. IOP Publishing Ltd. DOI: 10.1088/1755-1315/846/1/012023

Sarkar, P., Mondal, S., Pal, S.K., Roy, P.N.S., Sahoo, S.D., Widyadwatmaja, A., Gupta, S., Gupta, A., 2022. New Insights on The Tectonic Framework Using EIGEN6C4 Gravity Data, Seismicity, and Finite Element Stress Analysis: An Attempt to Map Earthquake Vulnerable Zones in Parts of North-East India and Surroundings. Physics and Chemistry of The Earth 127. DOI: 10.1016/J.Pce.2022.103195

Sharma, P.V., 1997. Environmental and Engineering Geophysics. Cambridge: Cambridge University Press. ISBN: 9781139171168

Simpson, F., Bahr, K., 2005. Practical Magnetotellurics. Practical Magnetotellurics 9780521817271, 1–254. DOI: 10.1017/Cbo9780511614095

Siripunvaraporn, W., Egbert, G., 2009. WSINV3DMT: Vertical Magnetic Field Transfer Function Inversion and Parallel Implementation. Physics of The Earth and Planetary Interiors 173. DOI: 10.1016/J.Pepi.2009.01.013

Siripunvaraporn, W., Egbert, G., Uyeshima, M., 2005. Interpretation of Two-Dimensional Magnetotelluric Profile Data with Three-Dimensional Inversion:

Synthetic Examples. Geophys. J. Int 160, 804–814. DOI: 10.1111/J.1365-246x.2005.02527.X

Slezak, K., Jozwiak, W., Nowozynski, K., Orynski, S., Brasse, H., 2019. 3-D Studies of MT Data in The Central Polish Basin: Influence of Inversion Parameters, Model Space and Transfer Function Selection. J Appl Geophy 161. DOI: 10.1016/J.Jappgeo.2018.11.008

Spector, A., Grant, F.S., 1970. Statistical model for interpreting aeromagnetic data. Geophysics 35, 293–302. DOI: 10.1190/1.1440092

Spichak, V., Manzella, A., 2009. Electromagnetic Sounding of Geothermal Zones. J. Appl. Geophys. 68, 459–478. DOI: 10.1016/J.Jappgeo.2008.05.007

Sugianto, A., Kholid, M., Suhanto, E., 2009. Survey Magnetotelluric Daerah Panas Bumi Danau Ranau Lampung - Sumatera Selatan [Magnetotelluric Survey in Danau Ranau Geothermal Area, Lampung - South Sumatera], in: Prosiding Hasil Kegiatan Lapangan Pusat Sumber Daya Geologi 2009. Geological Agency of Indonesia, Bandung, pp. 323–333.

Suharmanto, P., Fitria, A.N., Ghaliyah, S., 2015. Indonesian Geothermal Energy Potential as Source of Alternative Energy Power Plant. Kne Energy 1, 119–124. DOI: 10.18502/Ken.V1i1.325

Tanaka, T., Mizunaga, H., Hashimoto, K., Onodera, S., 2022. Advancement of MT Exploration Techniques Utilizing Compact and Lightweight Equipment (2): Hardware Design and Prototyping. Proceedings of the 146th SEGJ Conference. Tokyo

Thiel, S., 2008. Basics of The Magnetotelluric Method. Behaviour.

Tietze, K., Ritter, O., 2013. Three-Dimensional Magnetotelluric Inversion in Practice-The Electrical Conductivity Structure of The San Andreas Fault in Central California. Geophys J Int 195. DOI: 10.1093/Gji/Ggt234

Tikhonov, A., 1950. On Determining Electrical Characteristics of The Deep Layers of The Earth’s Crust. Doklady 73.

Trad, D.O., Travassos, J.M., 2000. Wavelet Filtering of Magnetotelluric Data. DOI: 10.1190/1.1444742 65, 482–491. DOI: 10.1190/1.1444742

Triahadini, A., Aizawa, K., Teguri, Y., Koyama, T., Tsukamoto, K., Muramatsu, D., Chiba, K., Uyeshima, M., 2019. Magnetotelluric Transect of Unzen Graben, Japan: Conductors Associated With Normal Faults. Earth, Planets and Space 71, 28. DOI: 10.1186/S40623-019-1004-Z

Unsworth, M., 2007. Magnetotellurics. Encyclopedia of Geomagnetism and Paleomagnetism 670–673. DOI: 10.1007/978-1-4020-4423-6_207

Ussher, G., Harvey, C., Johnstone, R., Anderson, E., Zealand, N., 2000. Understanding The Resistivities Observed in Geothermal Systems. Proceedings of World Geothermal Congress.

Utami, P., 2018. Overview of Geothermal Potential, Challenges, and Opportunities in Asia, in: The 8th Regional Workshop on Integrated Resource Management in Asian Cities: The Urban Nexus. United Nations Escap, Bangkok.

Uwiduhaye, J. D. A., Sakindi, G., Saibi, H., Cherkose, B.A., 2021. Subsurface Geoelectrical Structure From 3-D Inversion of Magnetotelluric Data of Gisenyi Geothermal Field, Western Part of Rwanda. J Appl Geophy 186. DOI: 10.1016/J.Jappgeo.2021.104277

Vaish, J., Pal, S.K., 2015. Geological Mapping of Jharia Coalfield, India Using Grace Egm2008 Gravity Data: A Vertical Derivative Approach. Geocarto Int 30. DOI: 10.1080/10106049.2014.905637

Vozoff, K., 1991. The Magnetotelluric Method. Investigations in Geophysics Series 641–712. DOI: 10.1190/1.9781560802686.Ch8

Wang, G., Cao, H., Xiao, D., Wang, W., Zhu, W., Wang, D., She, Y., Cui, A., Zhang, G., 2023a. Geothermal Field Model in The Southeast of Shijiazhuang Region (China) Deduced from Magnetotelluric Data. J Appl Geophy 219, 105235. DOI: 10.1016/J.Jappgeo.2023.105235

Wang, P., Chen, X., Zhang, Y., 2023b. Synthesizing Magnetotelluric Time Series Based On Forward Modeling. Front Earth Sci (Lausanne) 11. DOI: 10.3389/Feart.2023.1086749

Weckmann, U., Magunia, A., Ritter, O., 2005. Effective Noise Separation for Magnetotelluric Single Site Data Processing Using a Frequency Domain Selection

Scheme. Geophys J Int 161, 635–652. DOI: 10.1111/J.1365-246x.2005.02621.X/3/161-3-635-Fig021.Jpeg

Wijns, C., Perez, C., Kowalczyk, P., 2005. Theta Map: Edge Detection in Magnetic Data. Geophysics 70. DOI: 10.1190/1.1988184/Asset/Images/Large/L39_1_F7.Jpeg

Wilcox, J., 2012. Indonesia's Energy Transit: Struggle to Realize Renewable Potential. Renewable Energy World.

Wright, P.M., Ward, S.H., Ross, H.P., West, R.C., 1985. State-of-the-art Geophysical Exploration for Geothermal Resources. Geophysics 50, 2666–2699. DOI: 10.1190/1.1441889

Xu, L.H., Gan, J.X., Liu, J., 2013. The Analysis of Influence Factors of MT Tipper Response. Wutan Huatan Jisuan Jishu 35. DOI: 10.3969/J.Issn.1001-1749.2013.04.10

Yadav, K., Shah, M., Sircar, A., 2020. Application of Magnetotelluric (MT) Study for The Identification of Shallow and Deep Aquifers in Dholera Geothermal Region. Groundw. Sustain. Dev. 11. DOI: 10.1016/J.Gsd.2020.100472

Yamaguchi, S., Ogawa, Y., Fuji-Ta, K., Ujihara, N., Inokuchi, H., Oshiman, N., 2010. Audio-Frequency Magnetotelluric Imaging of The Hijima Fault, Yamasaki Fault System, Southwest Japan. Earth, Planets, and Space 62. DOI: 10.5047/Eps.2009.12.007

Zhang, L., Koyama, T., Utada, H., Yu, P., Wang, J., 2012. A Regularized Three-Dimensional Magnetotelluric Inversion with A Minimum Gradient Support Constraint. Geophys J Int 189. DOI: 10.1111/J.1365-246x.2012.05379.X

Zhang, L., Ren, Z., Xiao, X., Tang, J., Li, G., 2022. Identification and Suppression of Magnetotelluric Noise Via a Deep Residual Network. Minerals 12. DOI: 10.3390/Min12060766

Zhdanov, M. S., 2018. Magnetotelluric and Magnetovariational Methods, in: Foundations of Geophysical Electromagnetic Theory and Methods. DOI: 10.1016/B978-0-44-463890-8.00017-7

Zhdanov, M. S., Dmitriev, V. I., Gribenko, A. V., 2010. Joint Three-Dimensional Inversion of Magnetotelluric and Magnetovariational Data. Izvestiya, Physics of The Solid Earth 46, 655–669. DOI: 10.1134/S1069351310080033

Zhou, J., Hu, X., Xiao, T., 2020. A Regularized Magnetotelluric Inversion with A Minimum Support Gradient Constraint*. Earthquake Science 33. DOI: 10.29382/Eqs-2020-0130-03

Zhou, W., Hu, X., Guo, H., Liu, Shuang, Liu, Sijing, Yang, B., 2022. Three-Dimensional Magnetotelluric Inversion Reveals the Typical Geothermal Structure of Yanggao Geothermal Field in Datong Basin, Northern China. Geothermics 105, 102505. DOI: 10.1016/J.Geothermics.2022.102505

Zuo, G., Ren, Z., Xiao, X., Tang, J., Zhang, L., Li, G., 2022. Magnetotelluric Noise Attenuation Using A Deep Residual Shrinkage Network. Minerals 12. DOI: 10.3390/Min12091086